UNIVERSITÉ DE TOURS

ÉCOLE DOCTORALE : MIPTIS

Institut Denis Poisson UMR CNRS 7013, France

THÈSE présentée par :

Anatolii KORNEEV

soutenue le : **13 décembre 2023**

pour obtenir le grade de : **Docteur de l'université de Tours**
Discipline/ Spécialité : **Physique Théorique**

Compact Chandrasekhar-Kendall states in noncentrosymmetric superconductors

THÈSE dirigée par :

CHERNODUB Maxim	Directeur de Recherche, Université de Tours
MOLOCHKOV Alexander	Professeur, School of Physics, Beijing Institute of Technology, Beijing, P.R. China

RAPPORTEURS :

PASCALUTSA Vladimir	Professeur, Institut für Kernphysik, Johannes Gutenberg-Universität Mainz, Mainz, Germany
WIEGMANN Pavel	Professeur, Kadanoff Center for Theoretical Physics, University of Chicago, Chicago, USA

PRÈSIDENT DU JURY

NIEMI Antti	Professeur**,** Nordita, Stockholm University, Stockholm, Sweden

JURY : ***(directeurs, rapporteurs, examinateurs)***

CHERNODUB Maxim	Directeur de Recherche, Université de Tours
MOLOCHKOV Alexander	Professeur, School of Physics, Beijing Institute of Technology, Beijing, P.R. China
NICOLIS Stam	Maître de Conférences, Université de Tours
NIEMI Antti	Professeur, Nordita, Stockholm University, Stockholm, Sweden
PASCALUTSA Vladimir	Professeur, Institut für Kernphysik, Johannes Gutenberg-Universität Mainz, Mainz, Germany
WIEGMANN Pavel	Professeur, Kadanoff Center for Theoretical Physics, University of Chicago, Chicago, USA

Acknowledgements

First, I am extremely grateful to my supervisors, Prof. Alexander Molochkov and Prof. Maxim Chernodub for their continuous support, invaluable patience and inspiration during my PhD study. Words cannot express my gratitude to them, their advice and professional knowledge has always led me in the right direction in my research.

I would like to thank Prof. Vladimir Pascalutsa and Prof. Pavel Wiegmann for the acceptance of being the reviewers of my thesis.

I would like to extend my sincere thanks to Dr. Stam Nicolis and Prof. Antti Niemi for the acceptance of being members of the jury committee.

I would like to acknowledge all friends and colleagues from Far Eastern Federal University. Especially Alexander Begun, who has shared his time during our PhD study.

Thanks also to Julien Garaud for his invaluable assistance in 3D visualization of the resulting configurations and helpful discussions.

Finally, I would like to express special gratitude to my wife. Without her belief in me, her support and understanding, it would not have been possible to complete my study.

Abstract

In this thesis we demonstrate that superconductors with broken inversion symmetry support a family of stable, spatially localized configurations of the self-knotted magnetic field. These solutions are the superconducting counterparts of the Chandrasekhar-Kendall states (spheromaks or toroflux) that appear in highly conducting, force-free astrophysical and nuclear-fusion plasmas.

We study the superconducting spheromaks in the Ginzburg-Landau formalism, in the presence of a parity-breaking Lifshitz invariant associated with the O crystallographic point group symmetry. We demonstrate that in the London limit, the total energy of the solution diverges in the ultraviolet region and, therefore, needs to be regularized at the singular core region.

We show that an isolated spherical impurity may serve as a pinning center for a finite-energy superconducting Chandrasekhar-Kendall state and explicitly solve the equations of motion in the presence of an impurity. Also we argue that a magnetic dipole or a ferromagnetic inclusion in the bulk of a noncentrosymmetric superconductor source finite-energy spheromak solutions. We explicitly construct solutions induced by a ferromagnetic dipole and discuss the influence of the parity-breaking parameter on the structure, energy, and helicity of these configurations.

Résumé

Dans cette thèse, nous démontrons que les supraconducteurs à symétrie d'inversion brisée supportent une famille de configurations stables et spatialement localisées du champ magnétique auto-noué. Ces solutions sont les homologues supraconducteurs des états de Chandrasekhar-Kendall (les sphéromaks ou les toroflux) qui apparaissent dans les plasmas astrophysiques et de fusion nucléaire hautement conducteurs et sans force.

Nous étudions les sphéromaks supraconducteurs dans le formalisme de Ginzburg-Landau, en présence d'un invariant de Lifshitz brisant la parité associé à la symétrie cristallographique du premier groupe ponctuel. Nous démontrons que dans la limite de Londres, l'énergie totale de la solution diverge dans la région ultraviolette et, par conséquent, doit être régularisée dans la région du noyau singulier.

Nous montrons qu'une impureté sphérique isolée peut servir de centre de fixation pour un état supraconducteur de Chandrasekhar-Kendall à énergie finie et résoudre explicitement les équations du mouvement en présence d'une impureté. Nous soutenons également qu'un dipôle magnétique ou une inclusion ferromagnétique dans la masse d'un supraconducteur non centrosymétrique fournit des solutions de sphéromak à énergie finie. Nous construisons explicitement des solutions induites par un dipôle ferromagnétique et discutons de l'influence du paramètre de rupture de parité sur la structure, l'énergie et l'hélicité de ces configurations.

Contents

Introduction **17**

1 Literature review **21**

1.1 Basic macroscopic properties of superconductors 21

1.2 Type I and II superconductors 24

1.3 Noncentrosymmetric superconductors 25

1.4 The basics of the microscopic theory of superconductivity 27

1.4.1 Microscopic derivation of the Ginzburg - Landau model 27

1.5 Topological objects in field theories and condensed matter 29

1.5.1 Examples of knotted configurations in physical systems 30

2 Knotted self-linked configurations in noncentrosymmetric superconductors **33**

2.1 Ginzburg-Landau free energy 33

2.1.1 Critical value of the parity breaking 35

2.2 London limit 36

2.2.1 Field equations 36

2.2.2 Compact analytical vortex-free spheromak solutions 40

2.2.3 Explicit solution for parity-breaking $\Gamma = 1/\sqrt{2}$ 48

2.2.4 Helicity of spheromak solutions 52

2.3 Finite-energy solution 54

2.3.1 Solution in superconducting exterior 55

2.3.2 Configuration of the free magnetic field inside cavity 61

2.3.3 Consistent $l = 1$ solution in the whole space 64

2.3.4 Estimations of physical characteristics 73

3 Configurations induced by ferromagnetic inclusions **75**

3.1 Localized force-free solutions 75

3.1.1 London-limit 76

3.1.2 Derivation of a general solution via vector spherical harmonics . 78

3.2 Magnetized inclusion 81

3.2.1 Explicit forms of the toroflux induced by a magnetic dipole . . . 84
3.2.2 Outline of the Chandraseckhar-Kendall approach for a dipole source . . . 87
3.2.3 Knotted nature of toroflux . . . 88
3.2.4 Energy and helicity of the toroflux . . . 90
3.2.5 Toroidal dipole moments . . . 92
3.3 Experimental detection of the toroflux state . . . 93

Conclusion **97**

Appendices **101**
A Vector spherical harmonics . . . 101
A.1 Differential operators on vector spherical harmonics . . . 102
A.2 First vector spherical harmonics . . . 103
A.3 Integrals of vector spherical functions . . . 104
B Special functions . . . 104
B.1 Kelvin functions . . . 104
B.2 The spherical Hankel functions . . . 106
C Investigaton of structure and dynamics of proteins by the Landau – Ginzburg – Wilson approach . . . 107

Author's articles

[1] Julien Garaud, Anatolii Korneev, Albert Samoilenka, Alexander Molochkov, Egor Babaev, and Maxim Chernodub, *"Counterpart of the Chandrasekhar-Kendall state in noncentrosymmetric superconductors"*, Physical Review B 108, 014504 (2023)

[2] N. Gerasimeniuk, V. Bornyakov, V. Goy, R. Rogalyov, A. Korneev, A. Molochkov, and A. Nakamura, *"Lee–Yang Zeroes in the Baryon Fugacity Plane: The Role of High Densities"*, Particles 2023, 6, 834-846

[3] R.N. Rogalev, V.G. Bornyakov, N.V. Gerasimeniuk, V.A. Goy, A.A. Korneev, A.V. Molochkov, and A. Nakamura, *"Roberge–Weiss Transition in the Lee–Yang Approach"*, Physics of Particles and Nuclei Letters 20, 438–442 (2023)

[4] V.G. Bornyakov, N.V. Gerasimeniuk, V.A. Goy, A.A. Korneev, A.V. Molochkov, A. Nakamura, and R.N. Rogalyov, *"Numerical Study of the Roberge-Weiss Transition"*, Physical Review D 107, 014508 (2023)

[5] Anatolii Korneev, Alexander Begun, Sergei Liubimov, Khatuna Kachlishvili, Alexander Molochkov, Antti J. Niemi, and Gia G. Maisuradze, *"Exploring Structural Flexibility and Stability of α-Synuclein by the Landau-Ginzburg-Wilson Approach"*, Journal of Physical Chemistry B, 2022, 126(36), pp. 6878–6890

[6] Adam K. Sieradzan, Anatolii Korneev, Alexander Begun, Khatuna Kachlishvili, Harold A. Scheraga, Alexander Molochkov, Patrick Senet, Antti J. Niemi, and Gia G. Maisuradze, *"Investigation of Phosphorylation-Induced Folding of an Intrinsically Disordered Protein by Coarse-Grained Molecular Dynamics"*, Journal of Chemical Theory and Computation, 2021, 17(5), pp. 3203–3220

[7] Khatuna Kachlishvili, Anatolii Korneev, Luka Maisuradze, Jiaojiao Liu, Harold A. Scheraga, Alexander Molochkov, Patrick Senet, Antti J. Niemi, and Gia G. Maisuradze, *"New Insights into Folding, Misfolding, and Nonfolding Dynamics of a WW Domain"*, Journal of Physical Chemistry B, 2020, 124(19), pp. 3855–3872

List of Figures

1.1 Schematic representation of the Meissner effect. When the critical temperature T_c is reached, the external magnetic field is pushed out of the material. 23

1.2 Phase diagrams for type I and II superconductors. 25

2.1 Three-dimensional distributions of vector current lines in a bulk of noncentrosymmtric superconductor for two different points of view in the case of the parameter $\Gamma = 0.5$. 44

2.2 Multiple streamlines of the current density $\boldsymbol{j}_1$ for different starting points. Entanglement and intertwinning of these lines gives us the complete configuration shown in the Fig. 2.1. 45

2.3 The dependence of the energy (2.52) of the $l = 1$ spheromak on the parity-odd parameter Γ for $a_{\rm UV} \equiv \xi = 0.1\lambda_L$. The energy is shown in the units of $\mathcal{E}_0 = 4\pi^2 k^2 \lambda_L^5 \mathcal{A}^2$. 46

2.4 The dependence of the total energy of the $l = 1$ spheromak normalized to the energy of the magnetic field (2.56) for $a_{\rm UV} \equiv \xi = 0.1\lambda_L$. 48

2.5 Three-dimensional distributions of magnetic field lines in a bulk of noncentrosymmtric superconductor for two set of values l and m in the case of $\Gamma = 1/\sqrt{2}$. 50

2.6 Dependence of the derivative of the function $(f_l(r))$ on r for several values of the orbital number l. 52

2.7 The helicity (2.76) of the $l = 1$ spheromak as a function of the parity-breaking parameter Γ for different sizes of the (dimensionless) spheromak core $r_0 = \xi/\lambda_L$. 53

2.8 The helicity (2.76) normalized to the energy of magnetic field (2.77) as a function of the parity-breaking parameter Γ for different sizes of the (dimensionless) spheromak core $r_0 = \xi/\lambda_L$. 54

2.9 Location of the first few zeros of the $J^{\boldsymbol{Y}}(r)$ (2.83) for three different values of Γ. 57

2.10 Dependence of the first inter-shell radius R_0 of the superconducting spheromak solution on the parity-odd strentgh Γ. The dot marks the end-point of the curve at border of the stability zone, $\Gamma = 1$. 58

2.11 Dependence of the inter-shell radii R_0 of the first three cavities on the parity-odd strentgh Γ. 58

2.12 Dependence of the $\boldsymbol{\Psi}$-component of the surface current $\boldsymbol{J}_S$ on the parity-odd strength Γ. The magnitude is shown in the units of $J_{S_0} = \pi k \lambda_L \mathcal{A}$. 65

2.13 (a) Spheromak solution for the angular momentum numbers $(l, m) = (1, 0)$ and the parity breaking parameter $\Gamma = 0.1$. The top panel displays streamlines of the magnetic field H, and the bottom panel shows streamlines of the current J. The sphere in the center shows the vacuum cavity. (b) The same but for the parity breaking parameter $\Gamma = 0.5$. . . 66

2.14 The structure of the streamlines of the magnetic field H and the electric current J, for the lowest-energy spheromak with the projections $m = 0, 1$ of the total orbital momentum $l = 1$ for the two values of the parity-odd parameter: $\Gamma = 0.5$ and 0.95. The line on the top row shows streamlines of H, and the two next rows show the Poincaré sections of the streamlines of H on the $x = 0$ and $z = 0$ planes respectively. Similarly, the block of the three bottom rows indicate the structure of the current J. The central sphere depicts the vacuum cavity. 67

2.15 Dependence of the magnetic field energy in the cavity (2.121) on the parameter Γ. Energy is expressed in units of $\mathcal{E}_0 = 4\pi^2 k^2 \lambda_L^5 \mathcal{A}^2$. 68

2.16 Dependences of the total energy of the system (blue solid line), the energy of the magnetic field in the cavity (2.121) (orange dash-dotted line) and the energy of the superconducting state (2.52) (green dotted line) on parameter Γ. The red dot indicates the finiteness of the energy at $\Gamma = 1$. Energy is expressed in units of $\mathcal{E}_0 = 4\pi^2 k^2 \lambda_L^5 \mathcal{A}^2$. 69

2.17 The total helicity of the lowest-energy $l = 1$ superconducting spheromak solution (the blue solid line), the helicity of the magnetic field in the cavity (2.139) (the orange dashed line), and the helicity of the spheromak in the superconducting part outside the cavity (2.75) (the green dash-dotted line) on the parity-odd parameter Γ. The red dot indicates the value of the helicity of the magnetic field in the cavity at $\Gamma = 1$. The helicity is shown in the units of $\mathcal{H}_0 = 16\pi^2 k^2 \lambda_L^6 \mathcal{A}^2$. 72

2.18 The total helicity of the $l = 1$ spheromak, normalized to the total energy of magnetic field, as a function of the parity-breaking parameter Γ. The blue dot indicates the finite value of the normalized helicity at $\Gamma = 1$. . 73

3.1 Schematic representation of a spherical magnetized medium (#1) of radius r0 and the noncentrosymmetric superconducting medium (#2). The unit vector $\boldsymbol{n}_{12}$ is the normal vector at the interface between these media. 82
3.2 A toroflux solution induced by a magnetic dipole for the parity breaking parameter $\Gamma = 0.5$. The left panel displays the streamlines of the magnetic field $\boldsymbol{H}$, while the right panel shows the streamlines of the total electric current $\boldsymbol{J}$. These quantities are related to the other to the Ampère-Maxwell equation (3.8). The sphere in the center shows the position of the magnetized inclusion (the magnetic dipole). 88
3.3 Normalized free energy $\tilde{F}$ and normalized helicity $\tilde{H}$ of the toroflux as functions of the parity breaking coupling Γ for the spherical magnetic-dipole impurity of the radius $r_0 = 10^{-2}$ (in units of λ_L). 89
3.4 The structure of the streamlines of the magnetic field $\boldsymbol{H}$ of the toroflux solution induced by a magnetic dipole, for the values of the parity-breaking parameter $\Gamma = 0.15, 0.5,$ and 0.95. The line on the top row shows the streamlines of $\boldsymbol{H}$, and the two next rows are the Poincaré sections of the streamlines of $\boldsymbol{H}$ on the $x = 0$ and $z = 0$ planes, respectively. The central sphere depicts the spherical magnetic dipole inclusion. The relative sizes of the torofluxes can be seen from the vector basis. 90
3.5 The structure of the streamlines of the electric current $\boldsymbol{J}$, of the toroflux solution induced by a magnetic dipole, for the values of the parity-breaking parameter $\Gamma = 0.15, 0.5,$ and 0.95. The line on the top row shows the streamlines of $\boldsymbol{J}$, and the two next rows are the Poincaré sections of the streamlines of $\boldsymbol{J}$ on the $x = 0$ and $z = 0$ planes, respectively. The central sphere depicts the spherical magnetic dipole inclusion. The relative sizes of the torofluxes can be seen from the vector basis. 91
3.6 The amplitude of the toroidal dipole moments of the toroflux induced by a point-like magnetic dipole, as functions of the parity breaking coupling Γ. The toroidal dipole moment associated with the induction $\boldsymbol{T}^{\boldsymbol{B}}_{10}$ grows linearly with Γ, taking its maximum at the maximal value of the parity breaking parameter, $\Gamma = 1$. Quite surprisingly, $\boldsymbol{T}^{\boldsymbol{B}}_{10}$, the magnetic dipole moment $\boldsymbol{T}^{\boldsymbol{H}}_{10}$ is maximal at $\Gamma = 1/\sqrt{3}$, and vanishes at maximal parity breaking. 94

Introduction

Starting with the work of Lord Kelvin [1] on the representation of atoms as topological knotted vortex tubes in ether, the extensive studies of knotted structures begin both from the point of view of mathematics [2] and physics [3]. Around the same time, the phenomenon of superconductivity [4] was discovered in the Leiden laboratory. This phenomenon has become one of the few direct manifestations of quantum effects in the "classical" world. In this work, both of these facts are combined in one physical phenomenon - the purpose of the study is to argue that the certain class of superconducting materials, superconductors with broken symmetry of spatial inversion, support a family of stable, spatially localized configurations of the self-knotted magnetic field.

Superconductors react differently to an external magnetic field. In ordinary, parity-unbroken superconductors, the magnetic flux is almost totally, except for the surface layer, expelled by the superconducting condensate due to Meissner effect [5] (type I superconductivity). Ordinary type II superconductors also expel weak magnetic fields due to the Meissner effect, while if the magnetic-field background is strong enough, the magnetic flux penetrates thus superconducting medium in the form of a regular lattice or a liquid of Abrikosov vortices [6, 7]. Moreover, quantum or thermal fluctuations can induce closed loops of such quantum vortices. Due to the vortex string tension, these loops are unstable and eventually decay. Thus, apart from certain cases demonstrated in multicomponent systems that allow for different topology [8] bulk superconductors do not feature stable, localized configurations of the magnetic field (in three dimensions). Moreover, in a superconductor with a single order parameter, the magnetic flux carried by an Abrikosov vortex is necessarily quantized in units of the elementary magnetic flux.

In spite of these features, we demonstrate the existence of a new class of a compact self-supporting three-dimensional configurations of a knotted magnetic field which carry, in general, a non-quantized flux. These unusual solutions are supported in the bulk of parity-odd superconductors due to the breaking of the parity reversal symmetry. The latter feature plays a crucial role in the effect: we show in the thesis that no such configurations could exist in the ordinary superconductor with unbroken parity.

Noncentrosymmetric superconductors, that is superconductors whose crystal lattices lack inversion symmetry, have attracted significant attention from both theoreti-

cal [9–15] and experimental [16–20] communities. A key property of a noncentrosymmetric crystal is that it cannot be superimposed on its spatially inverted image with the help of spatial translations. The crystal thus explicitly breaks the parity inversion group. Since the superconducting order parameter captures the parity-breaking properties of the underlying ionic lattice, the noncentrosymmetric superconductors constitute a class of exotic systems that spontaneously break a continuous symmetry, in a parity violating medium (see Refs. [21–23] for detailed reviews). Parity-breaking superconducting systems feature several distinctive properties: they generate unusual magnetoelectric transport phenomena, exhibit a correlation between supercurrents and electron spin polarizations, lead to the emergence of helical states, and host, in the background of the magnetic field, the vortex lattices with exotic spatial structure [21–24].

At the macroscopic level, the noncentrosymmetric superconductors may be treated in the scope of the Ginzburg-Landau formalism with a single superconducting order parameter. The parity-odd properties of the noncentrosymmetric material are encoded via additional terms in the Ginzburg-Landau free energy, which are proportional to the so-called Lifshitz invariants allowed by broken inversion symmetry. These terms are linear in the magnetic field and in the gradients of the superconducting order parameter: $\propto k_{ij}B_i\mathrm{Im}(\psi^* D_j\psi)$. Here $\boldsymbol{D}$ is the gauge derivative of the order parameter ψ, and k_{ij} are coefficients, which concrete form depends on the point symmetry group of the underlying crystal structure.

We consider a particular class of isotropic noncentrosymmetric superconductors with chiral octahedral O point group symmetry, such as, for example, Li_2Pt_3B [18, 25], Mo_3Al_2C [26, 27] and PtSbS [28]. We demonstrate the existence of stable, spatially localized configurations of the self-knotted magnetic field as a solution of the Ginzburg-Landau formalism in the London limit. Thus, our solutions are eigenstates of the London equations for a noncentrosymmetric superconducting material. Labelled by their orbital ($0 < l < \infty$) and magnetic $-l \leqslant m \leqslant l$ quantum numbers, there are infinitely many l, m modes, for a given value of the parity breaking parameter. All of these modes have an intrinsic divergence at the origin, and therefore they require regularization at the core of the solutions. We show the existence of finite-energy solutions localized (pinned) at an isolated nonconducting vacuum spherical cavity. It should be noted that in the limit of weak parity-breaking, the minimal radius of the pinning cavity equals the golden ratio in units of the penetration length. Also we demonstrate that each divergent mode can be regularized by (pointlike) magnetic multipole sources. The case of a pointlike magnetic dipole is of particular physical relevance, as it corresponds to magnetic impurities inside a noncentrosymmetric superconductor. We argue that such magnetic impurities systematically induce a $(l, m) = (1, 0)$ finite energy solution mode.

As we shall see, the stability of our solution is supported by the fact that the lines of the magnetic lines self-intertwine with themselves and form a knotted-field configuration. Similar knotted configurations appear in many areas of physics, including particle physics [29], fluid dynamics [30], plasma physics [31], condensed matter [8, 32–34], and classical field theory [35, 36]. Knotted electromagnetic field configurations were also suggested to play a role in chirally imbalanced quark-gluon plasmas [37–41].

Our particular configuration of the knotted magnetic field can be considered as counterparts of the Chandrasekhar-Kendall (CK) states [42], in the context of non-centrosymmetric superconductors. The Chandrasekhar-Kendall states are divergence-free eigenvectors of the curl operator that determine the minimum-energy equilibrium configurations in magnetohydrodynamics of highly conducting, "force-free" plasmas. These states appear in various physical contexts, ranging from astrophysical plasmas [42] to nuclear fusion theory. In the latter case, the Chandrasekhar-Kendall eigenvectors are also known as Taylor states [43], which represent the relaxed minimum energy states of a plasma in a spheromak device (i.e., inside a spherical shell that confines the plasma which is counterpart of a tokamak device) and therefore are also called "spheromaks" [44, 45]. The principal difference between state in parity-broken superconductors and the Chandrasekhar-Kendall state in a conducting plasma, is that the state, which we found, are strongly localized configurations. The spatial localization of both the magnetic field and the supercurrent of investigated state originates from the Meissner effect.

We decided to name the investigated objects "toroflux", since, as we will see in the thesis below, the spatial configuration of magnetic field lines is extremely reminiscent of the lines of a well-known children's toy - toroflux. Also, sometimes we will call them as "spheromak", due to their connection with Chandrasekhar-Kendall state.

The thesis is organized as follows. The work consists of an introduction, three chapters, a conclusion, appendices, and a bibliography.

In the chapter 1, the main properties of the superconducting state are presented, the forms of existence of a magnetic field in a superconductor are given, the main features of materials with a crystal lattice that do not have an inversion center are given, and an overview of the knotted structures in various modern field theory models is given.

In the chapter 2, we introduce the Ginzburg-Landau (GL) model for parity breaking superconductor and derive the corresponding classical equations in the London limit. We discuss compact solutions for the magnetic field and electric currents in the parity-odd model using the basis of vector spherical harmonics. We discuss the explicit configurations, their energy and helicity densities, for lowest superconducting spheromak states and also provide the explicit form for an infinite series of states at a particular value of a parity-breaking parameter. We show that in the London limit,

the total energy of the solution diverges in the ultraviolet region and, therefore, needs to be regularized at the singular core region. We show that a large impurity may serve as a pinning center for a finite-energy superconducting CK state. We explicitly solve the classical equations of motion in the presence of an isolated spherical impurity and analyze properties of the corresponding solution.

In chapter 3, we express the London equation in terms of a force-free field, which allows us to obtain explicit solutions for all values of quantum numbers (l, m). There, we also determine the energy and helicity densities for the infinite tower of these states. We further demonstrate that in the London limit, the total energy of the solution is also diverges in its core. Next we show that a ferromagnetic inclusion regularizes the singular behavior of the solution, serving, at the same time, as a source for a finite-energy superconducting toroflux. Finally, we investigate the case where the inclusion is a ferromagnetic dipole. There, we explicitly construct solutions sourced by such an impurity. We discuss their properties and, in particular, the influence of the parity breaking parameter on the structure, energy, and helicity of knotted configurations.

Our conclusions are presented in the last section.

The appendices summarize useful relations for vector spherical harmonics, Kelvin functions, and associated Legendre polynomials used in this thesis.

The last appendix C is devoted to another topic of the author's scientific research, carried out in parallel during the years of work on the thesis, the study of the structure and dynamics of proteins using field theory methods. It provides basic information about the underlying theory, methods, and results obtained.

The list of references includes 124 sources.

Chapter 1

Literature review

1.1 Basic macroscopic properties of superconductors

Superconductors are materials that have no electrical resistance at some very low temperatures. For the first time, a superconducting state in a metal was discovered in the experiments of Heike Kamerlingh Onnes, who studied the properties of different materials at extremely low temperatures. In 1911, while working with mercury, he discovered that at a temperature slightly higher than 4.2 K, the electrical resistance of mercury completely disappears [4]. Moreover, the resistance abruptly became equal to zero and did not fall to zero smoothly and gradually. Further experiments showed that many other metals, as well as their intermetallic compounds and alloys, have the property of superconductivity.

Critical parameters

The temperature at which a material goes from a normal state to a superconducting state is called the critical temperature and is denoted T_c. For different pure substances and their compounds, the critical temperature takes on different values.

In addition to having a critical temperature, it has been found that superconductivity in materials can be destroyed when a sample is placed in an external magnetic field. This magnetic field is called the critical field and is denoted B_{cm}. The "m" prefix indicates that this value refers to a solid specimen, not a thin film or thread. The magnitude of the critical magnetic field B_{cm} is also determined by the type of matter.

There is an empirical dependence of the critical magnetic field on temperature:

$$B_{cm}(T) = B_{cm}(0)\left(1 - (T/T_c)^2\right), \tag{1.1}$$

where the value of $B_{cm}(0)$ is determined by the approximation of experimental data, since, according to the third law of thermodynamics (Nernst heat theorem), zero ab-

solute temperature is unattainable. This dependence is qualitatively demonstrated in the left half of Figure 1.2.

In addition to the critical temperature and magnetic field, there is a maximum current that can flow nondissipatively in a bulk in a superconducting state. This current is called critical current. Currents exceeding the critical value also destroy superconductivity and transfer matter to a normal state.

Meissner effect (Meissner–Ochsenfeld)

At the first time after the discovery of superconductivity, it was believed that the metal in the new state is an ideal diamagnet (substances magnetized against the direction of the external magnetic field). If this were the case, then during the transition of a conductor to a superconducting state in an external magnetic field the magnetic field would remain frozen into the material. But, as shown by experiments carried out in 1933 by Voltaire Meissner and Robert Ochsenfeld, a metal pushes out of itself a magnetic field when it goes into the superconducting state [5]. Moreover, this happens in any case, regardless of whether the sample was introduced into an external magnetic field before the transition to the superconducting state or afterward. Thus, the superconducting state is characterized by the complete absence of a magnetic field inside, which allows us to say that the transition from one state to another is a phase transition.

Magnetic flux quantization

Since the current can flow in superconductors without resistance, then if you take a ring from a superconductor and run a current through it, then it will never fade. In this case, the magnetic flux passing through the cavity of the ring can take on values that are multiples of a certain value

$$\Phi_0 = \pi\hbar/e = 2.07 \cdot 10^{-15}\ \mathrm{T} \cdot \mathrm{m}^2, \tag{1.2}$$

and called magnetic flux quantum. As we see, this quantum is expressed only in terms of fundamental mathematical and physical constants: the number π, the speed of light c and reduced Planck's constant $\hbar$. Experiments to determine the value of the magnetic flux quantum were determined in 1961 [46, 47]. Based on the existence of a magnetic flux quantum, it eventually became clear that superconductivity is a quantum phenomenon.

Josephson Effects

In 1962, two fundamentally new effects of superconductivity were predicted [48], which were named the Josephson effects, after their discoverer. These effects relate to the so-called phenomena of "weak superconductivity".

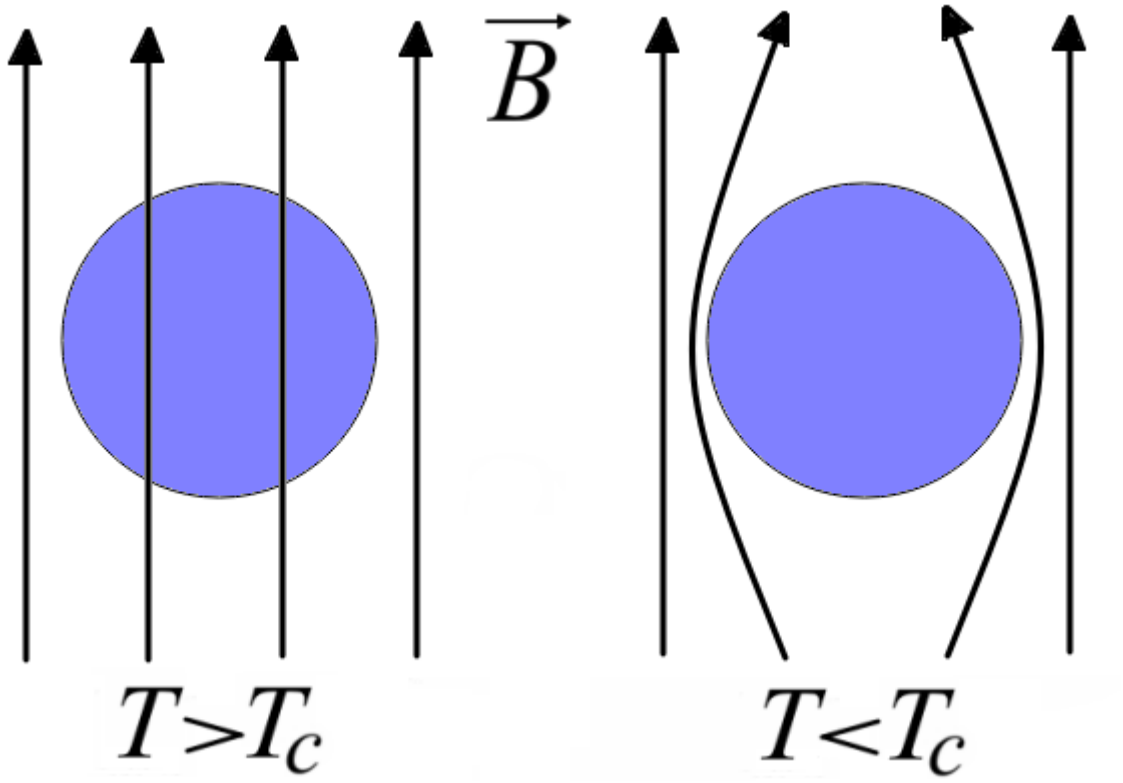

Figure 1.1: Schematic representation of the Meissner effect. When the critical temperature T_c is reached, the external magnetic field is pushed out of the material.

The first effect is usually called the "stationary" Josephson effect. It lies in the fact that the supercurrent continues through a weak bond (the connection of two superconductors by a thin layer of insulator, a thin film, or, for example, a very small area of their contact). Through the tunneling effect, the wave functions of electrons on both sides interfere with each other and a coherent behavior of electrons arises. Thus, all electrons on both sides of the weak bond are described by one wave function. This phenomenon was investigated experimentally at Bell Telephone Laboratories [49].

The second effect is the "non-stationary" Josephson effect. On the weak bond discussed above, when a current is more than a certain critical value, a voltage appears. Moreover, this voltage will have a alternatingcomponent. Voltage oscillates at a frequency dependent on Planck's constant which also makes it possible to carry out more accurate experiments to determine its numerical value. The experiment to detect the radiation generated by this Josephson transition was for the first time in the world carried out by soviet physicists I.K. Yanson, V.M. Svistunov and I.M. Dmitrienko in 1965 [50].

1.2 Type I and II superconductors

There are various criteria for dividing superconductors into different types. One of them is the separation according to the value of the critical temperature T_c. For historical reasons, the interface between low-temperature superconductors and high-temperature superconductors (HTS) is a temperature of 30 K. This critical temperature was obtained in the experiment of K. Müller and J. Bednorz in 1986 for the LaBaCuO compound [51]. Until that moment, the maximum temperature did not even exceed 20 K. For example, in 1973, after annealing Nb_3Sn triniobium stanide, a temperature of 17 K [52] was obtained. Thus, the experiment of Bednorz and Müller gave impetus to the rapid development of the physics of high-temperature superconductors. To describe HTS on the basis of first principles, a completely new theoretical model was required, which has not yet been fully completed. Some types of modern models are given in the review by Yu.V. Kopaev [53]. For low-temperature superconductors, there is a theory first presented in 1957 by J. Bardeen, L. Cooper and J. Schrieffer (BCS theory), which is a microscopic theory and is based on first principles [54]. According to her, the mechanism for the appearance of superconductivity is the union, through the phonon interaction of two electrons into a bound state - a Cooper pair. This pair has a whole spin, as a result of which it is a boson and obeys Bose-Einstein statistics. A characteristic feature of the behavior of bosons is that, having the lowest possible energy (at temperatures near absolute zero), they pass into a state called the Bose-Einstein condensate [55]. The flow of matter in this state through the crystal lattice is nondissipative. HTS, as indicated above, are not described within the framework of this theory. Thus, this feature allows one more division of superconductors into two types: which are described by the BCS theories (the so-called ordinary superconductors) and not described.

The most basic criterion for distinguishing superconductors is their response to an external magnetic field. Despite the fact that the Meissner effect is fulfilled for all superconductors, there are some peculiarities associated with the penetration of the magnetic field into the superconducting state. By the type of response to an external field, there is a division into type I and type II superconductors.

When a type I superconductor is in an external magnetic field, the superconductivity is destroyed at the moment when the magnetic field exceeds the critical value determined by the type of material.

For a type II superconductor, we have two critical magnetic fields. When the first critical magnetic field is exceeded, the material is in the so-called mixed state. This state is characterized by the penetration of an external magnetic field into the superconductor in a special way: in the form of lines called Abrikosov vortex lines [56].

It should be noted that, for type I superconductors, the magnetic is still not com-

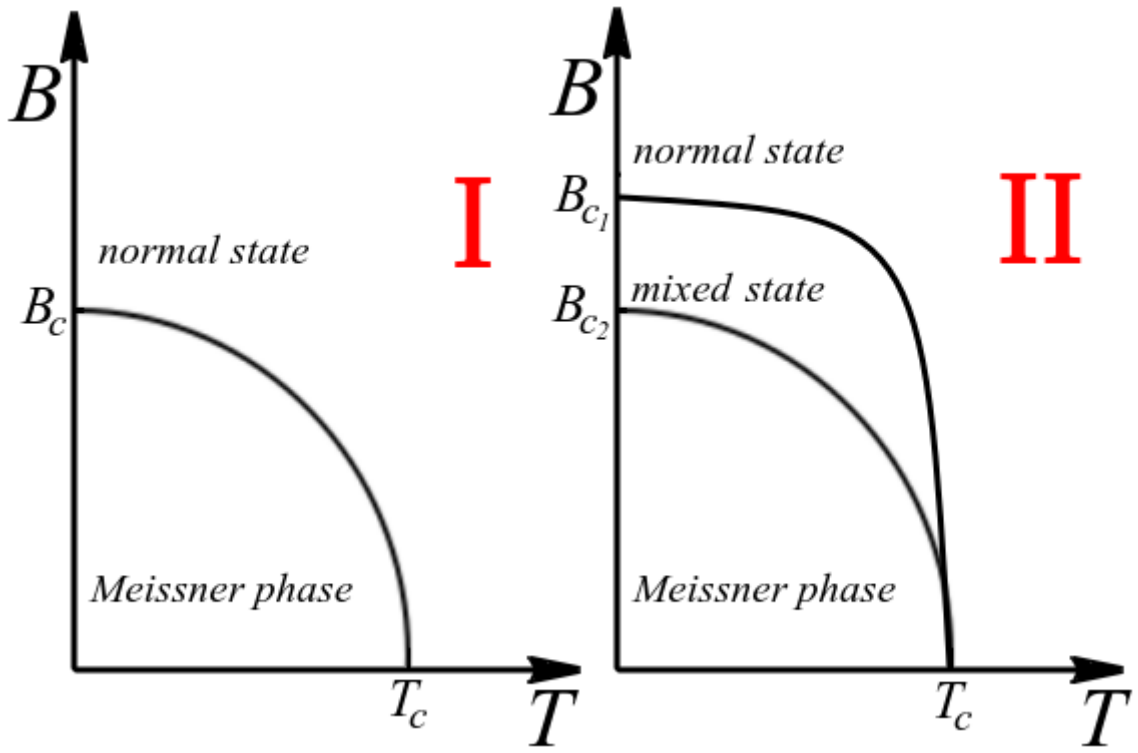

Figure 1.2: Phase diagrams for type I and II superconductors.

pletely squeezed out of the material but penetrates to a very shallow depth (called the London penetration depth) in the surface layer of the material.

Thus, in the superconducting state, ordinary superconductors either do not have a field inside, or it exists in the form of quantum lines (vortices).

1.3 Noncentrosymmetric superconductors

Noncentrosymmetric superconductors, that is superconductors whose crystal lattices lack inversion symmetry, have attracted significant attention from both theoretical[9–15] and experimental [16–20] communities. A key property of a noncentrosymmetric crystal is that after the operation of spatial inversion such crystals cannot be superimposed on themselves. The crystal thus explicitly breaks the parity inversion group. Since the superconducting order parameter captures the parity-breaking properties of the underlying ionic lattice, the noncentrosymmetric superconductors constitute a class of exotic systems that spontaneously break a continuous symmetry in a parity violating medium (see Refs. [21–23] for detailed reviews). Such systems exhibit a number of exotic features.

For example, noncentrosymmetric superconductors generate unusual magnetoelectric transport phenomena, exhibit a correlation between supercurrents and electron spin polarizations, are characterized by mixing of singlet and triplet components of superconducting condensates, lead to the appearance of helical states, and host, in

the background of the magnetic field, the vortex lattices with exotic spatial structure (see, for example, exhaustive reviews [21–23]). Recently, it was shown that vortices in parity-broken materials can exhibit an inversion of magnetic field at a certain distance from the vortex core, which leads to non-monotonic intervortex forces and, as a consequence, to the formation of bound vortex states and vortex clusters [57]. Vortexes can also form bound states at the sample boundary [58]. The parity breaking in noncentrosymmetric superconductors can also modify the Josephson effect with an unconventional phase-shifted relation for the Josephson current [59, 60]. Linked by a uniaxial ferromagnet, the unconventional Josephson junction was suggested to serve as an element of a qubit with a simple and presumably robust architecture [61].

At the macroscopic level, noncentrosymmetric superconductors can be considered in terms of the Ginzburg-Landau free energy with one superconducting order parameter. The properties of parity-odd material are encoded by the presence of additional terms that are proportional to the so-called Lifshitz invariants [62]. These terms are linear in the magnetic field and in the gradients of the superconducting order parameter: $\propto k_{ij} B_i \mathrm{Im}(\psi^* D_j \psi)$, where $\boldsymbol{D}$ is the gauge derivative of the order parameter ψ, and k_{ij} are coefficients depending on the crystal symmetry. Or, in other words, directly relate the magnetic field $\boldsymbol{B}$ to the current expressed in terms of the superconducting current $\boldsymbol{j}$. This current has the meaning of an ordinary supercurrent in the absence of the Lifshitz term. The specific form of a suitable Lifshitz invariant depends on the point symmetry group of the underlying crystal structure (Table 1.1).

Point group	Lifshitz invariant
O, T	$\gamma(B_x j_x + B_y j_y + B_z j_z)$
D_6, D_4 , D_3	$\gamma_1(B_x j_x + B_y j_y + B_z j_z) + \gamma_2 B_z j_z$
$C_{6\nu}$, $C_{4\nu}$, $C_{3\nu}$, D_{2d}	$\gamma(B_x j_y - B_y j_x)$
C_6, C_4, C_3	$\gamma_1(B_x j_x + B_y j_y + B_z j_z) + \gamma_2 B_z j_z + \gamma_3(B_x j_y - B_y j_x)$
S_4	$\gamma_1(B_x j_x - B_y j_y) + \gamma_2(B_y j_x + B_x j_y)$
D_2	$\gamma_1 B_x j_x + \gamma_2 B_y j_y + \gamma_3 B_z j_z$
$C_{2\nu}$	$\gamma_1 B_x j_y + \gamma_2 B_y j_x$
C_2	$\gamma_1 B_x j_x + \gamma_2 B_y j_y + \gamma_3 B_z j_z + \gamma_4 B_y j_x + \gamma_5 B_x j_y$

Table 1.1: Forms of Lifshitz invariants for various point symmetry groups. Data taken from [21].

Along with conventional superconductors, superconductors with disrupted spatial inversion are also gradually finding application in modern technology. For example, the world's first superconducting diode [63] was created on the basis of noncentrosymmetric superconductors. This development is characterized by minimal energy consumption, which will allow it to be used in more advanced electronic devices.

1.4 The basics of the microscopic theory of superconductivity

All macroscopic phenomena of conventional superconductors were described using the microscopic theory in 1957 by J. Bardeen, L.N. Cooper and J.R. Schrieffer [54]. The starting point for this theory was the isotope effect already known at that time: $T_c \sim M^{-1/2}$, where T_c is critical temperature and M is the isotopic mass. Quantitative expression for this effect was first obtained for mercury isotopes [64]. The existence of this dependence clearly indicates the contribution of the crystal lattice to the appearance of the superconducting state.

The derivation of macroparameters in terms of microparameters is given in the work of L.P.Gor'kov [65]. We will not repeat here Gorkov's primary derivation for superconductivity, but here we briefly consider the derivation of an expression for the GL free energy of a noncentrosymmetric superconductor, which was done in the paper by A. Samoilenka and E. Babaev [58].

1.4.1 Microscopic derivation of the Ginzburg - Landau model

In the paper [58] the derivation of the GL free energy is constructed as follows.

We begin by considering the continuous-space fermionic model with the action

$$S = \int_0^{\frac{1}{T}} d\tau \int_{-\infty}^{+\infty} d^3\boldsymbol{r} \sum_{\alpha,\beta=\downarrow,\uparrow} a^\dagger_\alpha (\vec{h}\cdot\vec{\sigma}_{\alpha\beta}) a_\beta - V a^\dagger_\uparrow a^\dagger_\downarrow a_\downarrow a_\uparrow \,, \tag{1.3}$$

in path integral formulation, given by partition function Z:

$$Z = \int D[a^\dagger, a] e^{-S} \,. \tag{1.4}$$

In the action (1.3) we switch to imaginary time $t = i\tau$ and the metric becomes Euclidean. This procedure (change from real to imaginary time) is often referred to as the Wick rotation. The T in the upper limit is the temperature and $a_\alpha(\tau, \boldsymbol{r})$, $a^\dagger_\alpha(\tau, \boldsymbol{r})$ are Grassman fields, that correspond to fermionic creation and annihilation operators, which depend on imaginary time τ, three dimensional space coordinates $\boldsymbol{r}$ and spin index α.

The first term in the action (1.3), which responsible for interacting with a magnetic field, includes

$$\begin{aligned} \vec{h} &= (\partial_\tau + E - \mu, \boldsymbol{h}), \quad \boldsymbol{h} = \boldsymbol{\gamma} - \mu_B \boldsymbol{B}, \\ \vec{\sigma} &= (\delta_{\alpha\beta}, \boldsymbol{\sigma}_{\alpha\beta}) \,, \end{aligned} \tag{1.5}$$

where $E(-i\boldsymbol{\nabla} - e\boldsymbol{A})$ is the single electron energy, μ is chemical potential, $\boldsymbol{\sigma}$ are the Pauli vector, e is electron charge, and μ_B is Bohr magneton. The term responsible for

the non-centrosymmetric nature of the system is spin-orbit coupling $\boldsymbol{\gamma}(-i\boldsymbol{\nabla} - e\boldsymbol{A})$. In the case of cubic O or T symmetry, $\boldsymbol{\gamma}(\boldsymbol{a}) = \gamma_0 a$.

The second term describe the simplest case with the BCS type of local attractive interaction with $V > 0$.

The authors focus on the standard situation where the macroscopic length scale λ, over which the vector potential $\boldsymbol{A}$ and the magnetic field $\boldsymbol{B}$ change, is much larger than the Fermi length scale $1/k_F$. As a result, they assume that the following inequalities hold:

$$\begin{aligned} \mu &\gg \omega_D \gg T_c\,, \\ \gamma_0 k_F &\gg \omega_D \gg \mu_B B\,, \end{aligned}$$

where k_F is the Fermi wavevector, ω_D is Debye frequency and T_c is the critical temperature of a superconductor.

Further, in the paper [58] were performed the Hubbard-Stratanovich transformation [66], [67]

$$e^{-ax^2/2} = \sqrt{\frac{1}{2\pi a}} \int_{-\infty}^{\infty} dy\, e^{-y^2/2a - ixy}\,, \tag{1.6}$$

so as to convert interaction term into field theory in terms of auxiliary scalar bosonic field $\Delta(\tau, \boldsymbol{r})$:

$$e^{V\int d\tau d\boldsymbol{r} a_\uparrow^\dagger a_\downarrow^\dagger a_\downarrow a_\uparrow} = \int D[\Delta^\dagger, \Delta] e^{-\int d\tau d\boldsymbol{r}\left(\frac{\Delta^\dagger \Delta}{V} + \Delta a_\downarrow a_\uparrow + \Delta a_\downarrow^\dagger a_\uparrow^\dagger\right)}\,. \tag{1.7}$$

Then, after a lot of calculations, including the Berezin integration, the result, up to the fourth order term, is the following expression for the minimal GL free energy of noncentrosymmetric superconductor:

$$F = \int d\boldsymbol{r} \left[\frac{(\boldsymbol{B} - \boldsymbol{H})^2}{2} + \alpha|\Delta|^2 + \beta|\Delta|^4 + \sum_{a=\pm 1} K_a \left| (v_{aF}\boldsymbol{D}^* - 2a\mu_B \boldsymbol{B})\,\Delta \right|^2 \right], \tag{1.8}$$

where all parameters depend on the microparameters of the theory [58].

Importantly, the energy of the model, derived in [58], in contrast to the phenomenological model presented in Chapter 5 of [21], is bounded from below.

The microscopically-derived model, can be rescaled and written in a more compact form:

$$F = \int d\boldsymbol{r} \left[\frac{(\boldsymbol{B} - \boldsymbol{H})^2}{2} + \sum_{a=\pm 1} \frac{|\boldsymbol{D}_a \psi|^2}{2\kappa_c} - |\psi|^2 + \frac{|\psi|^4}{2}\,, \right], \tag{1.9}$$

where $\boldsymbol{D}_a = i\boldsymbol{\nabla} - \boldsymbol{A} - (\gamma + a\nu)\boldsymbol{B}$.

The expression for new noncentrosymmetric term contains the parameter γ, which is appeared due to the microscopic spin-orbit coupling, and the parameter ν, which is responsible for the coupling to the Zeeman magnetic field.

Equations of motion are the following Ginzburg-Landau equations:

$$\sum_a \frac{\boldsymbol{D}_a^2\psi}{2\kappa_c} - \psi + |\psi|^2\psi = 0\,, \tag{1.10}$$

$$\boldsymbol{\nabla}\times\left(\boldsymbol{B} - \boldsymbol{H} - \sum_a(\gamma + a\nu)\boldsymbol{J}_a\right) = \sum_a \boldsymbol{J}_a\,, \tag{1.11}$$

and the corresponding boundary conditions reads as follows:

$$\boldsymbol{n}\cdot\sum_a \boldsymbol{D}_a\psi = 0\,, \quad \boldsymbol{n}\cdot\sum_a(\boldsymbol{D}_a\psi)^* = 0\,,$$
$$\boldsymbol{n}\times\left(\boldsymbol{B} - \boldsymbol{H} - \sum_a(\gamma + a\nu)\boldsymbol{J}_a\right) = 0\,, \tag{1.12}$$

where $\boldsymbol{J}_a = \frac{\mathrm{Re}(\psi^*\boldsymbol{D}_a\psi)}{\kappa_c}$.

1.5 Topological objects in field theories and condensed matter

In nonlinear field-theoretical models, there are solutions to classical equations that, without quantization, are similar to particles. These solutions are stable and have a finite size, finite energy, and in quantum models they are extended particles composed of elementary particles. Such particles (solutions) are called topological solitons (or topological defects) [68]. It should be noted that the existence of solitons is not possible in all nonlinear field theories. The possibility of the existence of topological solitons in various field theories obeys Derrek's theorem [69].

Depending on the form of the nonlinear equation of motion, topological solitons can be of various types. Let us briefly consider some of them and show in which areas of physics they can manifest themselves.

- Kink. Kinks arise in the theory with a complex field of $d = 1 + 1$. One of the physical manifestation of this object is description of the protein structure in terms of kinks [70];

- Vortex. Vortices appear in models with a gauge group $U(1)$ with scalar fields and the Higgs mechanism in $d = 2+1$. Vortices occur in the theory of condensed matter. They are observed in the Ginzburg-Landau model, which describes superconductors of the second kind [56] and in the Abelian Higgs model (relativistic analogue of GL model) [71]. They manifest themselves in the bosonic sector of the Electroweak model [72] and play an important role in topological phase transitions [73, 74].

- Skyrmion. This is soliton in nonlinear sigma-model in $(N+1)$ dimensional space-time with $[SU(2)_L \times SU(2)_R]/SU(N)_V$ global symmetry. In $(3+1)$ skyrmions are considered as a fairly realistic solitonic model of the nuclei (with well-reproduced physical quantities - mass, spin, isospin), where the topological charge is identified with baryon number.

Topological solitons in the form of knots are of another great interest. One of the brightest representatives of this type of configurations is the Hopfion solution, which has a topological invariant. In the next section, we will look at hopfions in a little more detail and consider some different knotted solutions in physics in general.

1.5.1 Examples of knotted configurations in physical systems

A hopfion (or Hopf soliton) is a topological soliton which is classified by the Hopf invariant (which is a linking number between field lines) [75]. A hopfion is a knot in a three-dimensional continuous unit vector field and cannot be unknotted without cutting. In a convenient form, the Hopf index is expressed in terms of an integral, as was introduced by Whitehead [76], which coincides with the definition of the helicity, which we use in the following chapters.

Hopfion-like objects appear in various physical theories, such as the usual Maxwell theory of electromagnetic fields [77, 78], Skyrme-Faddeev model [29, 79], hydrodynamics [80], magnetohydrodynamics [81] and physics of plasma [82].

Similar knotted configurations, with stability supported by the fact that the vector field lines are self-intertwine with themselves and form a knotted-field configuration, appear in many areas of physics, including particle physics [29], fluid dynamics [30], plasma physics [31], condensed matter [32–34], and the classical field theory [35, 36]. Knotted electromagnetic field configurations were also suggested to play a role in chirally imbalanced quark-gluon plasmas [37–41]. We should especially note that similar but metastable objects are theoretically predicted in a two-component superconductor [8].

Moreover, knots can appear in exotic cases as in Maxwell theory [83] and even in Einstein theory [84].

In addition, knots are found in biological systems. The peptide chain of some globular proteins is tied into a knot during folding. For example, the paper [85] presents the dynamics of the archaic viral protein AFV3-109 depending on temperature.

Spheromaks

Solutions that have been extensively investigated in this thesis can be considered as counterparts of the Chandrasekhar-Kendall (CK) states [42], in the context of noncentrosymmetric superconductors.

The Chandrasekhar-Kendall states are divergence-free eigenvectors of the curl operator that determine the minimum-energy equilibrium configurations in magnetohydrodynamics of highly conducting, "force-free" plasmas. By "force-free" we mean systems with a magnetic field, in which there is no Lorentz force. Charged particles move in such systems along the lines of force of the magnetic field.

These states appear in various physical contexts, ranging from astrophysical plasmas [42] to nuclear fusion theory. In the latter case, the Chandrasekhar-Kendall eigenvectors are also known as Taylor states [43], which represent the relaxed minimum energy states of a plasma in a spheromak device (i.e., inside a spherical shell that confines the plasma which is counterpart of a tokamak device) and therefore are also called "spheromaks" [44, 45]. The principal difference between state in parity-broken superconductors and the Chandrasekhar-Kendall state in a conducting plasma, is that the state, which we found, are strongly localized configurations. The spatial localization of both the magnetic field and the supercurrent of investigated state originates from the Meissner effect.

The central idea of the existence of spheromak is based on an effect which generates a current along the magnetic field lines. The conserved current, flowing along the lines of the magnetic field of configuration, produces its own magnetic field, which, in turn, appears to coincide with the original magnetic field that generates the current. In other words, the solution is self-supporting: the magnetic field hosts the current which maintains the magnetic field. If the electric current were superconducting, then no electromagnetic energy would be dissipated and this self-supporting solution would have an infinite lifetime (such a kind of configuration we present in Chapters 2 and 3).

From the point of view of different plasma confinement schemes, spheromak is confinement configuration, where magnetic field produced entirely by currents flowing in the plasmas. Since spheromak has no toroidal fields at the walls, then it doesn't have external toroidal field coils. Also, since spheromaks has no coils linking the plasma, then spheromak is forming spontaneously given the appropriate initial conditions. Thus, spheromak-like configurations should occur in nature, since they result from a plasma self-organization and represent a minimum energy state towards which the plasma evolves.

Moreover, spheromaks appear in different experiments with different methods [see review [86]]. Besides, experiments were carried out to study moving spheromaks. In particular, experiments were carried out with colliding spheromaks and merging spheromaks [87, 88] and a study of a double spheromak was carried out [89].

Chapter 2

Knotted self-linked configurations in noncentrosymmetric superconductors

In this chapter, we introduce the Ginzburg-Landau (GL) model for parity breaking superconductor and derive the corresponding classical equations of motion in the London limit. We consider static, time-independent configurations of the gauge field $\boldsymbol{A}$ and the superconducting condensate ψ. We explicitly solve these equations of motion in the presence of an isolated spherical impurity and analyze properties of the corresponding solution. We discuss their explicit configurations, their energy and helicity densities. In this chapter, we call our solutions "spheromak", since the original goal of the study was to search for spheromak-like solutions in noncentrosymmetric superconductors.

2.1 Ginzburg-Landau free energy

We consider a wide class of isotropic noncentrosymmetric superconductors that are invariant under spatial rotations while possessing, at the same time, an explicitly broken discrete group of spatial inversions. The macroscopic physics of these materials can be described within the framework of the Ginzburg-Landau theory [90] supplemented with the Lifshitz term of the simplest form $\gamma \boldsymbol{j} \cdot \boldsymbol{B}$ (the first line in the Table 1.1), which clearly violates the discrete group of spatial inversions (since, from a geometric point of view, the supercurrent $\boldsymbol{j}$ is a polar vector, and the vector of the magnetic field $\boldsymbol{B}$ is axial, then the Lifshitz term changes its sign when applying the operation of spatial inversion). The Lifshitz term directly couples the magnetic field $\boldsymbol{B}$ with a current $\boldsymbol{j}$ expressed via the superconducting order parameter ψ, and the strength of the parity violation is controlled by the value of the parameter γ. This particular form of the Lifshitz term describes a class of noncentrosymmetric superconductors with a crystal

structure characterized by the chiral octahedral O point group symmetry such as, for example, Li_2Pt_3B [18, 25], Mo_3Al_2C [26, 27] and PtSbS [28].

The initial expression for describing the superconducting state in noncentrosymmetric superconductors is the Ginzburg-Landau (GL) free energy $F = \int d^3x\, \mathcal{F}$, where, despite the derivation given in the previous chapter 1.4.1, we will use the form of the density $\mathcal{F}$ in the following form

$$\mathcal{F} = \frac{\boldsymbol{B}^2}{8\pi} + k|\boldsymbol{D}\psi|^2 + \frac{\beta}{2}(|\psi|^2 - \psi_0^2)^2 + \gamma \boldsymbol{j}\cdot\boldsymbol{B}\,. \tag{2.1}$$

This form is represented by the phenomenological model presented in Chapter 5 of [21], which has an artificial unboundness of the energy from below (this will be clearly demonstrated below in this section). Nevertheless this feature of the density will not affect subsequent analytical calculations and obtained results in the London limit.

It should be noted that all subsequent formulas and analytical calculations are presented in units of $\hbar = c = 1$, where $\hbar$ is Planck's constant and c is the speed of light in vacuum.

The superconducting order parameter $\psi = |\psi|e^{i\varphi}$ is a complex single-component scalar field. It is coupled to the vector potential $\boldsymbol{A}$ of the magnetic field $\boldsymbol{B} = \boldsymbol{\nabla}\times\boldsymbol{A}$ through the covariant derivative $\boldsymbol{D} \equiv \boldsymbol{\nabla} - ie\boldsymbol{A}$, where e is a gauge coupling, which is an electric charge of the Cooper pair and is equal, respectively, to the double charge of the electron.

The first three terms in Eq. (2.1) are the standard terms of the GL free energy. The last term is the Lifshitz invariant which describes the explicit breaking of the inversion symmetry. This term directly couples the magnetic field $\boldsymbol{B}$ and the current

$$\boldsymbol{j} = 2e|\psi|^2(\boldsymbol{\nabla}\varphi - e\boldsymbol{A}) = 2e\,\mathrm{Im}\big(\psi^*\boldsymbol{D}\psi\big). \tag{2.2}$$

The prefactor γ controls the degree of inversion-symmetry breaking. In a parity even system with $\gamma = 0$, the current (2.2) gives the usual superconducting current, while in the parity-odd system with $\gamma \neq 0$, the supercurrent gets an additional contribution from the Lifshitz term [91]. Without loss of generality, we choose the parameter γ to be a positive number.

The Lifshitz term $\boldsymbol{j}\cdot\boldsymbol{B}$ is a local higher-derivative term which appears as a result of a derivative expansion of an effective Ginzburg-Landau energy. Convergence of the expansion requires such terms to be small compared to the leading terms. Therefore, below we will first consider the lowest-energy spheromak solutions including small values of the parameter γ. To highlight the qualitative features of the entire tower of the spheromak spectrum, we will also consider larger values of the parity-odd parameter γ at which the generic properties of the spheromak solutions are more pronounced.

The couplings k and β describe, respectively, the magnitude of the kinetic and potential terms of the free energy (2.1). The real-valued parameter ψ_0 sets the ab-

solute value of the superconducting condensate in the ground state in the absence of background fields.

In the case of static, time-independent field configurations, the variations of the free energy (2.1) with respect to the fields ψ^* and $\boldsymbol{A}$ give us the Ginzburg-Landau equation for the superconducting condensate and the Ampère-Maxwell equation, respectively:

$$\begin{aligned} \big[k\boldsymbol{D} + 2ie\gamma\boldsymbol{B}\big]\cdot\boldsymbol{D}\psi &= \beta(|\psi|^2-\psi_0^2)\psi\,, && \text{(2.3a)}\\ \boldsymbol{\nabla}\times\Big(\frac{\boldsymbol{B}}{4\pi}+\gamma\boldsymbol{j}\Big) &= k\boldsymbol{j}+2\gamma e^2|\psi|^2\boldsymbol{B}\,. && \text{(2.3b)} \end{aligned}$$

The London penetration depth λ_L and the coherence length ξ, respectively,

$$\lambda_L^2=\frac{1}{8\pi k e^2\psi_0^2}\,,\qquad \xi^2=\frac{k}{2\beta\psi_0}\,, \tag{2.4}$$

define the length scales of the theory. The ratio of these lengths gives the Ginzburg-Landau parameter

$$\kappa=\frac{\lambda_L}{\xi}, \tag{2.5}$$

which determines the type of the superconductivity. Superconductors of the first type have $0<\kappa<1/\sqrt{2}$, and superconductors of the second type are those with $\kappa>1/\sqrt{2}$.

2.1.1 Critical value of the parity breaking

In order to have a ground state and not fall into minus infinity for large configurations, the free energy (2.1) must have a boundness from below. To demonstrate this, we expand the kinetic term for scalar field by using the definition of the complex modulus:

$$k|\boldsymbol{D}\psi|^2=k(\boldsymbol{D}\psi)(\boldsymbol{D}\psi)^* \tag{2.6}$$

Represent one of the factors as

$$\begin{aligned} \boldsymbol{D}\psi &= (\boldsymbol{\nabla}-ie\boldsymbol{A})|\psi|e^{i\varphi}=\boldsymbol{\nabla}(|\psi|e^{i\varphi})-ie\boldsymbol{A}|\psi|e^{i\varphi}\\ &= |\psi|\boldsymbol{\nabla}e^{i\varphi}+(\boldsymbol{\nabla}|\psi|)e^{i\varphi}-ie\boldsymbol{A}|\psi|e^{i\varphi}\\ &= |\psi|(\boldsymbol{\nabla}\varphi)ie^{i\varphi}+(\boldsymbol{\nabla}|\psi|)e^{i\varphi}-ie\boldsymbol{A}|\psi|e^{i\varphi}\\ &= \Big[\boldsymbol{\nabla}|\psi|+i|\psi|\big(\boldsymbol{\nabla}\varphi-e\boldsymbol{A}\big)\Big]e^{i\varphi}\,, \end{aligned} \tag{2.7}$$

and using the expressions for the current (2.2), we can transform it to the following form:

$$\boldsymbol{D}\psi=\left(\boldsymbol{\nabla}|\psi|+i\frac{\boldsymbol{j}}{2e|\psi|}\right)e^{i\varphi}. \tag{2.8}$$

Since the covariant derivative has the form $\boldsymbol{D}\equiv\boldsymbol{\nabla}-ie\boldsymbol{A}$, then the complex conjugate expression is $\boldsymbol{D}^*=\boldsymbol{\nabla}+ie\boldsymbol{A}$, and

$$(\boldsymbol{D}\psi)^*=\left(\boldsymbol{\nabla}|\psi|-i\frac{\boldsymbol{j}}{2e|\psi|}\right)e^{-i\varphi}\,. \tag{2.9}$$

The kinetic term (2.6) is expanded into two terms:

$$k|\boldsymbol{D}\psi|^2 = k\left(\boldsymbol{\nabla}|\psi| + i\frac{\boldsymbol{j}}{2e|\psi|}\right)\left(\boldsymbol{\nabla}|\psi| - i\frac{\boldsymbol{j}}{2e|\psi|}\right) = k\left(\boldsymbol{\nabla}|\psi|\right)^2 + k\frac{\boldsymbol{j}^2}{4e^2|\psi|^2}\,. \quad (2.10)$$

The next step is to complete the square from two terms, from the energy of the magnetic field and the Lifshitz invariant:

$$\begin{aligned}\frac{\boldsymbol{B}^2}{8\pi} + \gamma\boldsymbol{j}\cdot\boldsymbol{B} &= \frac{1}{8\pi}\left(\boldsymbol{B}^2 + 4\pi\gamma\boldsymbol{j}\cdot\boldsymbol{B} + (4\pi\gamma)^2\boldsymbol{j}^2 - (4\pi\gamma)^2\boldsymbol{j}^2\right)\\ &= \frac{1}{8\pi}\left(\boldsymbol{B} + 4\pi\gamma\boldsymbol{j}\right)^2 - 2\pi\gamma^2\boldsymbol{j}^2\,. \end{aligned} \quad (2.11)$$

Combining it all together, we obtain

$$\mathcal{F} = \frac{1}{8\pi}\left(\boldsymbol{B} + 4\pi\gamma\boldsymbol{j}\right)^2 + 2\pi\boldsymbol{j}^2\left(\frac{k}{8\pi e^2|\psi|^2} - \gamma^2\right) + k\left(\boldsymbol{\nabla}|\psi|\right)^2 + \frac{\beta}{2}(|\psi|^2 - \psi_0^2)^2. \quad (2.12)$$

It can be seen that only the second term is not a positively defined quantity. We note that the strength of the parity-odd parameter γ cannot exceed a critical value

$$0 \leqslant \gamma < \sqrt{\frac{k}{8\pi e^2|\psi|^2}}\,. \quad (2.13)$$

In the London Limit, the value of the superconducting order parameter is a constant $|\psi| = \psi_0$. Thus, this condition(2.13) can be reduced to

$$0 \leqslant \gamma < \gamma_\star = k\lambda_L\,, \quad (2.14)$$

where we use the expression for the London penetration depth (2.4).

The bound (2.13) implies that the parity breaking should not be too strong in order to ensure the stability of the Ginzburg-Landau model with a minimal number of terms (2.1). One may generalize the model (2.1) and include a higher-order term that will stabilize the ground state even for stronger parity-odd violation. One of the possible generalizations is to add the parity-event term $|\phi|^2\boldsymbol{B}^2$ which couples the local magnetic field energy $\boldsymbol{B}^2$ to the superconducting density $|\phi|^2$, as it was done in Ref. [58]. In this chapter, we will work in the London limit in which the difference between these two formulations of the parity-odd system disappears. These models may be treated at the same basis up to redefinition of free energy parameters.

2.2 London limit

2.2.1 Field equations

In the London limit, $\beta \to \infty$, the superconducting condensate gets frozen in the radial direction, $|\psi| = \psi_0$, while its phase φ remains dynamically active. The second London

equation, which in our case is obtained by taking the curl operator from the expression for the supercurrent (2.2)

$$\boldsymbol{j} = 2e\psi_0^2\,(\boldsymbol{\nabla}\varphi - e\boldsymbol{A})\,, \tag{2.15}$$

reads as follows:

$$\boldsymbol{B} = \frac{1}{e}\left(\boldsymbol{\nabla}\times\boldsymbol{\nabla}\varphi - \frac{1}{2e\psi_0^2}\boldsymbol{\nabla}\times\boldsymbol{j}\right)\,. \tag{2.16}$$

As a result, the Ampère-Maxwell equation (2.3b) may conveniently be rewritten as follows:

$$\lambda_L^2\boldsymbol{\nabla}\times\boldsymbol{\nabla}\times\boldsymbol{j} + \boldsymbol{j} - 2\frac{\gamma}{k}\boldsymbol{\nabla}\times\boldsymbol{j} = S\,, \tag{2.17}$$

where the source term on the right hand side,

$$\begin{aligned} S &= \frac{1}{4\pi k e}\Big(\boldsymbol{\nabla}\times\boldsymbol{\nabla}\times\boldsymbol{\nabla}\varphi - \frac{\gamma}{k\lambda_L^2}\boldsymbol{\nabla}\times\boldsymbol{\nabla}\varphi\Big) \\ &= \frac{\Phi_0}{4\pi k}\Big(\boldsymbol{\nabla}\times\boldsymbol{v} - \frac{\gamma}{k\lambda_L^2}\boldsymbol{v}\Big), \end{aligned} \tag{2.18}$$

is expressed via the vortex density,

$$\boldsymbol{v} = \frac{1}{2\pi}\boldsymbol{\nabla}\times\boldsymbol{\nabla}\varphi, \tag{2.19}$$

with $\Phi_0 = 2\pi/e$ being the elementary flux quantum.

The position $x = \boldsymbol{x}_a(\tau)$ of vortex $a = 1, 2, \ldots N$ with the vorticity n_a in a generic vortex ensemble may be parameterized via the length variable τ. Then the vorticity (2.19) takes the form:

$$\boldsymbol{v}(\boldsymbol{x}) = \sum_a n_a \int d\tau \frac{\partial\bar{\boldsymbol{x}}_a(\tau)}{\partial\tau}\delta\big(\boldsymbol{x} - \bar{\boldsymbol{x}}_a(\tau)\big). \tag{2.20}$$

It is convenient, following [57], to work in the dimensionless units with the rescaled spatial coordinates and the appropriately rescaled derivatives, respectively:

$$\boldsymbol{r} = \boldsymbol{x}/\lambda_L, \qquad \boldsymbol{\nabla}_{\boldsymbol{r}} = \lambda_L\boldsymbol{\nabla}. \tag{2.21}$$

The equation of motion takes the following form:

$$\boldsymbol{\nabla}_{\boldsymbol{r}}\times\boldsymbol{\nabla}_{\boldsymbol{r}}\times\boldsymbol{j} + \boldsymbol{j} - 2\Gamma\boldsymbol{\nabla}_{\boldsymbol{r}}\times\boldsymbol{j} = \tfrac{\Phi_0}{4\pi k\lambda_L}\Big(\boldsymbol{\nabla}_{\boldsymbol{r}}\times\boldsymbol{v} - \Gamma\boldsymbol{v}\Big), \tag{2.22}$$

where the relation

$$\boldsymbol{B}(\boldsymbol{r}) = \Phi_0\boldsymbol{v} - 4\pi k\lambda_L\boldsymbol{\nabla}_{\boldsymbol{r}}\times\boldsymbol{j}, \tag{2.23}$$

determines the magnetic field according to Eq. (2.16). The dimensionless parity breaking coupling,

$$\Gamma = \frac{\gamma}{k\lambda_L}, \tag{2.24}$$

according to the previous analysis (2.14), satisfies the stability bound (for definiteness, we take Γ to be a positive parameter):

$$0 \leqslant \Gamma < 1. \tag{2.25}$$

First, we consider free spheromak solutions in a parity-odd superconductor in the absence of vortices, $\boldsymbol{v} = 0$. The current $\boldsymbol{j}$ in such configurations is determined by Eq. (2.17) with vanishing right-hand side:

$$\boldsymbol{\nabla}_{\boldsymbol{r}} \times \boldsymbol{\nabla}_{\boldsymbol{r}} \times \boldsymbol{j} + \boldsymbol{j} - 2\Gamma \boldsymbol{\nabla}_{\boldsymbol{r}} \times \boldsymbol{j} = 0, \tag{2.26}$$

while the magnetic field $\boldsymbol{B}$ is given by the appropriate modification of Eq. (2.23):

$$\boldsymbol{B}(\boldsymbol{r}) = -4\pi k \lambda_L \boldsymbol{\nabla}_{\boldsymbol{r}} \times \boldsymbol{j}. \tag{2.27}$$

and $\boldsymbol{B} = (\lambda_L)^{-1} \boldsymbol{\nabla}_{\boldsymbol{r}} \times \boldsymbol{A}$.

The Ginzburg-Landau (GL) free energy, in turn, in the London limit, in the absence of vortices and in dimensionless coordinates, takes the expression

$$F = \int d^3x\, \mathcal{F} = 2\pi k^2 \lambda_L^5 \int d^3\boldsymbol{r} \Big(\big(\boldsymbol{\nabla}_{\boldsymbol{r}} \times \boldsymbol{j}\big)^2 + \big(\boldsymbol{j}\big)^2 - 2\Gamma \boldsymbol{j} \cdot \boldsymbol{\nabla}_{\boldsymbol{r}} \times \boldsymbol{j} \Big). \tag{2.28}$$

Since we are interested in compact solution of Eq. (2.26), it is convenient to represent the angular dependence of these solutions in terms of the vector spherical basis $\boldsymbol{Z}_{lm} = (\boldsymbol{Y}_{lm}, \boldsymbol{\Psi}_{lm}, \boldsymbol{\Phi}_{lm})$ where $l = 0, 1, 2, \ldots$ is the integer-valued momentum and $m \equiv m_z \in \mathbb{Z}$ with $-l \leqslant m \leqslant l$ is the projection of the momentum on the z axis.

For the vector spherical harmonics, we choose the parameterization of Ref. [92]:

$$\boldsymbol{Y}_{lm}(\hat{\boldsymbol{r}}) = Y_{lm}(\hat{\boldsymbol{r}}) \hat{\boldsymbol{r}}\,, \tag{2.29a}$$

$$\boldsymbol{\Psi}_{lm}(\hat{\boldsymbol{r}}) = r \boldsymbol{\nabla} Y_{lm}(\hat{\boldsymbol{r}})\,, \tag{2.29b}$$

$$\boldsymbol{\Phi}_{lm}(\hat{\boldsymbol{r}}) = \boldsymbol{r} \times \boldsymbol{\nabla} Y_{lm}(\hat{\boldsymbol{r}})\,, \tag{2.29c}$$

which is defined via the scalar spherical harmonics $Y_{lm}(\hat{\boldsymbol{r}})$. Both scalar spherical harmonics Y_{lm} and the set of vector spherical harmonics $\boldsymbol{Z}_{lm}$ depend on the angular coordinate encoded in the unit vector $\hat{\boldsymbol{r}} \equiv \boldsymbol{r}/r$. They do not depend on the radial coordinate r. Certain useful properties of both scalar and vector spherical harmonics are presented in Appendix A.

We represent a general spheromak field of the (l, m) harmonics as follows (with $l = 0, 1, \ldots$ and $|m| \leqslant l$):

$$\boldsymbol{j}_{lm}(\boldsymbol{r}) = \sum_{\boldsymbol{Z} = \boldsymbol{Y}, \boldsymbol{\Psi}, \boldsymbol{\Phi}} j_l^{\boldsymbol{Z}}(r)\, \boldsymbol{Z}_{lm}(\hat{\boldsymbol{r}}), \tag{2.30}$$

where $j_l^{\boldsymbol{Z}}$ with $\boldsymbol{Z} = \boldsymbol{Y}, \boldsymbol{\Psi}, \boldsymbol{\Phi}$ are certain functions of the radial variable r.

As we will see below, the structure of the equations of motion implies that that the radial functions $j_l^{\boldsymbol{Z}}$ do not depend on the angular variable m. Therefore these functions are the same for all solutions with different projections m and the same angular momentum l. In other words, if we find a solution for a certain (l, m) pair, we also automatically uncover the whole set of $2l+1$ solutions for the fixed total angular momentum l characterized by the same radial functions.

The magnetic field can also be given in the basis of vector spherical harmonics similarly to the electric current (2.30):

$$\boldsymbol{B}_{lm} = \sum_{\boldsymbol{Z}=\boldsymbol{Y},\boldsymbol{\Psi},\boldsymbol{\Phi}} B_l^{\boldsymbol{Z}}(r)\, \boldsymbol{Z}_{lm}(\hat{\boldsymbol{r}})\,, \tag{2.31}$$

where the magnetic radial functions $B_l^{\boldsymbol{Z}}$ are related to the radial functions $j_l^{\boldsymbol{Z}}$ via Eq. (2.27)

Substituting ansatz (2.30) into the London equation (2.26), and using the orthogonality relations (A.7) and expression for the curl operator in terms VSH (A.13), we get the following set of differential equations for the radial functions $j_l^{\boldsymbol{Z}}$:

$$\begin{aligned}
-\frac{l(l+1)}{r}\left(\frac{j_l^{\boldsymbol{Y}}}{r} + 2\Gamma j_l^{\boldsymbol{\Phi}}\right) + \frac{l(l+1)}{r}\left(\frac{d}{dr} + \frac{1}{r}\right) j_l^{\boldsymbol{\Psi}} - j_l^{\boldsymbol{Y}} &= 0, \\
\left(\frac{d^2}{dr^2} + \frac{2}{r}\frac{d}{dr}\right) j_l^{\boldsymbol{\Psi}} - \frac{1}{r}\frac{d}{dr} j_l^{\boldsymbol{Y}} - 2\Gamma\left(\frac{d}{dr} + \frac{1}{r}\right) j_l^{\boldsymbol{\Phi}} - j_l^{\boldsymbol{\Psi}} &= 0, \\
\left(\frac{d^2}{dr^2} + \frac{2}{r}\frac{d}{dr} - \frac{l(l+1)}{r^2}\right) j_l^{\boldsymbol{\Phi}} - 2\Gamma\frac{j_l^{\boldsymbol{Y}}}{r} + 2\Gamma\left(\frac{d}{dr} + \frac{1}{r}\right) j_l^{\boldsymbol{\Psi}} - j_l^{\boldsymbol{\Phi}} &= 0,
\end{aligned} \tag{2.32}$$

which are valid everywhere except for the origin $r = 0$.

The conservation of electric charge implies the closeness of the current lines,

$$\boldsymbol{\nabla} \cdot \boldsymbol{j} = 0, \tag{2.33}$$

which gives another useful equality if we use the expression for the divergence in the VSH basis (A.12):

$$\frac{d}{dr} j_l^{\boldsymbol{Y}} + \frac{2}{r} j_l^{\boldsymbol{Y}} - \frac{l(l+1)}{r} j_l^{\boldsymbol{\Psi}} = 0. \tag{2.34}$$

It is also convenient to use the operator

$$\mathcal{D} = \frac{1}{r}\frac{d}{dr} r\,, \tag{2.35}$$

to rewrite the system of linear equations (2.32) and (2.34) in a more compact form:

$$l(l+1)\left(\mathcal{D} j_l^{\boldsymbol{\Psi}} - 2\Gamma j_l^{\boldsymbol{\Phi}} - \frac{j_l^{\boldsymbol{Y}}}{r}\right) - r j_l^{\boldsymbol{Y}} = 0, \tag{2.36a}$$

$$\left(\mathcal{D}^2 - 1\right) j_l^{\boldsymbol{\Psi}} - \mathcal{D}\frac{j_l^{\boldsymbol{Y}}}{r} - 2\Gamma \mathcal{D} j_l^{\boldsymbol{\Phi}} = 0, \tag{2.36b}$$

$$\left(\mathcal{D}^2 - \frac{l(l+1)}{r^2} - 1\right) j_l^{\boldsymbol{\Phi}} + 2\Gamma \mathcal{D} j_l^{\boldsymbol{\Psi}} - \frac{2\Gamma}{r} j_l^{\boldsymbol{Y}} = 0\,, \tag{2.36c}$$

$$\mathcal{D}(r j_l^{\boldsymbol{Y}}) - l(l+1) j_l^{\boldsymbol{\Psi}} = 0. \tag{2.36d}$$

From (2.36d) we can obtain the dependence of the $j_l^{\mathbf{\Psi}}$ component on the $j_l^{\boldsymbol{Y}}$:

$$j_l^{\mathbf{\Psi}}(r) \;=\; \frac{1}{l(l+1)}\mathcal{D}\Big(r j_l^{\boldsymbol{Y}}(r)\Big)\,. \tag{2.37}$$

Further, the first equation of the system (2.36a) gives us an expression for the $j_l^{\mathbf{\Phi}}$ component in terms, once again, of the $j_l^{\boldsymbol{Y}}$:

$$\begin{aligned} j_l^{\mathbf{\Phi}}(r) \;&=\; \frac{1}{2\Gamma}\Big[\mathcal{D} j_l^{\mathbf{\Psi}}(r) - \Big(\frac{1}{r} + \frac{r}{l(l+1)}\Big) j_l^{\boldsymbol{Y}}(r)\Big] \\ &=\; \frac{1}{2\Gamma}\Big[\frac{1}{l(l+1)}\Big(\mathcal{D}^2 - 1\Big)\big(r j_l^{\boldsymbol{Y}}(r)\big) - \frac{1}{r} j_l^{\boldsymbol{Y}}(r)\Big]\,. \end{aligned} \tag{2.38}$$

Finally, the combination of the expressions (2.37), (2.38) and equation (2.36c) gives us a fourth-order differential equation for the $j_l^{\boldsymbol{Y}} = j_l^{\boldsymbol{Y}}(r)$ radial component:

$$\begin{aligned} 0 \;&=\; (j_l^{\boldsymbol{Y}})'''' + \frac{8}{r}(j_l^{\boldsymbol{Y}})''' + 2\Big[2\Gamma^2 - 1 + \frac{1}{r^2}\big(6 - l(l+1)\big)\Big](j_l^{\boldsymbol{Y}})'' \\ &+\; \frac{4}{r}\Big[4\Gamma^2 - 2 - \frac{l(l+1)}{r^2}\Big](j_l^{\boldsymbol{Y}})' \\ &+\; \frac{1}{r^2}\Big[\big(2 - l(l+1)\big)\big(4\Gamma^2 - 2 - \frac{l(l+1)}{r^2}\big) + r^2\Big] j_l^{\boldsymbol{Y}}, \end{aligned} \tag{2.39}$$

where each prime denotes a partial derivative with respect to r. Substitution of expressions (2.37) and (2.38) in the remaining equation of the system (2.36b) gives us an expression that is identically equal to zero.

As a result, finding a solution to this equation (2.39), we automatically obtain explicit expressions for the remaining two components (2.37) and (2.38).

2.2.2 Compact analytical vortex-free spheromak solutions

In this section we demonstrate that the system of equations (2.36) may be solved explicitly only for the low orbital momentum $l = 1$, for all projections $m \equiv m_z$ and for all values of the parity-odd parameter Γ. In addition, the explicit spheromak solutions may also be found for the specific value of $\Gamma = 1/\sqrt{2}$ for all angular numbers l and m.

No compact solutions for $l = 0$ and $m = 0$

Compact solutions with the lowest possible orbital momentum $l = 0$ do not exist. Indeed, Eq. (2.36a) has the solution $j^{\boldsymbol{Y}} = 0$. Since the purely angular functions at $l = 0$ are zero (A.15) ($\mathbf{\Psi}_{00} = \mathbf{\Phi}_{00} = 0$), the $(l, m) = (0, 0)$ solution is vanishing identically, $\boldsymbol{j}_{00} = 0$ and $\boldsymbol{B}_{00} = 0$.

Solutions for $l = 1$ and $m = -1, 0, 1$

The system of equations (2.36) with $l = 1$ can be solved explicitly. In this case, the equations defining the current components ((2.37), (2.38) and (2.39)) take the following

form:

$$
\begin{aligned}
j^{\mathbf{\Psi}_1}(r) &= \frac{r}{2}(j_1^{\boldsymbol{Y}})' + j_1^{\boldsymbol{Y}}\,, && \text{(2.40a)}\\
j_1^{\mathbf{\Phi}}(r) &= \frac{1}{4\Gamma}\Big[r(j_1^{\boldsymbol{Y}})'' + 4(j_1^{\boldsymbol{Y}})' - r j_1^{\boldsymbol{Y}}\Big]\,, && \text{(2.40b)}\\
0 &= (j_1^{\boldsymbol{Y}})'''' + \frac{8}{r}(j_1^{\boldsymbol{Y}})''' + 2\Big(2\Gamma^2 - 1 + \frac{4}{r^2}\Big)(j_1^{\boldsymbol{Y}})''\\
&+ \frac{8}{r}\Big(2\Gamma^2 - 1 - \frac{1}{r^2}\Big)(j_1^{\boldsymbol{Y}})' + j_1^{\boldsymbol{Y}}\,. && \text{(2.40c)}
\end{aligned}
$$

The analytical solution of the equation (2.40c) includes four independent constants $\mathcal{A}_i$ and has the form:

$$
\begin{aligned}
j_1^{\boldsymbol{Y}}(r) &= \mathcal{A}_1\frac{\sqrt{-a-r^2}}{r^3}\exp\left\{+\sqrt{-b}\left[r - \sqrt{a}\arctan\left(\frac{r}{\sqrt{a}}\right)\right]\right\}\\
&+ \mathcal{A}_2\frac{\sqrt{-a-r^2}}{r^3}\exp\left\{-\sqrt{-b}\left[r - \sqrt{a}\arctan\left(\frac{r}{\sqrt{a}}\right)\right]\right\}\\
&+ \mathcal{A}_3\frac{\sqrt{-b-r^2}}{r^3}\exp\left\{+\sqrt{-a}\left[r - \sqrt{b}\arctan\left(\frac{r}{\sqrt{b}}\right)\right]\right\}\\
&+ \mathcal{A}_4\frac{\sqrt{-b-r^2}}{r^3}\exp\left\{-\sqrt{-a}\left[r - \sqrt{b}\arctan\left(\frac{r}{\sqrt{b}}\right)\right]\right\}\,,
\end{aligned}
\qquad \text{(2.41)}
$$

where

$$
\begin{aligned}
a(\Gamma) &= 2\Gamma^2 - 1 - 2\Gamma\sqrt{\Gamma^2 - 1}, && \text{(2.42a)}\\
b(\Gamma) &= 2\Gamma^2 - 1 + 2\Gamma\sqrt{\Gamma^2 - 1}. && \text{(2.42b)}
\end{aligned}
$$

Since the solution must satisfy the finite energy condition (2.25), then in case of $0 < \Gamma < 1$ we have

$$
\begin{aligned}
a(\Gamma) &= 2\Gamma^2 - 1 - 2i\Gamma\sqrt{1 - \Gamma^2}, && \text{(2.43a)}\\
b(\Gamma) &= 2\Gamma^2 - 1 + 2i\Gamma\sqrt{1 - \Gamma^2}. && \text{(2.43b)}
\end{aligned}
$$

After several mathematical transformations, we easily find that

$$
\begin{aligned}
j_1^{\boldsymbol{Y}}(r) = &- (\mathcal{A}_1 + \mathcal{A}_2)\frac{e^{-\sqrt{1-\Gamma^2}r}}{r^3}\Big[(r + \sqrt{1-\Gamma^2})\cos(\Gamma r) - \Gamma\sin(\Gamma r)\Big]\\
&- i(\mathcal{A}_1 - \mathcal{A}_2)\frac{e^{-\sqrt{1-\Gamma^2}r}}{r^3}\Big[(r + \sqrt{1-\Gamma^2})\sin(\Gamma r) + \Gamma\cos(\Gamma r)\Big]\,, \qquad \text{(2.44)}
\end{aligned}
$$

where we set the constants $\mathcal{A}_3$ and $\mathcal{A}_4$ equal to zero in order to obtain a solution that does not diverge at infinity. Also we can choose parameters $\mathcal{A}_1$ and $\mathcal{A}_2$ in such a way ($\mathcal{A}_1 + \mathcal{A}_2 = -\mathcal{A}\Gamma$ and $i(\mathcal{A}_1 - \mathcal{A}_2) = \mathcal{A}\sqrt{1-\Gamma^2}$) that the $j_1^{\boldsymbol{Y}}$ component of the solution is globally minimized both in infrared and ultraviolet limits. Finally we get the following

radial functions:

$$
\begin{aligned}
j_1^{\boldsymbol{Y}}(r) &= -\frac{\mathcal{A}\,\Gamma^2}{r}e^{-\sqrt{1-\Gamma^2}r}\left[j_1(\Gamma r)+\frac{\sqrt{1-\Gamma^2}}{\Gamma}j_0(\Gamma r)\right],\\
j_1^{\boldsymbol{\Psi}}(r) &= \frac{\mathcal{A}\,\Gamma^2}{2}e^{-\sqrt{1-\Gamma^2}r}\left[\left(\frac{1}{r}+\sqrt{1-\Gamma^2}\right)j_1(\Gamma r)\right.\\
&\qquad\left.+\frac{1-2\Gamma^2}{\Gamma}j_0(\Gamma r)+\sqrt{1-\Gamma^2}y_0(\Gamma r)\right], \qquad (2.45)\\
j_1^{\boldsymbol{\Phi}}(r) &= \frac{\mathcal{A}\,\Gamma^2}{2}e^{-\sqrt{1-\Gamma^2}r}\left[\left(\frac{1}{r}+\sqrt{1-\Gamma^2}\right)j_0(\Gamma r)\right.\\
&\qquad\left.-\frac{1-2\Gamma^2}{\Gamma}y_0(\Gamma r)-\sqrt{1-\Gamma^2}y_1(\Gamma r)\right],
\end{aligned}
$$

where j_n and y_n are the spherical Bessel functions:

$$
\begin{aligned}
j_0(x)&=\frac{\sin x}{x}, \qquad & j_1(x)&=\frac{\sin x}{x^2}-\frac{\cos x}{x},\\
y_0(x)&=-\frac{\cos x}{x}, \qquad & y_1(x)&=-\frac{\cos x}{x^2}-\frac{\sin x}{x}. \qquad (2.46)
\end{aligned}
$$

The magnetic field (2.27) of the $l=1$ spheromak solution (2.45) has the following form:

$$
\begin{aligned}
B_1^{\boldsymbol{Y}}(r) &= 4\pi k\lambda_L\frac{\mathcal{A}\,\Gamma^2}{r}e^{-\sqrt{1-\Gamma^2}r}\left[j_0(\Gamma r)\left(\frac{1}{r}+\sqrt{1-\Gamma^2}\right)\right.\\
&\quad\left.-\frac{1-2\Gamma^2}{\Gamma}y_0(\Gamma r)-\sqrt{1-\Gamma^2}y_1(\Gamma r)\right],\\
B_1^{\boldsymbol{\Psi}}(r) &= 2\pi k\lambda_L\mathcal{A}\,\Gamma^2e^{-\sqrt{1-\Gamma^2}r}\left[-j_0(\Gamma r)(1-\Gamma^2)-j_1(\Gamma r)\Gamma\left(\frac{1}{r}+\sqrt{1-\Gamma^2}\right)\right.\\
&\quad+y_0(\Gamma r)\frac{1}{\Gamma}\left(\frac{2\Gamma^2-1}{r}+\sqrt{1-\Gamma^2}\left(1-3\Gamma^2\right)\right)\\
&\quad\left.+y_1(\Gamma r)\left(2-3\Gamma^2+\frac{\sqrt{1-\Gamma^2}}{r}\right)\right], \qquad (2.47)\\
B_1^{\boldsymbol{\Phi}}(r) &= 2\pi k\lambda_L\mathcal{A}\,\Gamma^2e^{-\sqrt{1-\Gamma^2}r}\left[j_1(\Gamma r)\left(\frac{2\sqrt{1-\Gamma^2}}{r}+2-3\Gamma^2\right)\right.\\
&\quad-j_0(\Gamma r)\frac{1}{r\Gamma}\left((1-\Gamma^2)+\sqrt{1-\Gamma^2}\left(\frac{2}{r}-r(1-3\Gamma^2)\right)\right)\\
&\quad\left.-y_0(\Gamma r)\sqrt{1-\Gamma^2}\left(\frac{1}{r}-\sqrt{1-\Gamma^2}\right)+y_1(\Gamma r)\Gamma\sqrt{1-\Gamma^2}\right].
\end{aligned}
$$

The parameter $\mathcal{A}$ determines the amplitude of the current (2.45) and the magnetic field (2.47). This parameter $\mathcal{A}$ is a dimensional quantity in these expressions and it has the dimensionality [length^{-3}]. Due to the linear nature of Eqs. (2.26) and (2.27), the parameter $\mathcal{A}$ determines the degeneracy of the superconducting spheromak solution. This fact implies that, contrary to the Abrikosov vortex solutions, the magnitude of the magnetic field in the spheromak solutions can take arbitrary values. In other words, the electric current (2.45) and, consequently, the associated magnetic field (2.47), may

be made arbitrarily small. This property is contrasted with the Abrikosov vortex solutions in the London limit of the same superconductor, for which the magnetic field in any fixed point is quantized in term of an integer number $n \in \mathbb{Z}$ and fixed by other parameters of the theory. Notice also that due to the closeness of the magnetic field lines and the compactness of the spheromak solution, the magnetic flux of the solution piercing any cross-section of the superconducting spheromak is strictly zero. This property highlights the principal difference between the spheromak solution and the Abrikosov vortices.

The solutions show that the spheromaks are localized solutions with the dimensionless size $\tilde{L} = L/\lambda_L$ which can be read off from the exponential tail of the solutions:

$$\tilde{L} = \frac{1}{\sqrt{1-\Gamma^2}}, \qquad \text{or} \qquad L = \frac{k\lambda_L^2}{\sqrt{k^2\lambda_L^2 - \gamma^2}}. \tag{2.48}$$

As soon the parity-breaking parameter approaches the critical value $\Gamma = 1$, the size of the spheromak diverges in agreement with the already established stability bound (2.25). Notice that the physically meaningful values of this parameter that are consistent with the GL expansion are small: $\Gamma \ll 1$.

The structure of the explicit solution (2.45) and (2.47) implies that it is convenient to introduce the angle θ_Γ that measures the degree of the parity violation in the noncentrosymmetric superconductor:

$$\Gamma = \sin\theta_\Gamma, \qquad 0 \leqslant \theta_\Gamma \leqslant \frac{\pi}{2}. \tag{2.49}$$

Using the parity-odd angle (2.49) together with Eq. (2.46) and applying the simplest trigonometric identities, we get the following, more compact representation of the electric current:

$$\begin{aligned}
j_1^{\mathbf{Y}}(r) &= -\frac{\mathcal{A}}{r^2} e^{-r\cos\theta_\Gamma}\left[\frac{1}{r}\sin(r\sin\theta_\Gamma) + \sin\big(r\sin\theta_\Gamma - \theta_\Gamma\big)\right], \\
j_1^{\mathbf{\Psi}}(r) &= \frac{\mathcal{A}}{2r^2} e^{-r\cos\theta_\Gamma}\left[\frac{1}{r}\sin(r\sin\theta_\Gamma)\right. \\
&\qquad \left. + \sin(r\sin\theta_\Gamma - \theta_\Gamma) + r\sin\left(r\sin\theta_\Gamma - 2\theta_\Gamma\right)\right], \\
j_1^{\mathbf{\Phi}}(r) &= \frac{\mathcal{A}}{2r^2} e^{-r\cos\theta_\Gamma}\Big[\cos(r\sin\theta_\Gamma - \theta_\Gamma) + r\cos(r\sin\theta_\Gamma - 2\theta_\Gamma)\Big],
\end{aligned} \tag{2.50}$$

and the magnetic field:

$$\begin{aligned}
B_1^{\mathbf{Y}}(r) &= 4\pi k\lambda_L \frac{\mathcal{A}}{r^2} e^{-r\cos\theta_\Gamma}\left[\cos(r\sin\theta_\Gamma - 2\theta_\Gamma) + \frac{1}{r}\cos(r\sin\theta_\Gamma - \theta_\Gamma)\right], \\
B_1^{\mathbf{\Psi}}(r) &= -2\pi k\lambda_L \frac{\mathcal{A}}{r^2} e^{-r\cos\theta_\Gamma}\left[r\cos(r\sin\theta_\Gamma - 3\theta_\Gamma)\right. \\
&\qquad \left. + \cos(r\sin\theta_\Gamma - 2\theta_\Gamma) + \frac{1}{r}\cos(r\sin\theta_\Gamma - \theta_\Gamma)\right], \\
B_1^{\mathbf{\Phi}}(r) &= 2\pi k\lambda_L \frac{\mathcal{A}}{r^2} e^{-r\cos\theta_\Gamma}\Big[r\sin(r\sin\theta_\Gamma - 3\theta_\Gamma) + \sin(r\sin\theta_\Gamma - 2\theta_\Gamma)\Big].
\end{aligned} \tag{2.51}$$

Three-dimensional visualization of vector lines of the current $\boldsymbol{j}_1$ for the case $\Gamma = 0.5$ is shown in Fig. 2.1, where one may notice a compact double-tori structure of knotted lines. At the same time, the following Figure 2.2 shows individual current density lines, which together give the complete knotted solution shown before in the Fig. 2.1

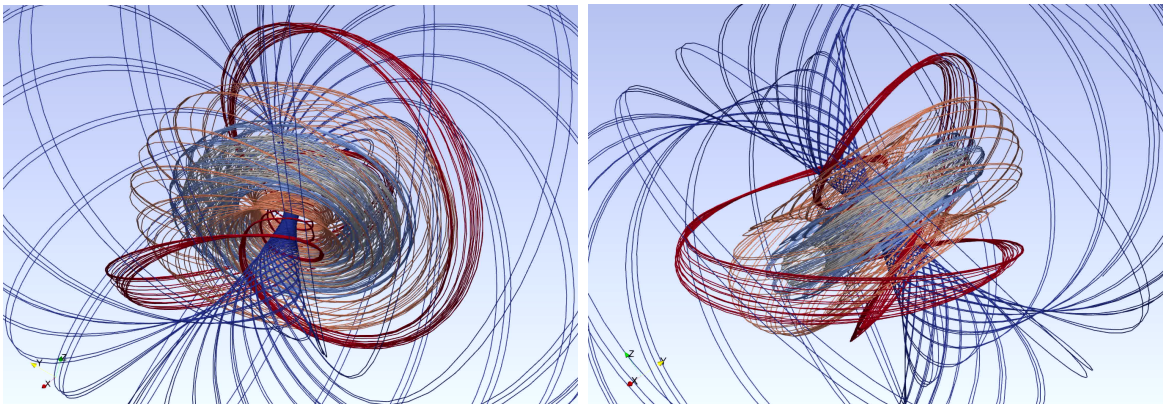

(a) (b)

Figure 2.1: Three-dimensional distributions of vector current lines in a bulk of noncentrosymmtric superconductor for two different points of view in the case of the parameter $\Gamma = 0.5$.

The configurations of the electric current and magnetic field with the angular momentum $l = 1$ and the projections $m = 0, \pm 1$ are given by Eqs. (2.30) and (2.31), respectively, where the radial functions are shown in Eqs. (2.50) and (2.51). The explicit form of the $\boldsymbol{Z}_{lm}$ harmonics is presented in Eq. (A.16) in Appendix A. Since the $m \neq 0$ harmonics are complex functions, the currents (2.30) and magnetic fields (2.31) of the spheromak solutions can be chosen as the real part of the vector harmonics, $\mathrm{Re}\,\boldsymbol{Z}_{lm}$. The imaginary part of the same $m \neq 0$ harmonics does not give us a new spheromak solution as one can show that the real and imaginary parts are related to each other by a $\pi/(2m)$ rotation about the z axis and, consequently, correspond to the same solution.

Since both the current (2.50) and the magnetic field (2.51) of the spheromak solutions are proportional to a non-quantized real-valued amplitude $\mathcal{A}$, the energy of a spheromak solution – which is quadratic both in the current $\boldsymbol{j}$ and the magnetic field $\boldsymbol{B}$ – can be made arbitrarily small thus facilitating its emergence as compact field configurations in the parity-odd superconductors. However in the London limit, the total energy of the spheromak is divergent due to contributions coming from a region near the spheromak's core.

The total energy of the $(l, m) = (1, 0)$ and $(l, m) = (1, \pm 1)$ spheromak solution has

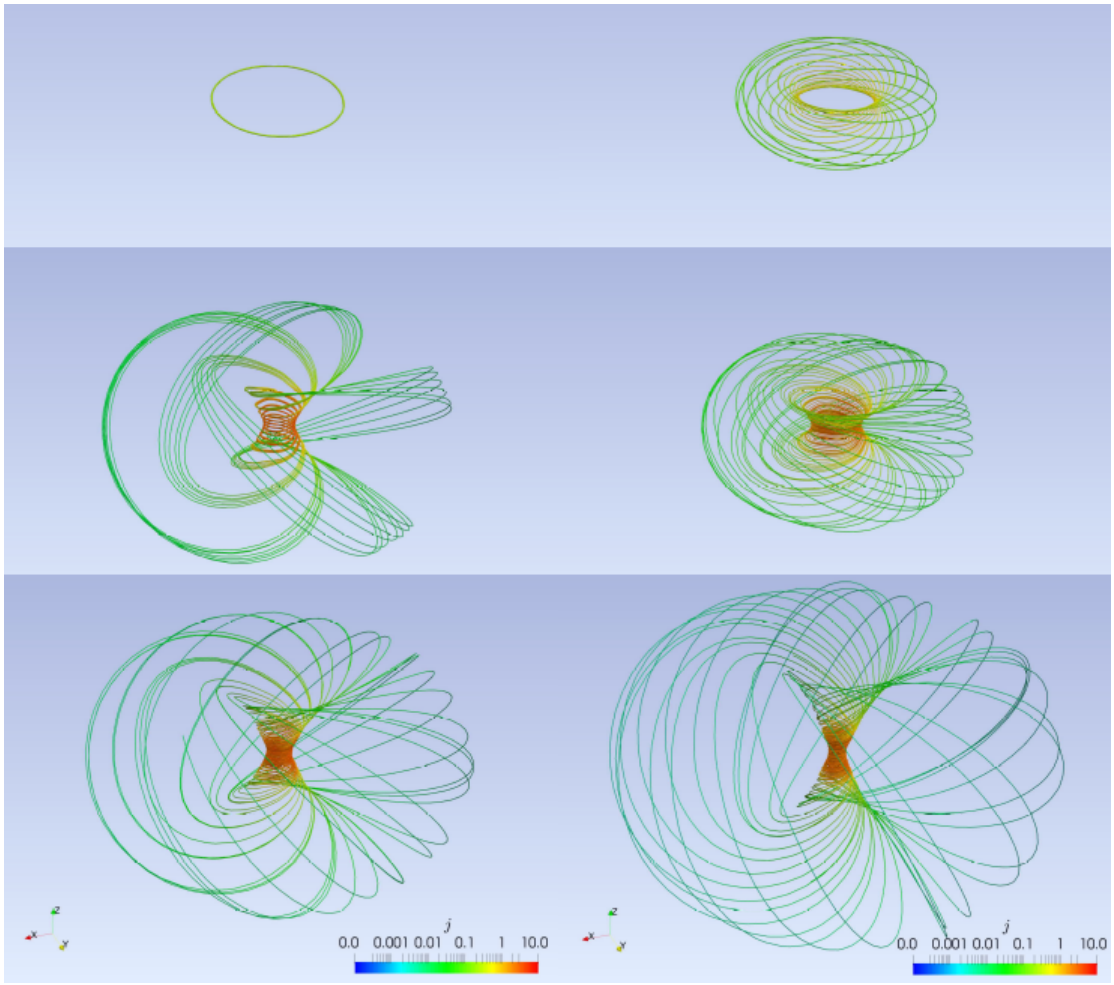

Figure 2.2: Multiple streamlines of the current density $\boldsymbol{j}_1$ for different starting points. Entanglement and intertwinning of these lines gives us the complete configuration shown in the Fig. 2.1.

the following form:

$$\begin{aligned}
\mathcal{E}_1(\tilde{a}_{\rm UV}) &= 2\pi k^2\lambda_L^5\int_{\tilde{a}_{\rm UV}}^{\infty} d^3\boldsymbol{r}\Big(\left(\boldsymbol{\nabla}_{\boldsymbol{r}}\times\boldsymbol{j}\right)^2+\left(\boldsymbol{j}\right)^2-2\Gamma\boldsymbol{j}\cdot\boldsymbol{\nabla}_{\boldsymbol{r}}\times\boldsymbol{j}\Big)\\
&= \pi k^2\lambda_L^5\mathcal{A}^2(1-\Gamma^2)\int_{\tilde{a}_{\rm UV}}^{\infty}\frac{dr}{r^4}\;e^{-2\sqrt{1-\Gamma^2}r}\\
&\times\;\Big\{3+2r\left[3\sqrt{1-\Gamma^2}+r\left(3-2\Gamma^2+2\sqrt{1-\Gamma^2}r+r^2\right)\right]\Big\}\\
&= \pi k^2\lambda_L^5\mathcal{A}^2\frac{\sqrt{1-\Gamma^2}}{\tilde{a}_{\rm UV}^3}\;\exp\Big(-2\sqrt{1-\Gamma^2}\tilde{a}_{\rm UV}\Big)\\
&\times\;\Big\{\sqrt{1-\Gamma^2}+\tilde{a}_{\rm UV}\left[\tilde{a}_{\rm UV}^2+2\tilde{a}_{\rm UV}\sqrt{1-\Gamma^2}+2\left(1-\Gamma^2\right)\right]\Big\}\;,
\end{aligned}\tag{2.52}$$

or in terms of θ_Γ:

$$\begin{aligned}
\mathcal{E}_1 &= \pi k^2\lambda_L^5\mathcal{A}^2\frac{\cos\theta_\Gamma}{\tilde{a}_{\rm UV}^3}\;\exp\Big(-2\tilde{a}_{\rm UV}\cos\theta_\Gamma\Big)\\
&\times\;\Big\{\cos\theta_\Gamma+\tilde{a}_{\rm UV}\left[\tilde{a}_{\rm UV}^2+2\tilde{a}_{\rm UV}\cos\theta_\Gamma+2\cos^2\theta_\Gamma\right]\Big\}\;,
\end{aligned}\tag{2.53}$$

where $\tilde{a}_{\rm UV}\equiv a_{\rm UV}/\lambda_L$ is the (dimensionless) ultraviolet cutoff which regularizes the divergent energy integral in Eq. (2.52) at the core of the solution. In terms of the

parity-odd angle θ_Γ, the total energy (2.52) takes the following asymptotic form:

$$\mathcal{E}_1 \;=\; \pi k^2 \lambda_L^5 \mathcal{A}^2 \frac{\cos^2\theta_\Gamma}{\tilde{a}_{\rm UV}^3} + \dots\,, \tag{2.54}$$

where the subleading $O(\tilde{a}_{\rm UV}^{-2})$ terms are shown by the ellipsis. In the dimensionless units:

$$\mathcal{E}_1 = \frac{\pi k^2 \lambda_L^8}{a_{\rm UV}^3} \mathcal{A}^2 (1-\Gamma^2) + \dots\,. \tag{2.55}$$

Formally, this strong divergence disappears at the border of the stability domain given by $\Gamma = 1$ or $\theta_\Gamma = \pi/2$. We will comment on this property below.

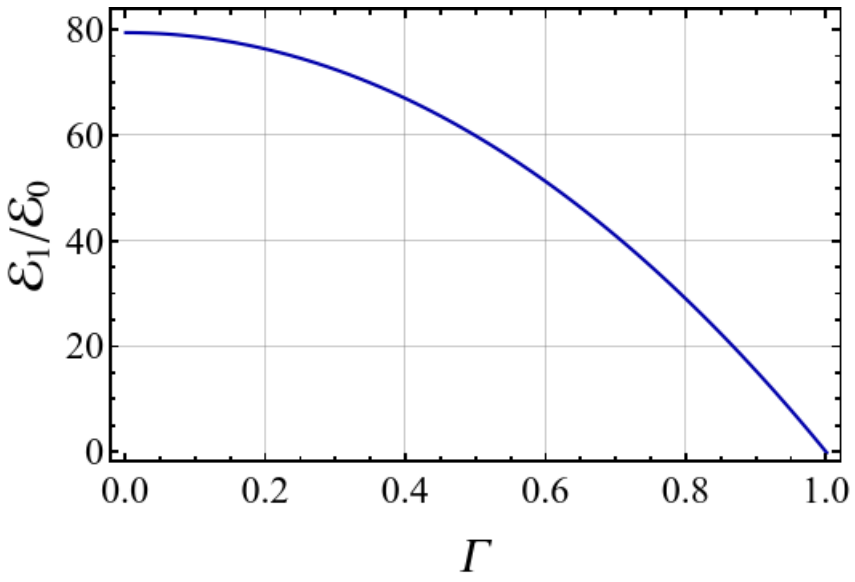

Figure 2.3: The dependence of the energy (2.52) of the $l = 1$ spheromak on the parity-odd parameter Γ for $a_{\rm UV} \equiv \xi = 0.1\lambda_L$. The energy is shown in the units of $\mathcal{E}_0 = 4\pi^2 k^2 \lambda_L^5 \mathcal{A}^2$.

The origin of the ultraviolet divergence can be traced down to the radial function of the current (2.50) and the magnetic field (2.51). For example, for the $(l, m) = (1, 0)$ spheromak, the $r \to 0$ asymptotic of the current density diverges as $j \sim 1/r^2$:

$$\boldsymbol{j}_{10}(\boldsymbol{r}) \;=\; \mathcal{A}\sqrt{\frac{3(1-\Gamma^2)}{4\pi}}\left(-\frac{\Gamma}{r}\cos\theta\,\hat{\boldsymbol{r}} + \frac{\Gamma}{2r}\sin\theta\,\hat{\boldsymbol{\theta}} - \frac{1}{2r^2}\sin\theta\,\hat{\boldsymbol{\phi}}\right) + O(r).$$

The magnetic field diverges even stronger at the core of the solution:

$$\boldsymbol{B}_{10}(\boldsymbol{r}) \;=\; 4\pi k\lambda_L \mathcal{A}\sqrt{\frac{3(1-\Gamma^2)}{4\pi}}\left(\frac{1}{r^3}\cos\theta\,\hat{\boldsymbol{r}} + \frac{1}{2r^3}\sin\theta\,\hat{\boldsymbol{\theta}} + \frac{\Gamma}{r^2}\sin\theta\,\hat{\boldsymbol{\phi}}\right) + O\left(\frac{1}{r}\right).$$

It is the divergence of the magnetic field, $B \sim 1/r^3$, which gives the largest contribution to the total energy of the solution. Similarly to the vortex solutions, the divergence of the spheromak's energy may be interpreted as a result of the inability

of London approximation to describe correctly the interior of the spheromak at the distances smaller than the coherence length ξ. A similar divergence – albeit in the much softer, logarithmic, form – appears also for the Abrikosov vortices in the London limit. In the case of Abrikosov vortices, the divergence disappears outside of the London limit being absorbed by the softening behavior of the magnitude of the superconducting condensate in the core of the vortex. We expect that the same property will take place for the spheromak solution.

To justify our claim, we notice that the superconducting density $|\psi|^2$ in the London approximation is a fixed constant. On the other hand, the magnetic-field strength of the spheromak solution raises towards the origin. These two properties are incompatible with each other taking into account the fact that the rise of magnetic field diminishes and, eventually, destroys the superconductivity. Therefore, one could suggest that outside of the London limit, the superconducting condensate should be suppressed in the core of the spheromak, thus leading to a gradual disappearance of the current $\boldsymbol{j}$ as we approach the spheromak's center. Although this solution seems quite plausible, we not insist on its validity as we do not address the spheromak solutions at finite values of the Ginzburg-Landau parameters κ.

According to (2.27), the magnetic field $\boldsymbol{B}$ depends locally on the current $\boldsymbol{j}$. As the current $\boldsymbol{j}$ diminishes in the core of the vortex, the behavior of the magnetic field softens towards the center of the spheromak leading to a non-singular behavior of the magnetic-field energy.

In the spheromak's core, the relevant length scale at which the condensate ψ deviates from its London value is set by the coherence length ξ. This quantity gives a natural ultraviolet cutoff of the spheromak solution: $a_{\rm UV} = \xi$, similarly to the properties of the solutions of the Abrikosov vortices in the London limit, where the size of the core is also set by the coherence length. The smallness of the ultraviolet cutoff $\xi \ll \lambda_L$ implies, automatically, that the superconductor should be of a strong type-2. The scale of the spatial features in the magnetic spheromak solution is governed by the penetration depth λ_L. The dependence of the energy of the simplest $l = 1$ spheromak configuration on the parity-odd parameter Γ for the ultraviolet cutoff $a_{\rm UV} \equiv \xi = 0.1\lambda_L$ is shown in Fig. 2.3.

In the case of a weak parity breaking, $\Gamma \ll 1$, the energy of the spheromak solution is proportional to the third power of the Ginzburg-Landau parameter (2.5): $\mathcal{E} \sim k^2\mathcal{A}^2\kappa^3\lambda_L^5$. Despite the fact that in a type-2 superconductors the parameter GL parameter is a large number, $\kappa \gg 1$, the amplitude $\mathcal{A}$ of the solution may be arbitrarily small (for example, $\mathcal{A} \simeq \kappa^{-3/2}$) thus putting the spheromak energy in an acceptable finite range of energies.

The spheromak's energy is mostly carried by the magnetic field. In Figure 2.4 we show the fraction of total energy of the $l = 1$ spheromak solution (2.52) with respect

to the magnetic-field energy carried by the same configuration:

$$\mathcal{E}_{B,1} = \frac{1}{8\pi}\int d^3\boldsymbol{r}\boldsymbol{B}_1^2\,. \tag{2.56}$$

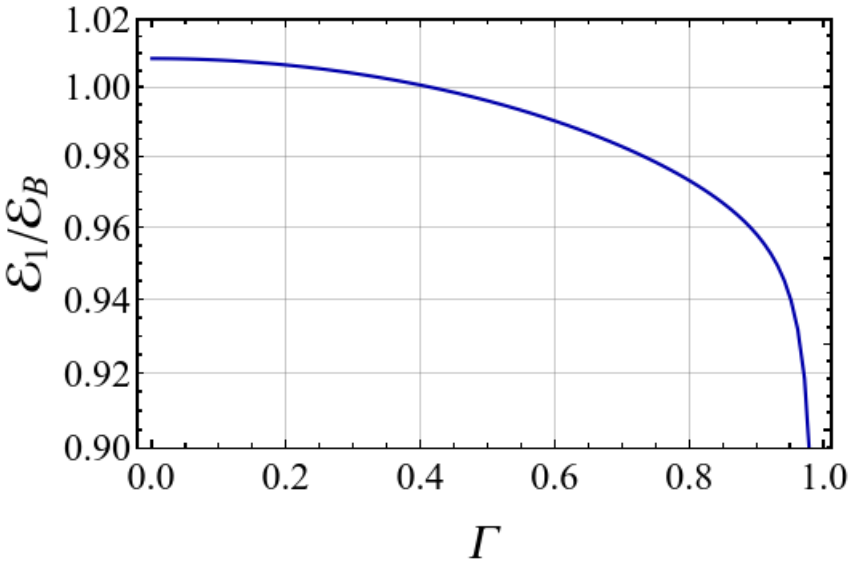

Figure 2.4: The dependence of the total energy of the $l = 1$ spheromak normalized to the energy of the magnetic field (2.56) for $a_{\rm UV} \equiv \xi = 0.1\lambda_L$.

At small values of the parity-odd parameter Γ, the ratio of the total energy $\mathcal{E}$ and the magnetic energy $\mathcal{E}_B$ is bigger than unity due to a negative (ferromagnetic-like) contribution of the parity-odd term to the total energy. As the parity breaking increases, the magnetic field contribution $\mathcal{E}_B$ becomes smaller while still taking the most essential part of the total energy. The ratio $\mathcal{E}/\mathcal{E}_B$ starts to decrease, with an increasing slope, when Γ approaches closely the maximal allowed value, $\Gamma \to 1$.

At the maximal value of the parity-odd violation, $\Gamma = 1$, the energy of the spheromak vanishes and the size of the spheromak (2.48) diverges. As we mentioned before, the large values of the inversion-breaking parameter Γ are not physically justifiable because, in terms of the series over the number of derivatives, the parity-odd term should be small compared to the leading terms in the Ginzburg-Landau free energy. Indeed, the Lifshitz invariant correspond to a higher-order marginal term in the derivative expansion which should be sufficiently small to ensure that expansion is convergent. Therefore, the limit $\Gamma \to 1$ cannot be treated consistently without taking into account even higher-order terms which are excluded from our analysis.

In details geometric structure of the magnetic field and the current density will be discussed in Section 2.3.3.

2.2.3 Explicit solution for parity-breaking $\Gamma = 1/\sqrt{2}$

It turns out that the radial functions $j_l^{\boldsymbol{z}}$ may be explicitly computed for arbitrary value of l in terms of special functions for a particular value of the parity-odd parameter

$\Gamma = 1/\sqrt{2}$ which corresponds to the parity-odd angle (2.49) $\theta_\Gamma = \pi/4$. In this case, the relations (2.37) and (2.38) remain unchanged, but a number of terms of Eq. (2.39) vanishes. This equation becomes simpler

$$\begin{aligned} 0 &= (j_l^{\boldsymbol{Y}})'''' + \frac{8}{r}(j_l^{\boldsymbol{Y}})''' + \frac{2}{r^2}\Big(6 - l(l+1)\Big)(j_l^{\boldsymbol{Y}})'' - \frac{4l(l+1)}{r^3}(j_l^{\boldsymbol{Y}})' \\ &- \frac{1}{r^2}\Big(\big(2 - l(l+1)\big)\frac{l(l+1)}{r^2} - r^2\Big) j_l^{\boldsymbol{Y}}, \end{aligned} \tag{2.57}$$

and it eventually can be solved explicitly for any angular number l:

$$j_l^{\boldsymbol{Y}} = \frac{1}{r^{3/2}}\Big(\mathcal{A}_1 \ker_{l+1/2}(r) + \mathcal{A}_2 \mathrm{kei}_{l+1/2}(r) + \mathcal{A}_3 \mathrm{ber}_{l+1/2}(r) + \mathcal{A}_4 \mathrm{bei}_{l+1/2}(r)\Big), \tag{2.58}$$

where $\mathcal{A}_i$ is a set of independent constants. General solution of this equation is a combination of Kelvin functions ($\ker_n(r), \mathrm{kei}_n(r), \mathrm{ber}_n(r)$ and $\mathrm{bei}_n(r)$) of the half integer order, which properties are disscused in Appendix B.

Since we are looking for compact solutions and the functions $\mathrm{ber}_{l+1/2}(r)$ and $\mathrm{bei}_{l+1/2}(r)$ diverge at infinity (B.3), we need to get rid of the coefficients $\mathcal{A}_3$ and $\mathcal{A}_4$. The minimum divergence of the solution at zero is achieved by the following relation between the remaining constants:

$$\mathcal{A}_1 = \mathcal{A}, \quad \mathcal{A}_2 = \mathcal{A}_1 \cot\left[\frac{3\pi}{4}\left(l + \frac{1}{2}\right)\right] = \mathcal{A}\eta_l\,. \tag{2.59}$$

As a result, the current components are presented as follows:

$$\begin{aligned} j_l^{\boldsymbol{Y}}(r) &= \frac{\mathcal{A}}{r^{3/2}}\Big(\ker_{l+\frac{1}{2}}(r) + \eta_l \mathrm{kei}_{l+\frac{1}{2}}(r)\Big), \\ j_l^{\boldsymbol{\Psi}}(r) &= \frac{\mathcal{A}}{l(l+1)}\left[\frac{l+1}{r^{3/2}}\Big(\ker_{l+\frac{1}{2}}(r) + \eta_l \mathrm{kei}_{l+\frac{1}{2}}(r)\Big)\right. \\ &\quad \left. + \frac{1}{\sqrt{2r}}\Big((1-\eta_l)\ker_{l+\frac{3}{2}}(r) + (1+\eta_l)\mathrm{kei}_{l+\frac{3}{2}}(r)\Big)\right], \\ j_l^{\boldsymbol{\Phi}}(r) &= \frac{\mathcal{A}}{l(l+1)\sqrt{2r}}\Big[(\eta_l - 1)\ker_{l+\frac{1}{2}}(r) - (1+\eta_l)\mathrm{kei}_{l+\frac{1}{2}}(r)\Big]. \end{aligned} \tag{2.60}$$

The radial functions of the magnetic field corresponding to solution (2.60) have the following form:

$$\begin{aligned} B_l^{\boldsymbol{Y}}(r) &= -\frac{4\pi k \lambda_L \mathcal{A}}{\sqrt{2} r^{3/2}}\Big[(1-\eta_l)\ker_{l+\frac{1}{2}}(r) + (1+\eta_l)\mathrm{kei}_{l+\frac{1}{2}}(r)\Big], \\ B_l^{\boldsymbol{\Psi}}(r) &= -\frac{4\pi k \lambda_L \mathcal{A}}{l(l+1)}\left[-\frac{1}{\sqrt{r}}\Big[\eta_l \ker_{l+\frac{3}{2}}(r) - \mathrm{kei}_{l+\frac{3}{2}}(r)\Big]\right. \\ &\quad \left. + \frac{(l+1)}{\sqrt{2} r^{3/2}}\Big((1-\eta_l)\ker_{l+\frac{1}{2}}(r) + (1+\eta_l)\mathrm{kei}_{l+\frac{1}{2}}(r)\Big)\right], \\ B_l^{\boldsymbol{\Phi}}(r) &= -\frac{4\pi k \lambda_L \mathcal{A}}{l(l+1)\sqrt{r}}\Big[\eta_l \ker_{l+\frac{1}{2}}(r) - \mathrm{kei}_{l+\frac{1}{2}}(r)\Big]. \end{aligned} \tag{2.61}$$

Spatial visualization of magnetic field lines is shown in Fig. 2.5. One can see how the symmetry pattern becomes more complicated with an increase of the values in the orbital number l.

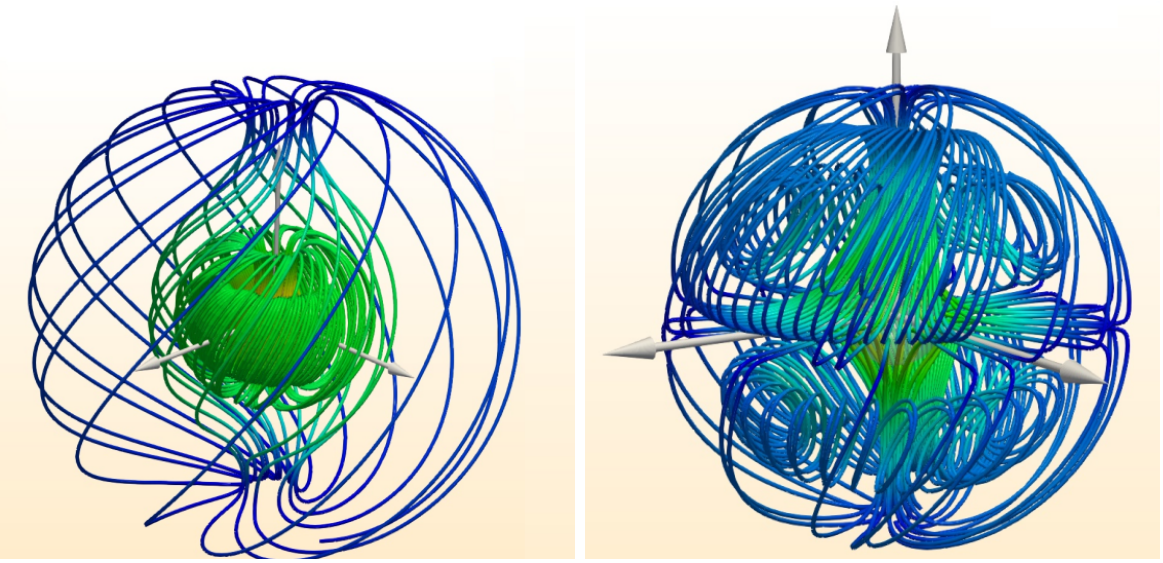

(a) $l = 1, m = 0$. (b) $l = 2, m = 0$.

Figure 2.5: Three-dimensional distributions of magnetic field lines in a bulk of noncentrosymmtric superconductor for two set of values l and m in the case of $\Gamma = 1/\sqrt{2}$.

The leading behavior of the radial functions of currents and magnetic fields at the origin $r \to 0$ is proportional to the negative powers of r (at $l = 2$ one has a curious exception: $j_l^{\mathbf{\Psi}} \sim r$):

$$j_l^{\boldsymbol{Y}}, j_l^{\mathbf{\Psi}} \sim \frac{1}{r^l}, \quad B_l^{\boldsymbol{Y}}, B_l^{\mathbf{\Psi}} \sim \frac{1}{r^{l+2}}, \quad j_l^{\mathbf{\Phi}}, B_l^{\mathbf{\Phi}} \sim \frac{1}{r^{l+1}}. \tag{2.62}$$

Consequently, the spheromak energy diverges in the ultraviolet region:

$$\mathcal{E}_{lm}^{\text{div}} \sim \frac{C_{lm}}{\lambda_L} \left(\frac{\lambda_L}{\xi}\right)^{2l+1}, \tag{2.63}$$

where C_{lm} is a constant and we took the coherence length as the ultraviolet cutoff, $a_{\text{UV}} = \xi$. Since we are working in a type-2 superconductor with $\xi \ll \lambda_L$, the spheromaks with the large orbital momenta l are energetically unfavorable as their mass rises exponentially (2.63) with increase of l.

In order to find an exact expression for the spheromak energy, it is convenient to use the vector notations for the basis of the vector spherical harmonics and for the radial functions, respectively:

$$\vec{\boldsymbol{Z}}_{lm} = \Big(\boldsymbol{Y}_{lm},\ \mathbf{\Psi}_{lm},\ \mathbf{\Phi}_{lm}\Big)^T, \qquad \vec{j}_l = \Big(j_l^{\boldsymbol{Y}},\ j_l^{\mathbf{\Psi}},\ j_l^{\mathbf{\Phi}}\Big)^T. \tag{2.64}$$

We expand $\boldsymbol{j}$ and $\boldsymbol{\nabla}_{\boldsymbol{r}} \times \boldsymbol{j}$ over the vector harmonics:

$$\boldsymbol{j}_{lm} = \vec{j}_l \vec{\boldsymbol{Z}}_{lm} \quad \text{and} \quad \boldsymbol{\nabla}_{\boldsymbol{r}} \times \boldsymbol{j}_{lm} = \boldsymbol{h}_{lm} = \vec{h}_l \vec{\boldsymbol{Z}}_{lm}, \tag{2.65}$$

where

$$\vec{h}_l = -\Big(\frac{l(l+1)}{r} j_l^{\mathbf{\Phi}},\ \mathcal{D} j_l^{\mathbf{\Phi}},\ \frac{1}{r} j_l^{\boldsymbol{Y}} - \mathcal{D} j_l^{\mathbf{\Psi}}\Big)^T, \tag{2.66}$$

is a vector in the space of the vector spherical harmonics.

Due to the orthogonality of the vector spherical harmonics (A.5), the scalar products in the energy functional can be simplified. For example, we obtain for the mixed term the following expression:

$$\boldsymbol{j}_{lm}\cdot(\boldsymbol{\nabla}_{\boldsymbol{r}}\times\boldsymbol{j}_{lm})^{*}=\boldsymbol{j}_{lm}\cdot(\boldsymbol{h}_{lm})^{*}=\left(\vec{j}_l\vec{\boldsymbol{Z}}_{lm}\right)\cdot\left(\vec{h}_l\vec{\boldsymbol{Z}}_{lm}\right)^{*}=\sum_{i=1}^{3}j_l^ih_l^i\big|(\boldsymbol{Z}_i)_{lm}\big|^2, \tag{2.67}$$

where the second vector of the dot product is taken to be the complex conjugate to take into account that the electric current and magnetic field are physical real-valued quantities. One then gets the following expression for the total energy of the solution:

$$\begin{aligned}\mathcal{E} &= 2\pi k^2\lambda_L^5\int d^3\boldsymbol{r}\left[\big|\boldsymbol{\nabla}_{\boldsymbol{r}}\times\boldsymbol{j}\big|^2+\big|\boldsymbol{j}\big|^2-2\Gamma\boldsymbol{j}\cdot(\boldsymbol{\nabla}_{\boldsymbol{r}}\times\boldsymbol{j})^{*}\right]\\ &= 2\pi k^2\lambda_L^5\sum_{i=1}^{3}q_{lm}^iF_l^i,\end{aligned} \tag{2.68}$$

where, by using normalization property of vector spherical harmonics (A.6), we obtain

$$q_{lm}^i=\int d\Omega\big|(\boldsymbol{Z}_i)_{lm}\big|^2,\qquad \vec{q}_{lm}=\begin{pmatrix}1\\ l(l+1)\\ l(l+1)\end{pmatrix}, \tag{2.69}$$

and

$$F_l^i=\int_{\tilde{a}_{\mathrm{UV}}}^{\infty}dr\,r^2\left[(h_l^i)^2+(j_l^i)^2-2\Gamma j_l^ih_l^i\right], \tag{2.70}$$

where $\tilde{a}_{\mathrm{UV}}=a_{\mathrm{UV}}/\lambda_L=\xi/\lambda_L$ - is the ultraviolet cutoff.

We get for the energy of the (l,m)–spheromak solution:

$$\mathcal{E}_{lm}=\pi k^2\lambda_L^5(1+\eta_l^2)\mathcal{A}^2f_l\left(\frac{\xi}{\lambda_L}\right), \tag{2.71}$$

where η_l is given in Eq. (2.59), and

$$\begin{aligned}f_l(r_0) &= \int_{r_0}^{\infty}dr\left[\frac{2l+1}{lr}\Big(\mathrm{ker}^2_{l+\frac{1}{2}}(r)+\mathrm{kei}^2_{l+\frac{1}{2}}(r)\Big)\right.\\ &+\frac{\sqrt{2}}{l}\Big(\mathrm{ker}_{l+\frac{1}{2}}(r)\,\mathrm{ker}_{l+\frac{3}{2}}(r)+\mathrm{kei}_{l+\frac{1}{2}}(r)\mathrm{kei}_{l+\frac{3}{2}}(r)\\ &+\mathrm{ker}_{l+\frac{1}{2}}(r)\mathrm{kei}_{l+\frac{3}{2}}(r)-\mathrm{ker}_{l+\frac{3}{2}}(r)\mathrm{kei}_{l+\frac{1}{2}}(r)\Big)\\ &\left.+\frac{r}{l(l+1)}\Big(\mathrm{ker}^2_{l+\frac{1}{2}}(r)+\mathrm{kei}^2_{l+\frac{1}{2}}(r)+\mathrm{ker}^2_{l+\frac{3}{2}}(r)+\mathrm{kei}^2_{l+\frac{3}{2}}(r)\Big)\right].\end{aligned} \tag{2.72}$$

The density of a given function $f_l(r)$ (otherwise, the normalized linear energy density $\frac{d\mathcal{E}_{lm}}{dr}/\mathcal{E}_0$, where $\mathcal{E}_0=\pi k^2\lambda_L^5(1+\eta_l^2)\mathcal{A}^2$) is presented in the logarithmic scale in Fig. 2.6.

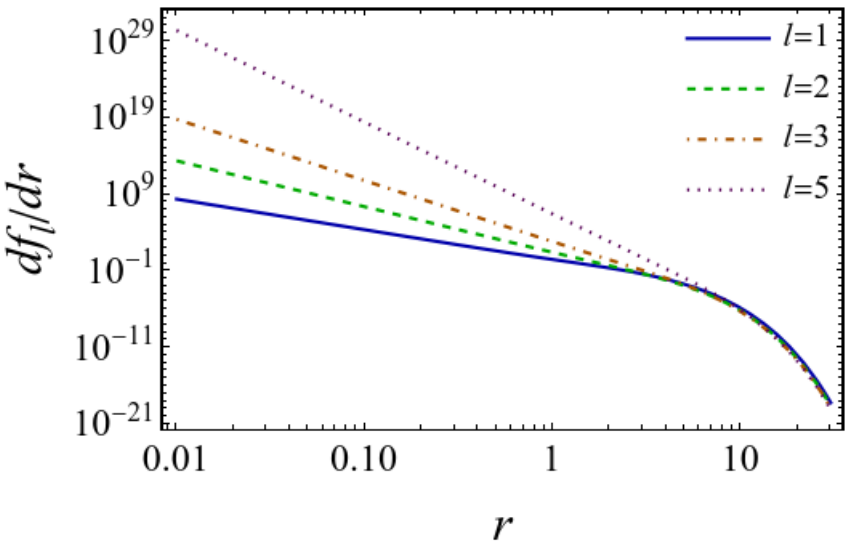

Figure 2.6: Dependence of the derivative of the function ($f_l(r)$) on r for several values of the orbital number l.

For certain values of the orbital number l, the total energy can be calculated analytically using relations for the Kelvin functions given in Appendix B. For example:

$$\begin{aligned} f_1(r_0) &= \frac{\pi e^{-\sqrt{2}r_0}}{4r_0^3}\left(\sqrt{2}r_0^3 + 2r_0^2 + \sqrt{2}r_0 + 1\right), \\ f_2(r_0) &= \frac{3\pi e^{-\sqrt{2}r_0}}{2r_0^5}\left(\frac{r_0^5}{9\sqrt{2}} + \frac{r_0^4}{3} + \frac{r_0^3}{\sqrt{2}} + \frac{7r_0^2}{6} + \sqrt{2}r_0 + 1\right). \end{aligned} \tag{2.73}$$

2.2.4 Helicity of spheromak solutions

Magnetic helicity is a topological quantity that determines how magnetic lines are connected, twisted, bent and tied [30, 93]. Or, in other words, it can indeed serve as a measure the entanglement of the magnetic field lines in knotted configurations of the magnetic field [31]. Magnetic helicity is also a kind of topological invariant, since it is a non-local quantity that determines the configuration as a whole, and not its individual parts (helicity is a non-additive quantity).

The magnetic helicity is widely used in ordinary electrically conducting plasmas described by ideal magnetohydrodynamics, where it is a conserved quantity modulo reconnections of the magnetic field lines [45].

The helicity of the magnetic field is determined by the following formula:

$$\mathcal{H} = \int d^3\boldsymbol{x}\ \boldsymbol{A}\cdot\boldsymbol{B}\,. \tag{2.74}$$

This formula may be suitably adapted to characterize the spheromak solutions in the parity-odd superconductors. To this end, we may use the relationship (2.2) between gauge-invariant current $\boldsymbol{j}$ and vector potential $\boldsymbol{A}$ ($\boldsymbol{j} = 2e\psi_0^2\,(\boldsymbol{\nabla}\varphi - e\boldsymbol{A})$). In the absence of Abrikosov vortices, we can choose a suitable gauge to eliminate phase and

express vector potential through current: $\boldsymbol{A} = -4\pi k\lambda_L^2 \boldsymbol{j}$. Using this relationship and the second London equation (2.16), we obtain the following expression for the helicity (2.74):

$$\begin{aligned} \mathcal{H}_{lm} &= 16\pi^2 k^2 \lambda_L^6 \int d^3\boldsymbol{r} \big(\boldsymbol{j}_{lm} \cdot (\boldsymbol{\nabla}_{\boldsymbol{r}} \times \boldsymbol{j}_{lm})\big) \\ &= 16\pi^2 k^2 \lambda_L^6 \mathcal{A}^2 \chi_l \left(\frac{\xi}{\lambda_L}\right), \end{aligned} \tag{2.75}$$

where the function

$$\chi_l(r_0) = \frac{\mathcal{H}_{lm}}{(4\pi k \mathcal{A} \lambda_L^3)^2} = \frac{1}{\mathcal{A}^2} \sum_{i=1}^{3} q_{lm}^i \int_{r_0}^{\infty} dr\, r^2 j_l^i(r) h_l^i(r)\,, \tag{2.76}$$

plays a role of a dimensionless helicity. The factor q_{lm}^i is given in Eq. (2.69), the definiton of $h_l^i(r)$ is presented in (2.66) and the ratio $r_0 = \xi/\lambda_L$ serves as a dimensionless cutoff.

In Fig. 2.7, we show the dependence of the normalized helicity (2.76) of the $(l, m) = (1, 0)$ spheromak on the parity-odd coupling Γ for various values of the core size ξ of the solution. The helicity of the spheromak solution becomes zero when the parity-odd coupling Γ vanishes.

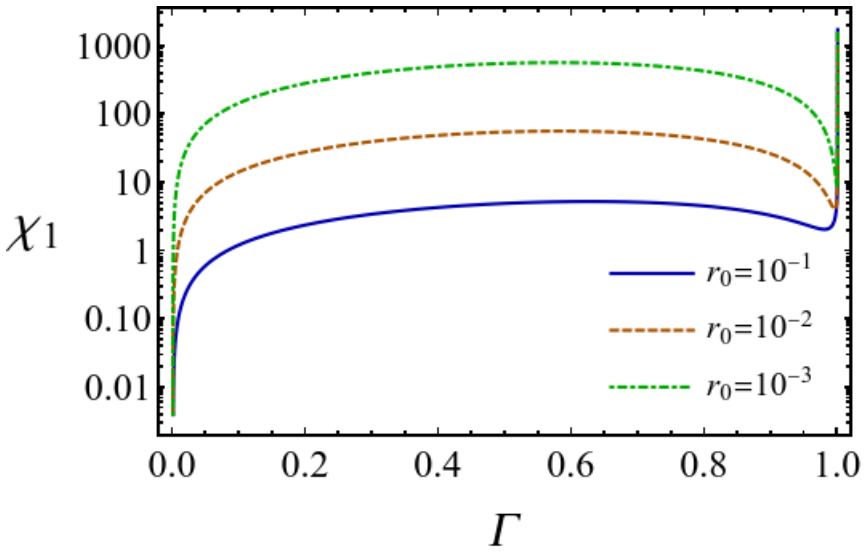

Figure 2.7: The helicity (2.76) of the $l = 1$ spheromak as a function of the parity-breaking parameter Γ for different sizes of the (dimensionless) spheromak core $r_0 = \xi/\lambda_L$.

Figure 2.8 shows the dependence of the helicity of the $(l, m) = (1, 0)$-spheromak solution,

$$H_l = \frac{\mathcal{H}_{lm}}{\lambda_L \mathcal{E}_{B,lm}}, \tag{2.77}$$

normalized to the energy of its magnetic field,

$$\mathcal{E}_{B,lm} = \frac{1}{8\pi} \int d^3\boldsymbol{r} \boldsymbol{B}_{lm}^2 = 2\pi k^2 \lambda_L^5 \int_{r_0}^{\infty} dr\, r^2 q_{ml}^i (h_l^i)^2\,. \tag{2.78}$$

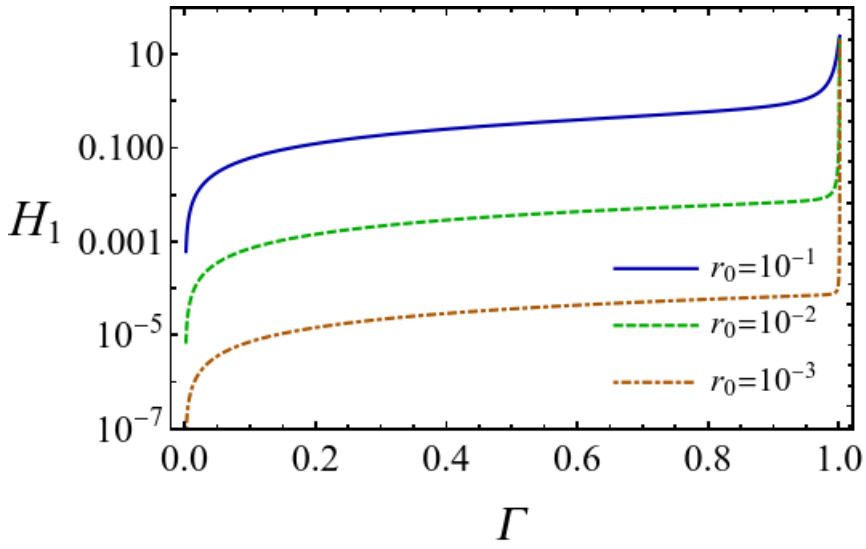

Figure 2.8: The helicity (2.76) normalized to the energy of magnetic field (2.77) as a function of the parity-breaking parameter Γ for different sizes of the (dimensionless) spheromak core $r_0 = \xi/\lambda_L$.

One can ealily check that the normalized helicity (2.77) depends only on the orbital number l of the spheromak and independent of its projection m.

As we see, the stability of our solution is supported by the fact that the lines of the magnetic lines self-intertwine with themselves and form a knotted-field configuration. Parity-broken system allows for a magnetoelectric effect which generates a supercurrent along the magnetic field lines. The conserved supercurrent, flowing along the lines of the magnetic field of our solution, produces its own magnetic field which, in turn, appears to coincide with the original magnetic field that generates the current. In other words, the solution is self-supporting: the magnetic field hosts the supercurrent which maintains the magnetic field. Since the electric current is superconducting, the current flow is dissipationless and this self-supporting solution has an infinite lifetime.

2.3 Finite-energy solution

In the previous section, we noticed that the total energy of the spheromak solution diverges in the London limit due to the contribution which emerge at the core of the solution. We speculated that this divergence can be eliminated by relaxing the London limit and solving the full equations of motion which may provide a noticeable dependence of the order parameter on coordinates at the spheromak core. Similarly, the energy of the ordinary Abrikosov vortex solution, which diverges in the London limit $\beta \to \infty$, becomes a finite quantity at finite values of the GL parameter κ due to the space-dependence of the order parameter around the vortex core. As this task cannot be addressed analytically, in this section we explore another physically meaningful

possibility to obtain a non-divergent, finite-energy solution in the London limit. We consider a parity-odd superconductor with a spherical cavity inside. We show that if the radius of the cavity is chosen in coherence with the intrinsic parameters of the superconductor, then the cavity can serve as a pinning center of the finite-energy superconducting spheromak solution.

2.3.1 Solution in superconducting exterior

Consider the Ampère-Maxwell equation (2.3b) in the London limit:

$$\boldsymbol{\nabla}\times\Big(\frac{\boldsymbol{B}}{4\pi}+\gamma\boldsymbol{j}\Big) \;=\; k\boldsymbol{j}+2\gamma e^2|\psi_0|^2\boldsymbol{B}\,. \tag{2.79}$$

Using the dimensionless units with the rescaled spatial coordinates, the appropriately rescaled derivatives (2.21) and the dimensionless parity breaking coupling (2.24), ($\boldsymbol{r}=\boldsymbol{x}/\lambda_L,\ \boldsymbol{\nabla}_{\boldsymbol{r}}=\lambda_L\boldsymbol{\nabla},\ \Gamma=\frac{\gamma}{k\lambda_L}$) we represent this equation in the following form:

$$\frac{1}{\lambda_L}\boldsymbol{\nabla}_{\boldsymbol{r}}\times\Big(\frac{\boldsymbol{B}}{4\pi}+k\Gamma\lambda_L\boldsymbol{j}\Big)=k\boldsymbol{j}+\frac{\Gamma}{4\pi\lambda_L}\boldsymbol{B}\,, \tag{2.80}$$

or

$$\boldsymbol{J}=\frac{1}{4\pi\lambda_L}\boldsymbol{\nabla}_{\boldsymbol{r}}\times\Big(\boldsymbol{B}-4\pi\boldsymbol{M}\Big)=\frac{1}{4\pi\lambda_L}\boldsymbol{\nabla}_{\boldsymbol{r}}\times\boldsymbol{H}, \tag{2.81}$$

where the magnetization $\boldsymbol{M}$ and the total current $\boldsymbol{J}$ are, respectively, as follows:

$$\begin{aligned}\boldsymbol{M} &= -\Gamma k\lambda_L\boldsymbol{j}\,,\\ \boldsymbol{J} &= k\boldsymbol{j}+\frac{\Gamma}{4\pi\lambda_L}\boldsymbol{B}\,.\end{aligned} \tag{2.82}$$

Using the results of the previous section for the $l=1$ solution ((2.50) and (2.51)), we provide the expressions for the radial components of the total current $\boldsymbol{J}$:

$$\begin{aligned}J^{\boldsymbol{Y}}(r) &= -k\frac{\mathcal{A}}{r^2}e^{-r\cos\theta_\Gamma}\cos\theta_\Gamma\left[\frac{1}{r}\sin(r\sin\theta_\Gamma-\theta_\Gamma)+\sin\big(r\sin\theta_\Gamma-2\theta_\Gamma\big)\right],\\ J^{\boldsymbol{\Psi}}(r) &= k\frac{\mathcal{A}}{2r^2}e^{-r\cos\theta_\Gamma}\cos\theta_\Gamma\left[\frac{1}{r}\sin(r\sin\theta_\Gamma-\theta_\Gamma)\right.\\ &\qquad\left.+\sin(r\sin\theta_\Gamma-2\theta_\Gamma)+r\sin\left(r\sin\theta_\Gamma-3\theta_\Gamma\right)\right],\\ J^{\boldsymbol{\Phi}}(r) &= k\frac{\mathcal{A}}{2r^2}e^{-r\cos\theta_\Gamma}\cos\theta_\Gamma\left[\cos(r\sin\theta_\Gamma-2\theta_\Gamma)+r\cos(r\sin\theta_\Gamma-3\theta_\Gamma)\right],\end{aligned} \tag{2.83}$$

and the magnetic field $\boldsymbol{H}$:

$$\begin{aligned}H^{\boldsymbol{Y}}(r) &= 4\pi k\lambda_L\frac{\mathcal{A}}{r^2}e^{-r\cos\theta_\Gamma}\cos\theta_\Gamma\left[\cos(r\sin\theta_\Gamma-\theta_\Gamma)+\frac{1}{r}\cos(r\sin\theta_\Gamma)\right],\\ H^{\boldsymbol{\Psi}}(r) &= -2\pi k\lambda_L\frac{\mathcal{A}}{r^2}e^{-r\cos\theta_\Gamma}\cos\theta_\Gamma\left[r\cos(r\sin\theta_\Gamma-2\theta_\Gamma)\right.\\ &\qquad\left.+\cos(r\sin\theta_\Gamma-\theta_\Gamma)+\frac{1}{r}\cos(r\sin\theta_\Gamma)\right],\\ H^{\boldsymbol{\Phi}}(r) &= 2\pi k\lambda_L\frac{\mathcal{A}}{r^2}e^{-r\cos\theta_\Gamma}\cos\theta_\Gamma\left[r\sin(r\sin\theta_\Gamma-2\theta_\Gamma)+\sin(r\sin\theta_\Gamma-\theta_\Gamma)\right].\end{aligned} \tag{2.84}$$

To make our notations concise, we drop the superscript $l = 1$ from the radial functions hereafter.

It should be noted that particular components of the current $J^{\boldsymbol{Y}}(r)$ and the magnetic field $H^{\boldsymbol{\Phi}}(r)$ are related:

$$-2\pi\lambda_L r J^{\boldsymbol{Y}}(r) = H^{\boldsymbol{\Phi}}(r)\,, \tag{2.85}$$

and thus they share the same set of zeros except for the point in the origin, $r = 0$.

Consider now a spherical non-conducting cavity of the radius R in the bulk of the superconductor. For simplicity, we assume that the cavity is empty so that it possesses electromagnetic properties of the vacuum (the permittivity and permeability of the cavity are fixed to the corresponding vacuum values). Since no physical current $\boldsymbol{J}$ can pass through the interface surface between the superconductor and the cavity, the normal component of the current is vanishing at the interface:

$$\hat{\boldsymbol{r}} \cdot \boldsymbol{J}(\boldsymbol{r})\Big|_{r=R_0} = 0\,, \tag{2.86}$$

where we used the dimensionless units, $R_0 = R/\lambda_R$.

Our next consideration is based on the observation, which we will see shortly after, that in terms of the electric supercurrents the superconducting spheromak solution is composed of the spherical, onion-like arranged shells which separate the regions of space with vanishing normal currents at the interfaces between the shells. This structure of the spheromak solution is remarkably consistent with the boundary condition (2.86): the radius of the spherical cavity can be chosen in such a way that the radius R coincides with a radius an interface between two adjacent shells of the spheromak solution. This construction will remove the divergent part of the spheromak's core region without modifying the original spheromak solution outside the core. Notice that the onion-like structure of the spheromak implies that the supercurrent, circulating inside each shell, does not enter the adjacent shells. However, the magnetic field penetrates between the shells as its normal component does not vanish at the inter-shell interface. In particular, the magnetic field enters the internal cavity from the superconducting exterior, as we discuss below.

Using the explicit expression for the radial component of the total supercurrent (2.83), we find that the distance R_0 at which the radial component vanishes (2.86) satisfies the following equation which explicitly depends on the parity-odd angle θ_Γ:

$$0 = \sin(R_0 \sin\theta_\Gamma - \theta_\Gamma) + R_0 \sin\big(R_0 \sin\theta_\Gamma - 2\theta_\Gamma\big)\,, \tag{2.87}$$

or, in terms of Γ:

$$\begin{aligned} 0 \;&=\; \sqrt{1-\Gamma^2}\sin(\Gamma R_0) - \Gamma\cos(\Gamma R_0) \\ &+\; R_0\Big(\big(1-2\Gamma^2\big)\sin(\Gamma R_0) - 2\Gamma\sqrt{1-\Gamma^2}\cos(\Gamma R_0)\Big). \end{aligned} \tag{2.88}$$

The function (2.87) is shown in Fig. 2.9 for a few values of the parity-odd parameter Γ. While the locations of zeros, shown by the dots in the same figure, cannot be found analytically they can easily be determined numerically. The multi-shell structure of the superconducting spheromak solution is clearly seen in the figure since each Γ parameter corresponds to multiple "inter-shell" radii at which the radial component of the current vanishes. Figure 2.10 shows the dependence of the first inter-shell radius R_0, given by

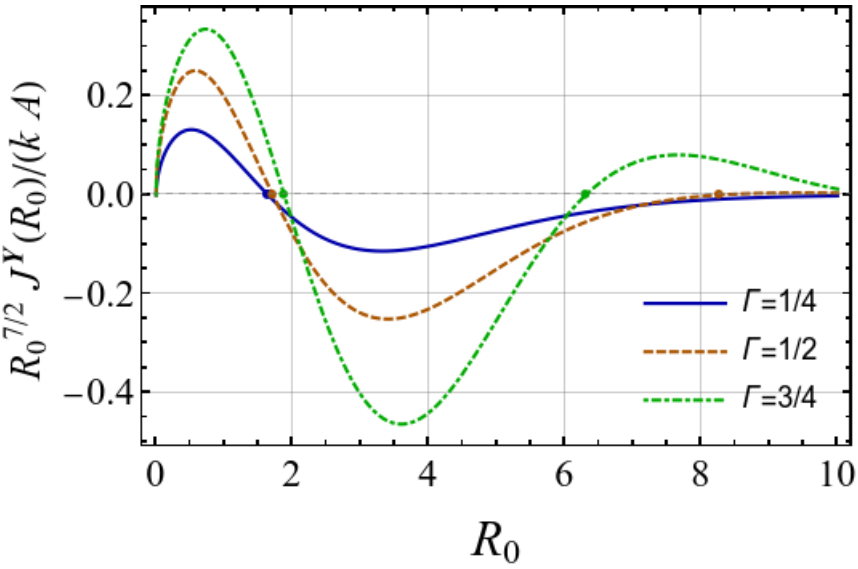

Figure 2.9: Location of the first few zeros of the $J^{\mathbf{Y}}(r)$ (2.83) for three different values of Γ.

the smallest non-vanishing solution of Eq. (2.87), on the parity-odd parameter Γ. It should be noted that the radius R_0 has a finite value when $\Gamma = 1$. Moreover, for completeness of the picture, in Fig. 2.11 we show the dependence of the second and third inter-shell radii of the cavity on the parameter Γ.

In addition to the numerical solution, we can get the analytical dependence of R_0 on Γ in the case of small values of Γ, which corresponds to physically realizable values in real parity-odd materials. To this end, we expand the transcendental equation (2.87) at small θ_Γ:

$$0 = (R_0^2 - R_0 - 1)\theta_\Gamma + \mathcal{O}(\theta_\Gamma^3)\,, \tag{2.89}$$

and find that the leading-order term vanishes at the radius of the cavity R_0 that turns out to be equal to the golden number $\mathcal{R}$:

$$R_0 = \frac{R}{\lambda_L} = \mathcal{R}, \qquad \mathcal{R} = \frac{1+\sqrt{5}}{2} \approx 1.618. \tag{2.90}$$

In other words, the minimal radius of the cavity that can serve as a pinning centre of the superconducting spheromak in the London limit is equaled to the London penetration length multiplied by the golden ratio $\mathcal{R}$. At small values of the parity-odd

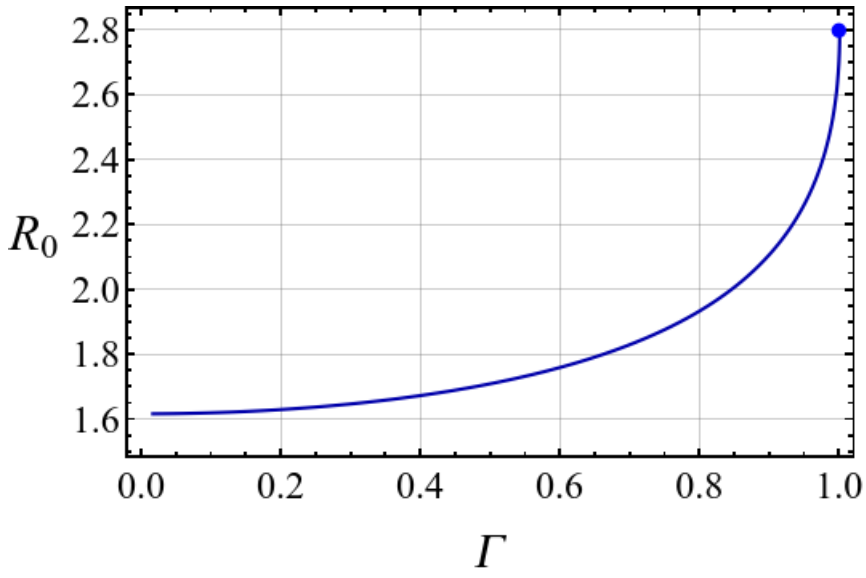

Figure 2.10: Dependence of the first inter-shell radius R_0 of the superconducting spheromak solution on the parity-odd strentgh Γ. The dot marks the end-point of the curve at border of the stability zone, $\Gamma = 1$.

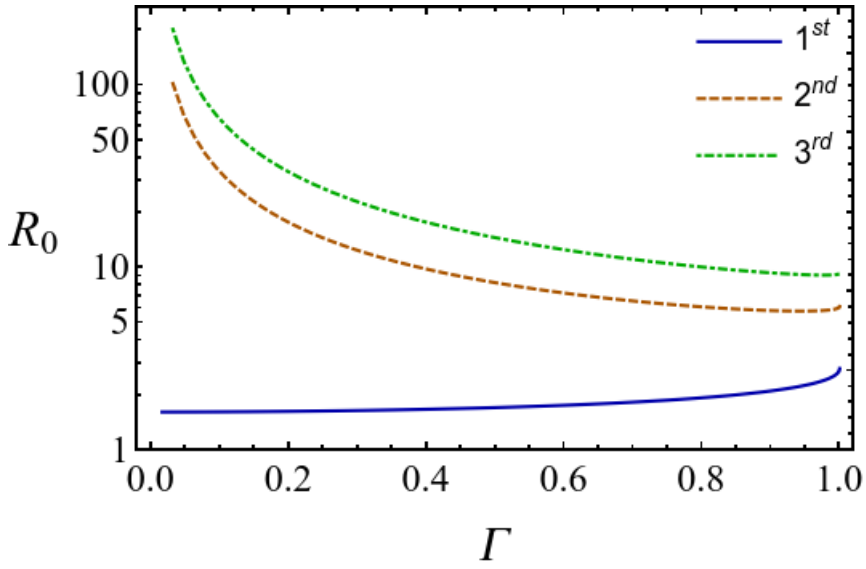

Figure 2.11: Dependence of the inter-shell radii R_0 of the first three cavities on the parity-odd strentgh Γ.

angle θ_Γ, the minimal cavity radius $R_0 = R/\lambda_L$ receives a quadratic correction in θ_Γ:

$$R_0 = \mathcal{R} + \frac{11\sqrt{5}-5}{60}\theta_\Gamma^2 + \dots, \tag{2.91}$$

where higher-order corrections, $O(\theta_\Gamma^4)$, are not shown. In physical units, this equation for the cavity radius can be transfrom into the form:

$$R = \mathcal{R}\lambda_L + \frac{11\sqrt{5}-5}{60}\frac{\gamma^2}{k^2\lambda_L} + \dots, \tag{2.92}$$

where we used the facts that the angle θ_Γ is related, via Eq. (2.49), to the dimensionless parity-odd breaking parameter Γ which, in turn, can be expressed, in Eq. (2.24), via

the magnitudes of the kinetic term k and the parity-broken term γ of the free GL energy (2.1).

Arbitrary size of the cavity

The cavity radius R_0 is determined by the condition that the normal component of the electric current vanishes (2.86) at the cavity boundary. So far we discussed the simplest spheromak solution (2.83) which provides us with the constraint (2.87) that gives us a discrete set of allowed values of R_0. Obviously, in the realistic case, the radius of a physical cavity may take arbitrary values implying incompatibility of the cavity radius with the spheromak configuration (2.83). This configuration can indeed be easily generalized. For this, we take equation (2.44):

$$\begin{aligned} j_1^{\boldsymbol{Y}}(r) = & - (c_1+c_2)\frac{e^{-\sqrt{1-\Gamma^2}r}}{r^3}\Big[(r+\sqrt{1-\Gamma^2})\cos(\Gamma r) - \Gamma\sin(\Gamma r)\Big] \\ & - i(c_1-c_2)\frac{e^{-\sqrt{1-\Gamma^2}r}}{r^3}\Big[(r+\sqrt{1-\Gamma^2})\sin(\Gamma r) + \Gamma\cos(\Gamma r)\Big], \end{aligned} \tag{2.93}$$

and put $c_1+c_2=-\tilde{\mathcal{A}}_1$ and $i(c_1+c_2)=-\tilde{\mathcal{A}}_2$, so as to leave two arbitrary independent amplitudes $\tilde{\mathcal{A}}_1$ and $\tilde{\mathcal{A}}_2$. Below we provide an explicit form for all currents and magnetic fields of the $l=1$ spheromak solution in terms of $\Gamma=\sin\theta_\Gamma$.

The superconducting component of the electric current is:

$$\begin{aligned} j_1^{\boldsymbol{Y}}(r) &= \frac{\mathcal{A}_1}{r^2}e^{-r\cos\theta_\Gamma}\left[\frac{1}{r}\cos(r\sin\theta_\Gamma+\theta_\Gamma)+\cos\big(r\sin\theta_\Gamma\big)\right] \\ &\quad +\frac{\mathcal{A}_2}{r^2}e^{-r\cos\theta_\Gamma}\left[\frac{1}{r}\sin(r\sin\theta_\Gamma+\theta_\Gamma)+\sin\big(r\sin\theta_\Gamma\big)\right], \qquad (2.94) \\ j_1^{\boldsymbol{\Psi}}(r) &= -\frac{\mathcal{A}_1}{2r^2}e^{-r\cos\theta_\Gamma}\left[\frac{1}{r}\cos(r\sin\theta_\Gamma+\theta_\Gamma)+\cos\big(r\sin\theta_\Gamma\big)+r\cos(r\sin\theta_\Gamma-\theta_\Gamma)\right] \\ &\quad -\frac{\mathcal{A}_2}{2r^2}e^{-r\cos\theta_\Gamma}\left[\frac{1}{r}\sin(r\sin\theta_\Gamma+\theta_\Gamma)+\sin\big(r\sin\theta_\Gamma\big)+r\sin(r\sin\theta_\Gamma-\theta_\Gamma)\right], \\ j_1^{\boldsymbol{\Phi}}(r) &= \frac{\mathcal{A}_1}{2r^2}e^{-r\cos\theta_\Gamma}\left[\sin\big(r\sin\theta_\Gamma\big)+r\sin(r\sin\theta_\Gamma-\theta_\Gamma)\right] \\ &\quad -\frac{\mathcal{A}_2}{2r^2}e^{-r\cos\theta_\Gamma}\left[\cos\big(r\sin\theta_\Gamma\big)+r\cos(r\sin\theta_\Gamma-\theta_\Gamma)\right], \end{aligned}$$

while the total electric current acquires the following form:

$$
\begin{aligned}
J^{\boldsymbol{Y}}(r) &= k\frac{\mathcal{A}_1}{r^2}e^{-r\cos\theta_\Gamma}\cos\theta_\Gamma\left[\frac{1}{r}\cos(r\sin\theta_\Gamma)+\cos(r\sin\theta_\Gamma-\theta_\Gamma)\right] \\
&\quad +k\frac{\mathcal{A}_2}{r^2}e^{-r\cos\theta_\Gamma}\cos\theta_\Gamma\left[\frac{1}{r}\sin(r\sin\theta_\Gamma)+\sin(r\sin\theta_\Gamma-\theta_\Gamma)\right], \qquad (2.95)\\
J^{\boldsymbol{\Psi}}(r) &= -k\frac{\mathcal{A}_1}{2r^2}e^{-r\cos\theta_\Gamma}\cos\theta_\Gamma\left[\frac{1}{r}\cos(r\sin\theta_\Gamma)+\cos(r\sin\theta_\Gamma-\theta_\Gamma)+r\cos(r\sin\theta_\Gamma-2\theta_\Gamma)\right] \\
&\quad -k\frac{\mathcal{A}_2}{2r^2}e^{-r\cos\theta_\Gamma}\cos\theta_\Gamma\left[\frac{1}{r}\sin(r\sin\theta_\Gamma)+\sin(r\sin\theta_\Gamma-\theta_\Gamma)+r\sin(r\sin\theta_\Gamma-2\theta_\Gamma)\right], \\
J^{\boldsymbol{\Phi}}(r) &= k\frac{\mathcal{A}_1}{2r^2}e^{-r\cos\theta_\Gamma}\cos\theta_\Gamma\left[\sin(r\sin\theta_\Gamma-\theta_\Gamma)+r\sin(r\sin\theta_\Gamma-2\theta_\Gamma)\right] \\
&\quad -k\frac{\mathcal{A}_2}{2r^2}e^{-r\cos\theta_\Gamma}\cos\theta_\Gamma\left[\cos(r\sin\theta_\Gamma-\theta_\Gamma)+r\cos(r\sin\theta_\Gamma-2\theta_\Gamma)\right].
\end{aligned}
$$

The magnetic field $\boldsymbol{B}$ is expressed as follows:

$$
\begin{aligned}
\frac{B_1^{\boldsymbol{Y}}(r)}{(-4\pi k\lambda_L)} &= -\frac{\mathcal{A}_1}{r^2}e^{-r\cos\theta_\Gamma}\left[\frac{1}{r}\sin(r\sin\theta_\Gamma)+\sin(r\sin\theta_\Gamma-\theta_\Gamma)\right] \\
&\quad +\frac{\mathcal{A}_2}{r^2}e^{-r\cos\theta_\Gamma}\left[\frac{1}{r}\cos(r\sin\theta_\Gamma)+\cos(r\sin\theta_\Gamma-\theta_\Gamma)\right], \qquad (2.96)\\
\frac{B_1^{\boldsymbol{\Psi}}(r)}{(-4\pi k\lambda_L)} &= \frac{\mathcal{A}_1}{2r^2}e^{-r\cos\theta_\Gamma}\left[\frac{1}{r}\sin(r\sin\theta_\Gamma)+\sin(r\sin\theta_\Gamma-\theta_\Gamma)+r\sin(r\sin\theta_\Gamma-2\theta_\Gamma)\right] \\
&\quad -\frac{\mathcal{A}_2}{2r^2}e^{-r\cos\theta_\Gamma}\left[\frac{1}{r}\cos(r\sin\theta_\Gamma)+\cos(r\sin\theta_\Gamma-\theta_\Gamma)+r\cos(r\sin\theta_\Gamma-2\theta_\Gamma)\right], \\
\frac{B_1^{\boldsymbol{\Phi}}(r)}{(-4\pi k\lambda_L)} &= \frac{\mathcal{A}_1}{2r^2}e^{-r\cos\theta_\Gamma}\left[\cos(r\sin\theta_\Gamma-\theta_\Gamma)+r\cos(r\sin\theta_\Gamma-2\theta_\Gamma)\right] \\
&\quad +\frac{\mathcal{A}_2}{2r^2}e^{-r\cos\theta_\Gamma}\left[\sin(r\sin\theta_\Gamma-\theta_\Gamma)+r\sin(r\sin\theta_\Gamma-2\theta_\Gamma)\right],
\end{aligned}
$$

while the magnetic field $\boldsymbol{H}$ takes the form:

$$
\begin{aligned}
\frac{H_1^{\boldsymbol{Y}}(r)}{(-4\pi k\lambda_L)} &= -\frac{\mathcal{A}_1}{r^2}e^{-r\cos\theta_\Gamma}\cos\theta_\Gamma\left[\frac{1}{r}\sin(r\sin\theta_\Gamma+\theta_\Gamma)+\sin(r\sin\theta_\Gamma)\right] \\
&\quad +\frac{\mathcal{A}_2}{r^2}e^{-r\cos\theta_\Gamma}\cos\theta_\Gamma\left[\frac{1}{r}\cos(r\sin\theta_\Gamma+\theta_\Gamma)+\cos(r\sin\theta_\Gamma)\right], \qquad (2.97)\\
\frac{H_1^{\boldsymbol{\Psi}}(r)}{(-4\pi k\lambda_L)} &= \frac{\mathcal{A}_1}{2r^2}e^{-r\cos\theta_\Gamma}\cos\theta_\Gamma\left[\frac{1}{r}\sin(r\sin\theta_\Gamma+\theta_\Gamma)+\sin(r\sin\theta_\Gamma)+r\sin(r\sin\theta_\Gamma-\theta_\Gamma)\right] \\
&\quad -\frac{\mathcal{A}_2}{2r^2}e^{-r\cos\theta_\Gamma}\cos\theta_\Gamma\left[\frac{1}{r}\cos(r\sin\theta_\Gamma+\theta_\Gamma)+\cos(r\sin\theta_\Gamma)+r\cos(r\sin\theta_\Gamma-\theta_\Gamma)\right], \\
\frac{H_1^{\boldsymbol{\Phi}}(r)}{(-4\pi k\lambda_L)} &= \frac{\mathcal{A}_1}{2r^2}e^{-r\cos\theta_\Gamma}\cos\theta_\Gamma\left[\cos(r\sin\theta_\Gamma)+r\cos(r\sin\theta_\Gamma-\theta_\Gamma)\right] \\
&\quad +\frac{\mathcal{A}_2}{2r^2}e^{-r\cos\theta_\Gamma}\cos\theta_\Gamma\left[\sin(r\sin\theta_\Gamma)+r\sin(r\sin\theta_\Gamma-\theta_\Gamma)\right].
\end{aligned}
$$

The vanishing of the normal component of the total current at the boundary of the spherical cavity (2.86) provides us with the following equation for the cavity radius R_0

for the general $l = 1$ solution:

$$\begin{aligned} 0 &= \mathcal{A}_1\Big(\cos(R_0\sin\theta_\Gamma) + R_0\cos(R_0\sin\theta_\Gamma - \theta_\Gamma)\Big) \\ &+ \mathcal{A}_2\Big(\sin(R_0\sin\theta_\Gamma) + R_0\sin(R_0\sin\theta_\Gamma - \theta_\Gamma)\Big)\,. \end{aligned} \tag{2.98}$$

This condition, which generalizes Eq. (2.87), has solutions for any radius R_0 of the cavity thus implying that the spheromak configuration can exist at any R_0. Equation (2.98) establishes a relation between the coefficients $\mathcal{A}_1$ and $\mathcal{A}_2$ of the generic solution.

It is easy to check that the generic spheromak solution has the same divergences as the solution considered in the previous section. For example, the divergent part of the spheromak energy is:

$$\mathcal{E}_1^{\rm div} = \frac{\pi k^2\lambda_L^8}{a_{\rm UV}^3}(\mathcal{A}_1^2 + \mathcal{A}_2^2)\cos^2\theta_\Gamma, \tag{2.99}$$

where the relation between the coefficients $\mathcal{A}_1$ and $\mathcal{A}_2$ is given by Eq. (2.98).

Setting the amplitudes $\mathcal{A}_1 = \mathcal{A}\sin\theta_\Gamma$ and $\mathcal{A}_2 = -\mathcal{A}\cos\theta_\Gamma$, we obtain the solution explored in the previous sections. For example, the divergent part of the spheromak energy is:

$$\mathcal{E}_1^{\rm div} = \frac{\pi k^2\lambda_L^8}{a_{\rm UV}^3}\mathcal{A}^2\sqrt{1-\Gamma^2}. \tag{2.100}$$

2.3.2 Configuration of the free magnetic field inside cavity

Since we assume the spherical cavity is empty, the Maxwell equations that determine the magnetic field take the following form:

$$\boldsymbol{\nabla}\times\boldsymbol{B} = 0, \quad \boldsymbol{\nabla}\cdot\boldsymbol{B} = 0\,. \tag{2.101}$$

Using expansion via vector spherical harmonics

$$\boldsymbol{B} = B^{\boldsymbol{Y}}_{lm}(r)\,\boldsymbol{Y}_{lm}(\hat{\boldsymbol{r}}) + B^{\boldsymbol{\Psi}}_{lm}(r)\,\boldsymbol{\Psi}_{lm}(\hat{\boldsymbol{r}}) + B^{\boldsymbol{\Phi}}_{lm}(r)\boldsymbol{\Phi}_{lm}(\hat{\boldsymbol{r}})\,, \tag{2.102}$$

and taking into account the expressions for the curl and divergence operators, described in detail in Appendix A.1, we obtain Maxwell's equations in the explicit form:

$$\begin{aligned} \boldsymbol{\nabla}\times\boldsymbol{B} &= \sum_{l=0}^{\infty}\sum_{m=-l}^{l}\Bigg(-\frac{l(l+1)}{r}B^{\boldsymbol{\Phi}}_{lm}\boldsymbol{Y}_{lm} - \Big(\frac{dB^{\boldsymbol{\Phi}}_{lm}}{dr} + \frac{1}{r}B^{\boldsymbol{\Phi}}_{lm}\Big)\boldsymbol{\Psi}_{lm} \\ &\qquad + \Big(-\frac{1}{r}B^{\boldsymbol{Y}}_{lm} + \frac{dB^{\boldsymbol{\Psi}}_{lm}}{dr} + \frac{1}{r}B^{\boldsymbol{\Psi}}_{lm}\Big)\boldsymbol{\Phi}_{lm}\Bigg)\,, \end{aligned} \tag{2.103}$$

$$\boldsymbol{\nabla}\cdot\boldsymbol{B} = \sum_{l=0}^{\infty}\sum_{m=-l}^{l}\left(\frac{dB^{\boldsymbol{Y}}_{lm}}{dr} + \frac{2}{r}B^{\boldsymbol{Y}}_{lm} - \frac{l(l+1)}{r}B^{\boldsymbol{\Psi}}_{lm}\right)Y_{lm}\,.$$

Thus, inside the spherical cavity, the Maxwell equation (2.101) can be represented as the following set of the differential equations on the (l,m) radial components of the vector spherical functions:

$$
\begin{aligned}
0 &= B^{\mathbf{\Phi}}_{lm}\,, && \text{(2.104a)}\\
0 &= \frac{dB^{\mathbf{\Phi}}_{lm}}{dr}+\frac{1}{r}B^{\mathbf{\Phi}}_{lm}\,, && \text{(2.104b)}\\
0 &= -\frac{1}{r}B^{\boldsymbol{Y}}_{lm}+\frac{dB^{\mathbf{\Psi}}_{lm}}{dr}+\frac{1}{r}B^{\mathbf{\Psi}}_{lm}\,, && \text{(2.104c)}\\
0 &= \frac{dB^{\boldsymbol{Y}}_{lm}}{dr}+\frac{2}{r}B^{\boldsymbol{Y}}_{lm}-\frac{l(l+1)}{r}B^{\mathbf{\Psi}}_{lm}\,. && \text{(2.104d)}
\end{aligned}
$$

Since, for arbitrary values of Γ we have an analytical solution only for $l=1$ ($m=-1,0,1$), for simplicity let consider the case with $(l,m)=(1,0)$. Maxwell equations (2.104) take the form :

$$
\begin{aligned}
0 &= B^{\mathbf{\Phi}}, && \text{(2.105a)}\\
0 &= \frac{dB^{\mathbf{\Phi}}}{dr}+\frac{1}{r}B^{\mathbf{\Phi}}, && \text{(2.105b)}\\
0 &= -\frac{1}{r}B^{\boldsymbol{Y}}+\frac{dB^{\mathbf{\Psi}}}{dr}+\frac{1}{r}B^{\mathbf{\Psi}}, && \text{(2.105c)}\\
0 &= \frac{dB^{\boldsymbol{Y}}}{dr}+\frac{2}{r}B^{\boldsymbol{Y}}-\frac{2}{r}B^{\mathbf{\Psi}}. && \text{(2.105d)}
\end{aligned}
$$

where, for convenience, we omit the indices "10" for the components.

The first equation (2.105a) gives us immediately $B^{\mathbf{\Phi}}=0$. The last two equations (2.105c) and (2.105d) provide us with a system of differential equations for two functions $B^{\boldsymbol{Y}}$ and $B^{\mathbf{\Psi}}$:

$$
0=-\frac{1}{r}B^{\boldsymbol{Y}}+\frac{dB^{\mathbf{\Psi}}}{dr}+\frac{1}{r}B^{\mathbf{\Psi}}, \qquad 0=\frac{dB^{\boldsymbol{Y}}}{dr}+\frac{2}{r}B^{\boldsymbol{Y}}-\frac{2}{r}B^{\mathbf{\Psi}}. \tag{2.106}
$$

or

$$
B^{\boldsymbol{Y}}=r\left(\frac{d}{dr}+\frac{1}{r}\right)B^{\mathbf{\Psi}}, \qquad 0=\left(\frac{d^2}{dr^2}+\frac{4}{r}\frac{d}{dr}\right)B^{\mathbf{\Psi}}. \tag{2.107}
$$

The general solution of this system is as follows:

$$
\begin{aligned}
B^{\boldsymbol{Y}} &= c_1+\frac{c_2}{r^3}\,, && \text{(2.108a)}\\
B^{\mathbf{\Psi}} &= c_1-\frac{c_2}{2r^3}\,. && \text{(2.108b)}
\end{aligned}
$$

In order to determine the magnetic field in the cavity, we need to consider the configuration of the magnetic field that does not diverge at the origin $r=0$ and, at the same time, is consistent with the boundary conditions at the interface. The first condition

sets $c_2 = 0$ in Eq. (2.108):

$$B^{\boldsymbol{Y}}(r) = \mathcal{B}\,, \tag{2.109a}$$

$$B^{\boldsymbol{\Psi}}(r) = \mathcal{B}\,, \tag{2.109b}$$

$$B^{\boldsymbol{\Phi}}(r) = 0\,, \tag{2.109c}$$

where we renamed the constant c_1 to $\mathcal{B}$. Taking into account the expansion of the magnetic field over vector spherical harmonics (2.102), the generic solution inside the cavity can be written in the form:

$$\boldsymbol{B} = \sum_{m=-l}^{l} \mathcal{B}_{1m} \left[\boldsymbol{Y}_{1m}(\hat{\boldsymbol{r}}) + \boldsymbol{\Psi}_{1m}(\hat{\boldsymbol{r}}) \right] , \tag{2.110}$$

where the constants $\mathcal{B}_{1m}$ are to be defined from the matching of the cavity field with the superconducting field at the cavity-superconductor interface. This procedure is discussed below.

Matching interface conditions

The interface conditions for the magnetic field vectors are as follows:

$$0 = \boldsymbol{n}_{12} \cdot (\boldsymbol{B}_2 - \boldsymbol{B}_1)\,, \tag{2.111a}$$

$$\boldsymbol{J}_S = \boldsymbol{n}_{12} \times (\boldsymbol{H}_2 - \boldsymbol{H}_1)\,, \tag{2.111b}$$

where $\boldsymbol{n}_{12}$ is normal vector from medium 1 (the vacuum cavity) to medium 2 (the parity-odd superconductor) and $\boldsymbol{J}_S$ is the surface current density which is localized at the interface.

We represent these conditions in the following form:

$$0 = \boldsymbol{B}_{2,n} - \boldsymbol{B}_{1,n}, \tag{2.112a}$$

$$\boldsymbol{J}_S = \boldsymbol{H}_{2,\tau} - \boldsymbol{H}_{1,\tau}, \tag{2.112b}$$

where the indices n and τ denote the normal and tangential components, respectively. The fields $\boldsymbol{B}$, $\boldsymbol{H}$ and the current $\boldsymbol{J}$, expanded over the vector spherical harmonics, give us the following equations for each (l, m) harmonics:

$$0 = \left(B^{\boldsymbol{Y}}_{2,lm} - B^{\boldsymbol{Y}}_{1,lm}\right) \boldsymbol{Y}_{lm}, \tag{2.113a}$$

$$J^{\boldsymbol{\Psi}}_{S,lm} \boldsymbol{\Psi}_{lm} + J^{\boldsymbol{\Phi}}_{S,lm} \boldsymbol{\Phi}_{lm} = \left(H^{\boldsymbol{\Psi}}_{2,lm} - H^{\boldsymbol{\Psi}}_{1,lm}\right) \boldsymbol{\Psi}_{lm} + \left(H^{\boldsymbol{\Phi}}_{2,lm} - H^{\boldsymbol{\Phi}}_{1,lm}\right) \boldsymbol{\Phi}_{lm}. \tag{2.113b}$$

Since the cavity has properties of the vacuum, the magnetic field $\boldsymbol{B}$ and the field $\boldsymbol{H}$

inside the cavity coincide with each other. Finally we obtain the following boundary conditions (we omit again the indices l and m):

$$B_1^{\boldsymbol{Y}}(R_0) = B_2^{\boldsymbol{Y}}(R_0), \tag{2.114a}$$

$$B_1^{\boldsymbol{\Psi}}(R_0) = H_2^{\boldsymbol{\Psi}}(R_0) - J_S^{\boldsymbol{\Psi}}, \tag{2.114b}$$

$$B_1^{\boldsymbol{\Phi}}(R_0) = H_2^{\boldsymbol{\Phi}}(R_0) - J_S^{\boldsymbol{\Phi}}. \tag{2.114c}$$

2.3.3 Consistent $l = 1$ solution in the whole space

Finally we have all the ingredients to construct the spheromak solution in the whole space. For this purpose we consider the lowest-energy, $(l, m) = (1, m)$ spheromak configurations with $m = -1, 0, 1$. The complete solution can be obtained by analyzing the previously obtained equalities and expressions.

The condition (2.85) gives us $B_1^{\boldsymbol{\Phi}}(R_0) = -J_S^{\boldsymbol{\Phi}}$ from (2.114c). At the same time, based on the solution for the field in the cavity, we know that $B_1^{\boldsymbol{\Phi}}(r) = 0$ (2.109c), from which it follows that the surface current lacks the $\boldsymbol{\Phi}$ - component. Moreover, the boundary condition (2.114a) provides us the value of the $\boldsymbol{Y}$ component of the magnetic field in the cavity (2.109a) and therefore the value of the constant $\mathcal{B}$, which also determines the value of $\boldsymbol{\Psi}$ component (2.109b). Thus, we obtain the following expressions for the magnetic field inside the cavity, $\boldsymbol{B}_{\rm cav} \equiv \boldsymbol{B}_1$ and the surface current, respectively:

$$\boldsymbol{B}_{{\rm cav},m} = \mathcal{B}\boldsymbol{Y}_{1m} + \mathcal{B}\boldsymbol{\Psi}_{1m}\,, \tag{2.115a}$$

$$\boldsymbol{J}_S = \big(H_2^{\boldsymbol{\Psi}}(R_0) - \mathcal{B}\big)\boldsymbol{\Psi}_{1m}\,, \tag{2.115b}$$

where these radial functions are the same for all projections of the angular momenta $m = -1, 0, +1$. The $\boldsymbol{\Psi}$ component of the magnetic field $\boldsymbol{H}$ at the medium "2" (i.e., superconductor), given in Eq. (2.84), should be evaluated at the inner shell of the radius R_0. The latter is given by the solution of Eq. (2.87) which, in the limit of weak parity violation, is given by Eq. (2.91).

The surface current has the following explicit expression:

$$\boldsymbol{J}_{S,m}(\hat{\boldsymbol{r}}) = J_S^{\boldsymbol{\Psi}}\,\boldsymbol{\Psi}_{1m}(\hat{\boldsymbol{r}})\,. \tag{2.116}$$

Since the surface current exists only at the interface between the superconductor and the cavity, it depends only on the angular variables encoded in the vector spherical function $\boldsymbol{\Psi}_{1m}$. The radial component of the current (2.116) is a constant:

$$\begin{aligned} J_S^{\boldsymbol{\Psi}} = &- 2\pi k\lambda_L \frac{\mathcal{A}}{R_0^3} e^{-R_0\cos\theta_\Gamma}\Big[\cos\theta_\Gamma\cos(R_0\sin\theta_\Gamma) \\ &+ \Big(2 + R_0\cos\theta_\Gamma\Big)\Big(\cos(R_0\sin\theta_\Gamma - \theta_\Gamma) + R_0\cos(R_0\sin\theta_\Gamma - 2\theta_\Gamma)\Big)\Big]\,. \end{aligned} \tag{2.117}$$

The dependence of this component on the parameter Γ is shown in Fig. 2.12. In the limit $\Gamma \to 0$ (or $\theta_\Gamma \to 0$) we have:

$$J_S^{\Psi} = -2\pi k \lambda_L \mathcal{A} \frac{R_0^2 + 3R_0 + 3}{R_0^3} e^{-R_0} + O(\Gamma^2)\,. \tag{2.118}$$

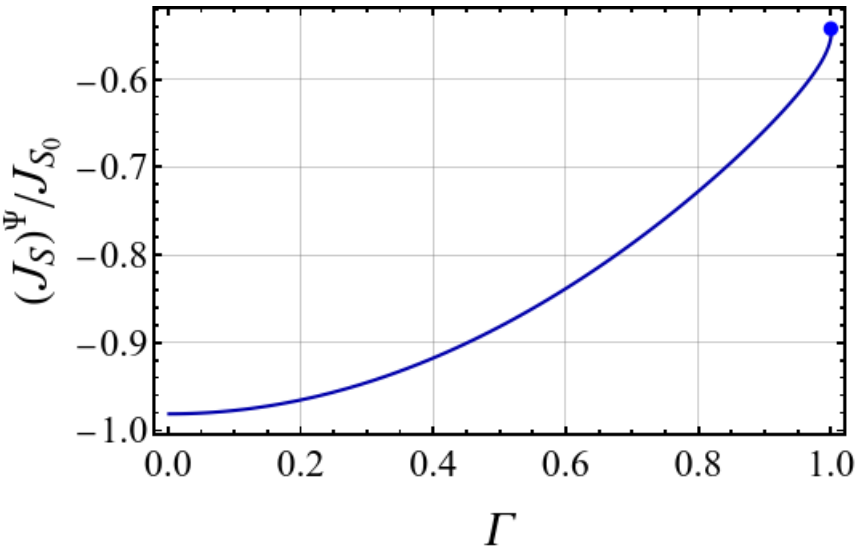

Figure 2.12: Dependence of the $\boldsymbol{\Psi}$-component of the surface current $\boldsymbol{J}_S$ on the parity-odd strength Γ. The magnitude is shown in the units of $J_{S_0} = \pi k \lambda_L \mathcal{A}$.

The magnitude of the magnetic field $\mathcal{B}$ is defined by the matching conditions at the boundary. In this case we obtain:

$$\mathcal{B} \;=\; 4\pi k \lambda_L \frac{\mathcal{A}}{R_0^2} e^{-R_0 \cos\theta_\Gamma} \left[\cos(R_0 \sin\theta_\Gamma - 2\theta_\Gamma) + \frac{1}{R_0} \cos(R_0 \sin\theta_\Gamma - \theta_\Gamma) \right]. \tag{2.119}$$

In the limit of weak parity-odd violation, $\Gamma \ll 1$, one gets the following matching condition:

$$\mathcal{B} = 4\pi k \lambda_L \mathcal{A} \frac{1 + R_0}{R_0^3} e^{-R_0} + O(\Gamma^2)\,. \tag{2.120}$$

The structure of the streamlines of the magnetic field $\boldsymbol{H}$ and the electric current $\boldsymbol{J}$ for the parity breaking parameters $\Gamma = 0.1$ and $\Gamma = 0.5$ are shown in Figs. 2.13. In agreement with the general properties of the solution, the intertwining magnetic field penetrate the central cavity while the electric current is tangential to the cavity surface, as expected. The multiple nested toroidal structures of the electric current are clearly seen in the bottom plot. The geometrical features of the spheromak configuration at low values of the parity-odd parameter Γ stay the same up to moderate values of Γ. The influence of the magnitude of the parity breaking parameter Γ and the value of the projection $m = 0, 1$ on the structure of the spheromak solution is illustrated in Fig. 2.14. A noticeable difference in properties of the magnetic field H and the current J appears at higher values of the parameter Γ. Notice that while the $(l, m) = (1, 1)$ visually resembles a rotated $(l, m) = (1, 0)$ solution, it is not the case: these are two different, linearly-independent solutions.

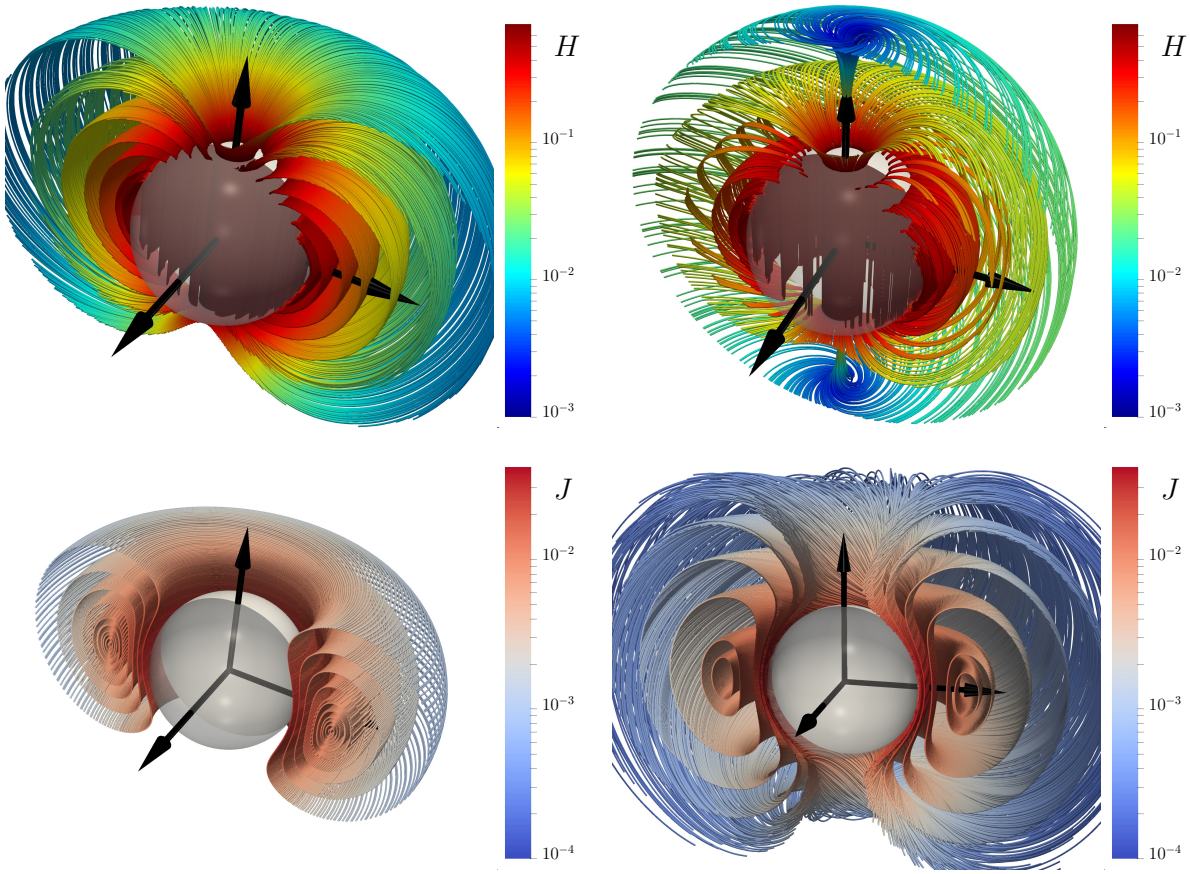

(a) (b)

Figure 2.13: (a) Spheromak solution for the angular momentum numbers $(l, m) = (1, 0)$ and the parity breaking parameter $\Gamma = 0.1$. The top panel displays streamlines of the magnetic field H, and the bottom panel shows streamlines of the current J. The sphere in the center shows the vacuum cavity. (b) The same but for the parity breaking parameter $\Gamma = 0.5$.

Energy of the compact solution

The energy of the magnetic field inside the cavity can be calculated using Eqs. (2.69) in the second line and (2.87) in the third line:

$$\begin{aligned}
\mathcal{E}_{\rm cav} &= \frac{1}{8\pi}\int dV \boldsymbol{B}_1^2 \\
&= \frac{\lambda_L^3}{8\pi}\int_0^{R_0} dr r^2 \mathcal{B}^2 \left[\int d\Omega \left(\boldsymbol{Y}_{10}\right)^2 + \int d\Omega \left(\boldsymbol{\Psi}_{10}\right)^2\right] = \frac{\lambda_L^3 R_0^3}{8\pi}\mathcal{B}^2 \qquad (2.121)\\
&= 2\pi k^2 \lambda_L^5 \mathcal{A}^2 \frac{e^{-2R_0\cos\theta_\Gamma}}{R_0}\left(\cos(R_0\sin\theta_\Gamma - 2\theta_\Gamma) + \frac{1}{R_0}\cos(R_0\sin\theta_\Gamma - \theta_\Gamma)\right)^2 \\
&= 2\pi k^2 \lambda_L^5 \mathcal{A}^2 \frac{e^{-2R_0\cos\theta_\Gamma}}{R_0^3}\left(1 + R_0^2 + 2R_0\cos\theta_\Gamma\right),
\end{aligned}$$

The dependence of the energy of magnetic field (2.121) inside the cavity on the parity-odd parameter Γ outside the cavity is shown in Fig. 2.15. It is important that the energy is finite for all values of the parity-odd parameter Γ. We remind that despite

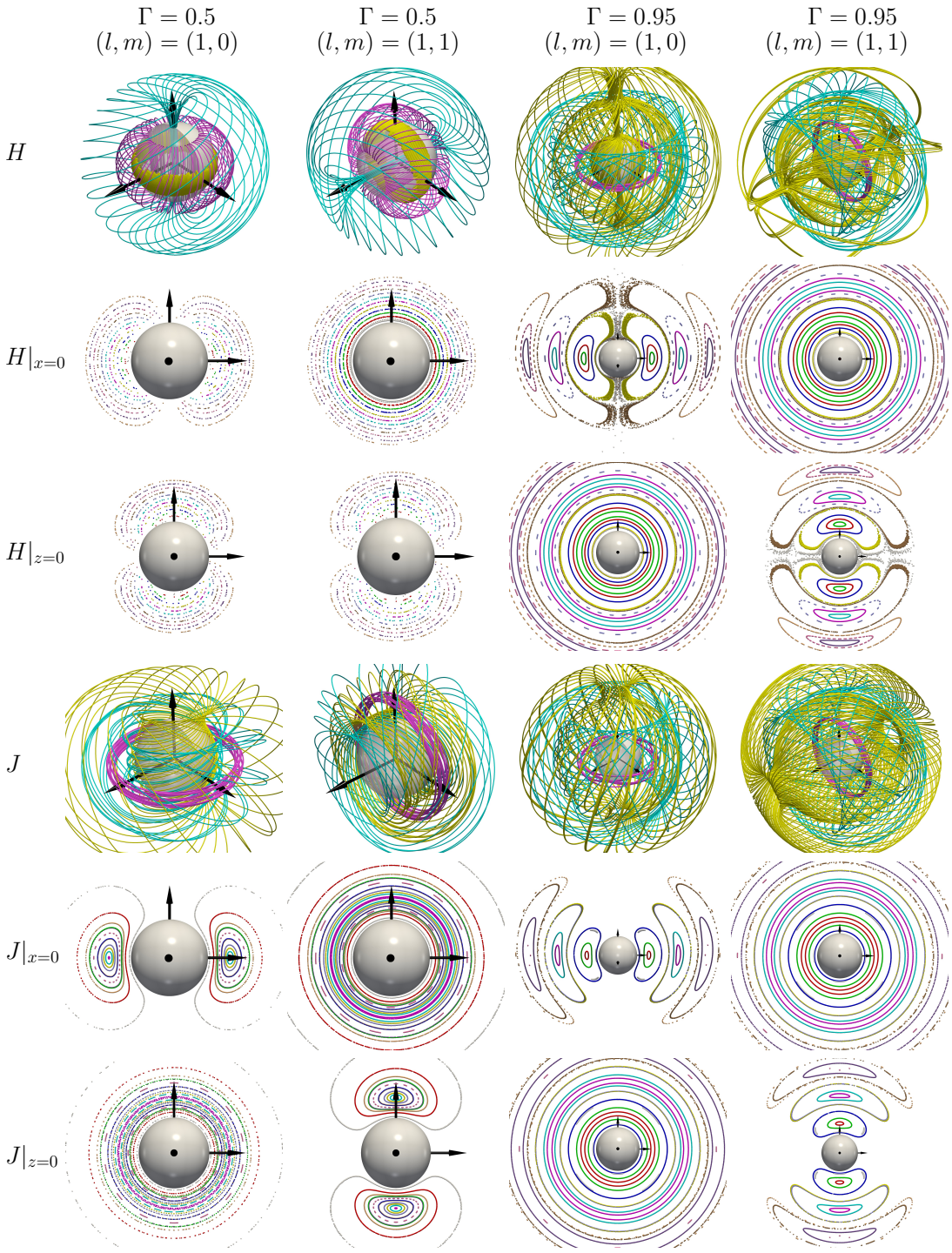

Figure 2.14: The structure of the streamlines of the magnetic field H and the electric current J, for the lowest-energy spheromak with the projections $m = 0, 1$ of the total orbital momentum $l = 1$ for the two values of the parity-odd parameter: $\Gamma = 0.5$ and 0.95. The line on the top row shows streamlines of H, and the two next rows show the Poincaré sections of the streamlines of H on the $x = 0$ and $z = 0$ planes respectively. Similarly, the block of the three bottom rows indicate the structure of the current J. The central sphere depicts the vacuum cavity.

the material in the cavity is a parity-even medium (vacuum), the total energy of the magnetic field inside the cavity (2.121) depends on the parity-odd parameter Γ which determines the configuration of the spheromak field outside the cavity and, eventually, via the interface matching conditions (2.111), influences the field inside the cavity.

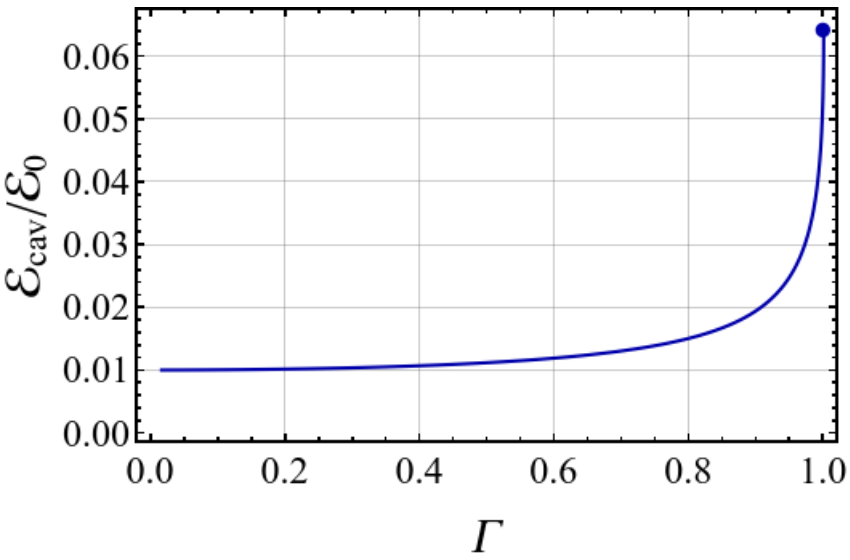

Figure 2.15: Dependence of the magnetic field energy in the cavity (2.121) on the parameter Γ. Energy is expressed in units of $\mathcal{E}_0 = 4\pi^2 k^2 \lambda_L^5 \mathcal{A}^2$.

The total energy of the lowest-energy $l = 1$ spheromak solutions localized around the cavity is given by the sum of the in-cavity free magnetic field (2.121) and the GL energy (2.52) in the exterior of the cavity:

$$\mathcal{E} = \mathcal{E}_{\rm cav} + \mathcal{E}_1(R_0)\,, \tag{2.122}$$

where the limit of integration in the GL energy functional (2.52) is set to be the radius of the cavity R_0. The energy of the magnetic field, both inside the cavity and at zero, no longer diverges. The dependence of the total energy (2.122) on the parity-odd parameter Γ is shown in Fig. 2.16. It should be noted that at the maximal value of the parity-odd parameter, $\Gamma = 1$, the energy of the solution in the superconductor vanishes, and the energy of the cavity has a finite, non-divergent value.

Finally, we present the total energy of the $l = 1$ spheromak in the limit of small Γ:

$$\frac{\mathcal{E}(\Gamma)}{\mathcal{E}_0} = \frac{e^{-1-\sqrt{5}}}{6\pi}\left(3 + 3\sqrt{5} + \left(3 - \sqrt{5}\right)\Gamma^2\right), \tag{2.123}$$

where the higher-order $O(\Gamma^4)$ terms are not shown and the expression for $\mathcal{E}_0 = 4\pi^2 k^2 \lambda_L^5 \mathcal{A}^2$.

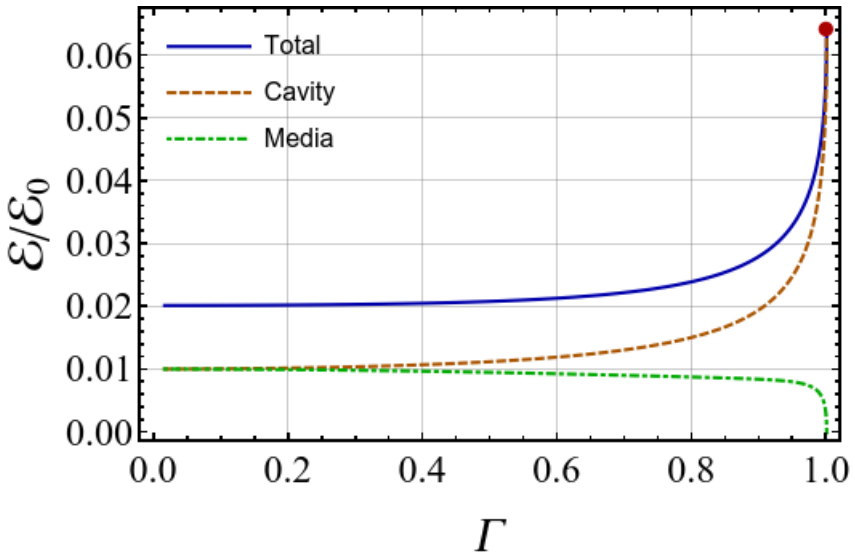

Figure 2.16: Dependences of the total energy of the system (blue solid line), the energy of the magnetic field in the cavity (2.121) (orange dash-dotted line) and the energy of the superconducting state (2.52) (green dotted line) on parameter Γ. The red dot indicates the finiteness of the energy at $\Gamma = 1$. Energy is expressed in units of $\mathcal{E}_0 = 4\pi^2 k^2 \lambda_L^5 \mathcal{A}^2$.

Helicity of the compact solution

In order to calculate the contribution to the total helicity (2.74) coming from the fields in the cavity,

$$\mathcal{H}_{\rm cav} = \int d^3\boldsymbol{r}\ \boldsymbol{A}_{\rm cav} \cdot \boldsymbol{B}_{\rm cav}\,, \tag{2.124}$$

we need to determine the explicit form of the vector potential $\boldsymbol{A}_{\rm cav}$ in the cavity. Using the definition of magnetic field,

$$\frac{1}{\lambda_L}\boldsymbol{\nabla} \times \boldsymbol{A}_{\rm cav} = \boldsymbol{B}_{\rm cav}\,, \tag{2.125}$$

and expanding vector fields in terms of vector spherical harmonics, we find the following relations:

$$\begin{aligned} &-\frac{2}{r}A^{\boldsymbol{\Phi}}_{\rm cav}\boldsymbol{Y}_{1m} - \left(\frac{dA^{\boldsymbol{\Phi}}_{\rm cav}}{dr} + \frac{1}{r}A^{\boldsymbol{\Phi}}_{\rm cav}\right)\boldsymbol{\Psi}_{1m} + \left(-\frac{1}{r}A^{\boldsymbol{Y}}_{\rm cav} + \frac{dA^{\boldsymbol{\Psi}}_{\rm cav}}{dr} + \frac{1}{r}A^{\boldsymbol{\Psi}}_{\rm cav}\right)\boldsymbol{\Phi}_{1m} \\ &= \lambda_L\left[\mathcal{B}\boldsymbol{Y}_{1m} + \mathcal{B}\boldsymbol{\Psi}_{1m}\right]. \end{aligned} \tag{2.126}$$

It should be noted that in Eq. (2.125) the factor λ_L appears due to the use of the rescaled dimensionless coordinates (2.21).

In the component notation, Eq. (2.126) can be split into three equations:

$$-\frac{2}{r\lambda_L}A^{\boldsymbol{\Phi}}_{\rm cav} = \mathcal{B}\,, \tag{2.127a}$$

$$-\frac{1}{\lambda_L}\left(\frac{dA^{\boldsymbol{\Phi}}_{\rm cav}}{dr} + \frac{1}{r}A^{\boldsymbol{\Phi}}_{\rm cav}\right) = \mathcal{B}\,, \tag{2.127b}$$

$$-\frac{1}{r}A^{\boldsymbol{Y}}_{\rm cav} + \frac{dA^{\boldsymbol{\Psi}}_{\rm cav}}{dr} + \frac{1}{r}A^{\boldsymbol{\Psi}}_{\rm cav} = 0. \tag{2.127c}$$

The first equation (2.127a) gives us a relation

$$A^{\mathbf{\Phi}}_{\rm cav} \;=\; -\frac{r\lambda_L}{2}\mathcal{B}\,, \tag{2.128}$$

which is in full agreement with the second equation of the system (2.127). At the same time, the third equation gives a simple relation between the components $\boldsymbol{Y}$ and $\mathbf{\Psi}$:

$$\frac{1}{r}A^{\boldsymbol{Y}}_{\rm cav} = \frac{dA^{\mathbf{\Psi}}_{\rm cav}}{dr} + \frac{1}{r}A^{\mathbf{\Psi}}_{\rm cav}\,. \tag{2.129}$$

The above relations admit an ambiguity which can be expressed via the choice of the component $A^{\mathbf{\Psi}}_{\rm cav} = a$, where a is a constant. Then Eq. (2.129) fixes other components of the vector potential, $A^{\boldsymbol{Y}}_{\rm cav} = A^{\mathbf{\Psi}}_{\rm cav} = a$. In general, the helicity in the cavity will be determined by the magnitude of a taking a nonvanishing value if $a \neq 0$. But, if we choose $a = 0$, then the helicity in the cavity vanishes, since the third component of the magnetic field in the cavity is equal to zero. In order to fix this ambiguity, it is necessary to correctly match the vector potentials of the cavity and the superconducting medium at the boundary of the cavity.

The tangential components of the vector potential are always continuous at the boundary while the normal components may have a discontinuity across the boundary. In our vortex-free solution in the superconducting medium (at $r > R_0$), the relation between the corresponding vector potential $\boldsymbol{A}$ and the current $\boldsymbol{j}$ has a linear form:

$$\boldsymbol{A} = -4\pi k\lambda_L^2\boldsymbol{j}\,, \qquad [r > R_0]\,. \tag{2.130}$$

Due to the electric charge conservation (2.33), the vector potential field in the superconducting medium is a solenoidal vector field which satisfies the Coulomb gauge $\boldsymbol{\nabla}\cdot\boldsymbol{A} = 0$. To keep the solutions smooth across the boundary, we choose the same Coulomb gauge condition in the cavity. This requirement implies that the normal components, similarly to the tangential components, are continuous across the interface between the superconducting medium and the cavity.

The continuity of the gauge fields across the boundary sets the boundary conditions for the fields in the cavity:

$$\boldsymbol{A}_{\rm cav}(R_0) = \boldsymbol{A}(R_0)\,, \tag{2.131}$$

or, explicitly in components:

$$A^{\boldsymbol{Y}}_{\rm cav}(R_0) \;=\; A^{\boldsymbol{Y}}(R_0) = 2\xi\left(\frac{1}{R_0}\sin\alpha_0 + \sin\alpha_1\right), \tag{2.132a}$$

$$A^{\mathbf{\Psi}}_{\rm cav}(R_0) \;=\; A^{\mathbf{\Psi}}(R_0) = -\xi\left(\frac{1}{R_0}\sin\alpha_0 + \sin\alpha_1 + R_0\sin\alpha_2\right), \tag{2.132b}$$

$$A^{\mathbf{\Phi}}_{\rm cav}(R_0) \;=\; A^{\mathbf{\Phi}}(R_0) = -\xi\left(\frac{1}{R_0}\cos\alpha_1 + R_0\cos\alpha_2\right), \tag{2.132c}$$

with

$$\alpha_n = R_0 \sin\theta_\Gamma - n\theta_\Gamma \quad \text{and} \quad \xi = 2\pi k\lambda^2 \frac{\mathcal{A}}{R_0^2} e^{-R_0\cos\theta_\Gamma} \,. \tag{2.133}$$

Using equation (2.87) that expresses the dependence of the cavity radius on an parity-odd parameter θ_Γ, we can drop the second and third terms in Eq. (2.132b). The equality for the $\mathbf{\Phi}$'s component (2.132c) of the vector potential is satisfied automatically by virtue of Eq. (2.128).

Finally, in order to obtain the explicit form of the vector potential in the cavity, we solve a system of two ordinary differential equations:

$$(\boldsymbol{\nabla} \times \boldsymbol{A}_{\text{cav}})^{\mathbf{\Phi}} = 0 = -\frac{1}{r} A^{\boldsymbol{Y}}_{\text{cav}} + \frac{dA^{\mathbf{\Psi}}_{\text{cav}}}{dr} + \frac{1}{r} A^{\mathbf{\Psi}}_{\text{cav}}, \tag{2.134a}$$

$$\boldsymbol{\nabla} \cdot \boldsymbol{A}_{\text{cav}} = 0 = \frac{dA^{\boldsymbol{Y}}_{\text{cav}}}{dr} + \frac{2}{r} A^{\boldsymbol{Y}}_{\text{cav}} - \frac{2}{r} A^{\mathbf{\Psi}}_{\text{cav}}, \tag{2.134b}$$

with the corresponding boundary conditions:

$$A^{\boldsymbol{Y}}_{\text{cav}}(R_0) = 2\xi \left(\frac{1}{R_0} \sin\alpha_0 + \sin\alpha_1 \right) , \tag{2.135a}$$

$$A^{\mathbf{\Psi}}_{\text{cav}}(R_0) = -\xi \frac{1}{R_0} \sin\alpha_0 \,. \tag{2.135b}$$

The general solution has the following form:

$$A^{\boldsymbol{Y}}_{\text{cav}}(r) = \frac{2c_1}{r^3} + c_2 \,, \tag{2.136a}$$

$$A^{\mathbf{\Psi}}_{\text{cav}}(r) = -\frac{c_1}{r^3} + c_2 \,. \tag{2.136b}$$

Taking into account the boundary condition (2.131), we obtain the two constants in an explicit form:

$$c_1 = \xi R_0^3 \left(\frac{1}{R_0} \sin\alpha_0 + \frac{2}{3} \sin\alpha_1 \right) , \tag{2.137a}$$

$$c_2 = \xi \frac{2}{3} \sin\alpha_1 \,. \tag{2.137b}$$

The solution for the vector-potential in the cavity is as follows:

$$A^{\boldsymbol{Y}}_{\text{cav}}(r) = \xi \left[\frac{2}{3} \sin\alpha_1 + 2\frac{R^3}{r^3} \left(\frac{1}{R_0} \sin\alpha_0 + \frac{2}{3} \sin\alpha_1 \right) \right] ,$$

$$A^{\mathbf{\Psi}}_{\text{cav}}(r) = \xi \left[\frac{2}{3} \sin\alpha_1 - \frac{R^3}{r^3} \left(\frac{1}{R_0} \sin\alpha_0 + \frac{2}{3} \sin\alpha_1 \right) \right] .$$

Now we have all ingredients to compute unambigously the contribution to the total helicity from the gauge fields in the cavity:

$$\begin{aligned}\mathcal{H}_{\rm cav} &= \int d^3\boldsymbol{x}\ \boldsymbol{A}_{\rm cav}\cdot\boldsymbol{B}_{\rm cav} = \lambda_L^3\int d^3\boldsymbol{r}\ \boldsymbol{A}_{\rm cav}\cdot\boldsymbol{B}_{\rm cav}\\ &= \lambda_L^3\int dr r^2\mathcal{B}\left(A^{\boldsymbol{Y}}_{\rm cav}+2A^{\boldsymbol{\Psi}}_{\rm cav}\right)\\ &= \frac{16}{3}\pi^2k^2\lambda_L^6\frac{\mathcal{A}^2}{R_0}e^{-2R_0\cos\theta_\Gamma}\sin(R_0\sin\theta_\Gamma-\theta_\Gamma)\\ &\times \left[\cos(R_0\sin\theta_\Gamma-2\theta_\Gamma)+\frac{1}{R_0}\cos(R_0\sin\theta_\Gamma-\theta_\Gamma)\right],\end{aligned} \tag{2.139}$$

where in the second line we, as usually, used the expansion of field $\boldsymbol{A}_{\rm cav}$ and $\boldsymbol{B}_{\rm cav}$ over vector spherical harmonics and relation (2.69).

Figure 2.17 shows the individual contributions to total helicity coming from the fields in the cavity, superconductor, and the total helicity. In the parity-even limit $\Gamma\to 0$, the total helicity vanishes while in the limit of the maximal parity violation, $\Gamma\to 1$, the total helicity diverges. The ratio of the total helicity and the total energy of the spheromak solution remains, however, finite (Fig. 2.18).

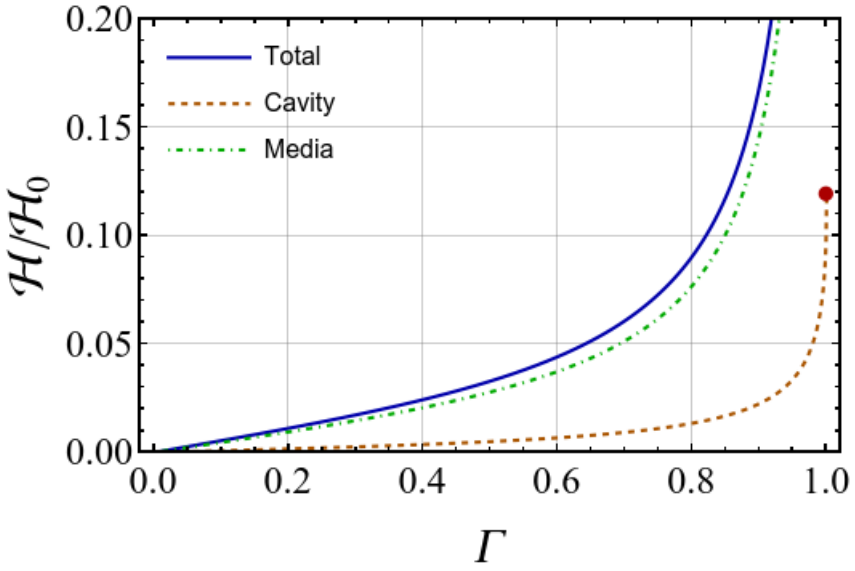

Figure 2.17: The total helicity of the lowest-energy $l=1$ superconducting spheromak solution (the blue solid line), the helicity of the magnetic field in the cavity (2.139) (the orange dashed line), and the helicity of the spheromak in the superconducting part outside the cavity (2.75) (the green dash-dotted line) on the parity-odd parameter Γ. The red dot indicates the value of the helicity of the magnetic field in the cavity at $\Gamma=1$. The helicity is shown in the units of $\mathcal{H}_0=16\pi^2k^2\lambda_L^6\mathcal{A}^2$.

We would like to stress that that the finite-energy spheromak solutions exist even in the limit $\Gamma\to 0$ which corresponds to the absence of the parity breaking. While the helicity of the $\Gamma=0$ configuration is exactly zero, the existence of these solutions

is not surprising given the emergence of these Chandrasekhar-Kendall states in the chirality-neutral astrophysical [42] and nuclear fusion [43] plasmas.

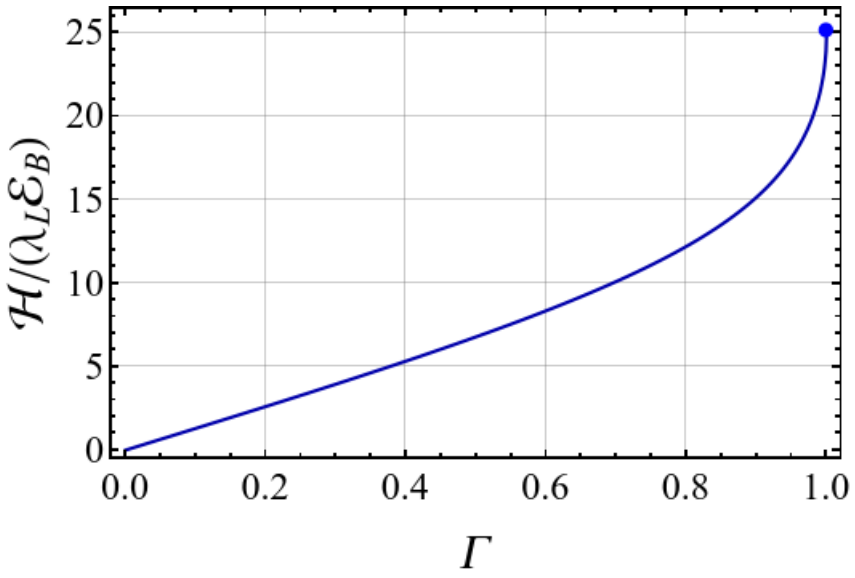

Figure 2.18: The total helicity of the $l = 1$ spheromak, normalized to the total energy of magnetic field, as a function of the parity-breaking parameter Γ. The blue dot indicates the finite value of the normalized helicity at $\Gamma = 1$.

2.3.4 Estimations of physical characteristics

Let us estimate the typical parameters of the superconducting spheromak solution for realistic superconductors. For a typical value of London penetration depth, $\lambda_L \simeq 100\,\text{nm}$, the radius of the superconducting cavity is given by the golden ratio (2.90), $R = \mathcal{R}\lambda_L \simeq 160\,\text{nm}$.

The strength of the magnetic field of spheromak as well as its energy are not quantized contrary to the Abrikosov vortices. Therefore, the energy of spheromak can be made arbitrarily low which could facilitate its engineering. However, in order to estimate a typical range of energies involved and compare them with the physical scales of the Abrikosov vortices, let us assume that the magnetic field inside the cavity has the fraction f of the magnetic field $B(r = 0)$ in the center of an Abrikosov vortex in the strong type-II (London) regime:

$$B(r = 0) \simeq \frac{\Phi_0}{2\pi\lambda_L^2} \ln \kappa, \tag{2.140}$$

where $\Phi_0 = h/(2e)$ is the magnetic flux quantum and κ is the Ginzburg-Landau parameter (2.5). The magnetic field inside the cavity (2.115a) is fixed by the factor $\mathcal{B}$. Therefore, setting $\mathcal{B} = fB(r = 0)$, we can use then Eq. (2.140) as well as Eq. (2.119) to find the magnitude parameter $\mathcal{A}$ which determines the energy of the total solution (2.122).

The latter quantity, shown in Fig. 2.16, has the energy scale $\mathcal{E}_0 = 4\pi^2 k^2 \lambda_L^5 \mathcal{A}^2$. One gets:

$$\mathcal{E}_{\rm sph} \simeq \frac{f^2 \Phi_0^2 \mathcal{R}^3}{32\pi^3 \lambda_L} \ln^2 \kappa \,. \tag{2.141}$$

Choosing the typical superconducting coherence length $\xi \sim 1\,\text{nm}$, we get for the spheromak energy (2.141) the estimation $\mathcal{E}_{\rm sph} \simeq 20 f^2\,\text{eV}$. For a spheromak with the central magnitude of the magnetic field being just 1% of the vortex field (i.e., with $f = 0.01$), one gets the spheromak energy $\mathcal{E}_{\rm sph} \simeq 2\,\text{meV}$ which corresponds to the thermal scale of $\mathcal{E}/k_B \simeq 23\,\text{K}$.

For convenience, we finish this chapter with a short summary. The finite-energy superconducting spheromak solution can be realized as a gapped Chandrasekhar-Kendall state pinned at a spherical nonconducting cavity of the radius R. The minimal-energy configuration, characterized by the orbital momentum $l = 1$, is triply degenerate in terms of the projection number, $m = -1, 0, +1$. For all these spheromaks, the radius of the cavity R, in terms of the dimensionless units $R_0 = R/\lambda_L$, is determined by Eq. (2.87). For small (realistic) values of the parity broken parameter γ, related to the auxiliary dimensionless parity-odd parameter Γ, Eq. (2.24), and the parity-odd angle θ_Γ, Eq. (2.49), the minimal radius of the cavity (2.91) is determined by the golden ratio (2.90).

Inside the nonconducting cavity, $r < R$, the magnetic field $\boldsymbol{B}_{\rm cav}$ of the spheromak is given by Eq. (2.115a) and the electric current is, obviously, vanishing. The surface current $\boldsymbol{J}_S$, however, appears at the interface (2.116), $r = R$, between the cavity and the parity-odd superconductor. The superconducting exterior at $r > R$ hosts the electric current (2.83) and the magnetic field (2.84). All expressions are given in the basis of the vector spherical harmonics described in detail in Appendix A.

Chapter 3

Configurations induced by ferromagnetic inclusions

In this chapter, we express the London equation in terms of a force-free field, which allows us to obtain explicit solutions for all values of (l, m). There, we also determine the energy and helicity densities for the infinite tower of these states. Next we demonstrate that a ferromagnetic inclusion regularizes the singular behavior of the solution, serving, at the same time, as a source for a finite-energy superconducting knotted solution. We further investigate the case where the inclusion is a ferromagnetic dipole. There, we explicitly construct solutions sourced by such an impurity. Finally, we discuss their properties and the influence of the parity breaking parameter on the structure, energy, and helicity of knotted configurations. In this chapter we coin these solutions "toroflux", since in the course of studying ferromagnetic inclusions, we notice that the geometry of their current and flux lines resemble a popular toroflux toy.

3.1 Localized force-free solutions

In Section 1.4 we brifly presented the derivation of Ginzburg-Landau free energy done by E. Babaev and A. Samoilenka [58] from the microscopic model. Thus, in the vicinity of the superconducting critical temperature, this density $\mathcal{F}$ of the Ginzburg-Landau free energy $F = \int d^3x\mathcal{F}$ can be written as follows:

$$\mathcal{F} = \frac{\boldsymbol{B}}{8\pi} + \frac{k}{2}\sum_{a=\pm}|\boldsymbol{\mathcal{D}}_a\psi|^2 + \frac{\beta}{2}(|\psi|^2 - |\psi_0|^2), \tag{3.1}$$

where $\boldsymbol{\mathcal{D}}_\pm \equiv \boldsymbol{\nabla} - ie\boldsymbol{A} + ie\varkappa_\pm\boldsymbol{B}$.

The single - component order parameter $\psi = |\psi|e^{i\varphi}$ stands for the density of Cooper pairs. The gauge derivative $\boldsymbol{\mathcal{D}}$ couples the scalar field ψ to the vector potential $\boldsymbol{A}$ and the magnetic field $\boldsymbol{B} = \boldsymbol{\nabla}\times\boldsymbol{A}$. The coefficients of the Ginzubrg - Landau model (3.1), including the parity-breaking couplings $\varkappa_\pm = \varkappa \pm \nu$, can be expressed, as we metioned above, in terms of the parameters of the microscopic model [58, 62].

In the microscopic single-particle Hamiltonian, the parity-odd terms originate from the antisymmetric spin-orbit couplings $\boldsymbol{g}_k \cdot \boldsymbol{\sigma}$ with $\boldsymbol{g}_k = -\boldsymbol{g}_{-\boldsymbol{k}}$ and the Pauli matrices $\boldsymbol{\sigma}$ acting on the spin space [94]. The parity-odd couplings $\varkappa_\pm$, allowed by the parity-broken nature of the noncentrosymmetric superconductors, are nonvanishing but have parametrically small values [21].

The last term in the gauge derivative $\boldsymbol{\mathcal{D}}$ that appear in the free energy (3.1) corresponds to the Lifshitz invariant associated with the O point group symmetry. This term reflects the breaking of the parity symmetry in the system. Indeed, under the parity inversion, $P(\boldsymbol{x}) = -\boldsymbol{x}$, the magnetic field transforms as a parity-even quantity $P(\boldsymbol{B}) = -\boldsymbol{B}$ while the other terms in the derivative transform as vectors, $P(\boldsymbol{\mathcal{D}}_\pm) = -\boldsymbol{\mathcal{D}}_\pm + 2ie\varkappa_\pm \boldsymbol{B}$. Thus, the presence of the last term in the derivative makes the free energy density (3.1) non-invariant under the parity inversion: $P(\mathcal{F}) = \mathcal{F} - 2ek(\varkappa_+ + \varkappa_-)\boldsymbol{B} \cdot \mathrm{Im}(\psi^* \boldsymbol{D}\psi)$.

The physical length scales of the theory, namely the coherence length ξ and London penetration depth λ_L, are determined by the coefficients of the Ginzburg-Landau model as

$$\begin{aligned} \lambda_L &= \lambda_0 \sqrt{1 + \frac{\varkappa_+^2 + \varkappa_-^2}{2\lambda_0^2}}, \quad \text{where} \quad \lambda_0^2 = \frac{1}{8\pi k e^2 \psi_0^2}, \\ \xi^2 &= \frac{k}{2\beta\psi_0^2}, \end{aligned} \tag{3.2}$$

respectively. The Ginzburg-Landau parameter is the ratio $\kappa = \frac{\lambda_L}{\xi}$. Note that in noncentrosymmetric superconductors, an externally applied magnetic field does not decay in a simple monotonic way; for a detailed discussion how a counterpart of the London's penetration length is defined in such a case, see [57, 58]. The variation of the free energy (3.1) with respect to the field ψ^* yields the Ginzburg-Landau equation for the superconducting condensate

$$k \sum_{a=\pm} \mathcal{D}_a \mathcal{D}_a \psi = 2\beta(|\psi|^2 - \psi_0^2)\psi, \tag{3.3}$$

while the variation of the free energy with respect to the vector potential $\boldsymbol{A}$ determines the Ampère-Maxwell equation

$$\boldsymbol{\nabla} \cdot \left(\frac{\boldsymbol{B}}{4\pi} + ke \sum_{a=\pm} \varkappa_a \boldsymbol{J}_a \right) = ke \sum_{a=\pm} \boldsymbol{J}_a \tag{3.4}$$

where $\boldsymbol{J}_a = \mathrm{Im}(\psi^* \mathcal{D}_a \psi)$.

3.1.1 London-limit

The kinetic term of the free energy (3.1), can be expressed into a sum of gauge-invariant terms:

$$\frac{1}{2} \sum_{a=\pm} |\mathcal{D}_a \psi|^2 = |\boldsymbol{D}\psi|^2 + \chi \boldsymbol{j} \cdot \boldsymbol{B} + e^2(\chi^2 + \nu^2)|\psi|^2 \boldsymbol{B}^2, \tag{3.5}$$

where $\boldsymbol{D} \equiv \boldsymbol{\nabla} - ie\boldsymbol{A}$, and $\boldsymbol{j} = 2e|\psi|^2(\boldsymbol{\nabla}\varphi - e\boldsymbol{A})$.

In the London limit ($\beta \to \infty$), the superconducting density is a spatially uniform quantity, $|\psi| = \psi_0$, and the free energy reads as follows:

$$\mathcal{F}_L = k\lambda_L^2 e^2 \psi_0^2 \left(\boldsymbol{B}^2 + \hat{\boldsymbol{j}}^2 + 2\Gamma \hat{\boldsymbol{j}} \cdot \boldsymbol{B} \right) , \tag{3.6}$$

where $\hat{\boldsymbol{j}} = \dfrac{\boldsymbol{j}}{2\lambda_L e^2 \psi_0^2}$, $\Gamma = \dfrac{\chi}{\lambda_L}$, and $0 \leqslant \Gamma \leqslant 1$.

Importantly, the dimensionless parameter Γ quantifies the importance of the parity breaking. At $\Gamma = 0$, the material is thus centrosymmetric. The second London equation that relates the magnetic field $\boldsymbol{B}$ and the current $\boldsymbol{j} = 2e|\psi|^2(\boldsymbol{\nabla}\varphi - e\boldsymbol{A})$ takes the following form:

$$\boldsymbol{B} = \Phi_0 \boldsymbol{v} - \tilde{\boldsymbol{\nabla}} \times \hat{\boldsymbol{j}}. \tag{3.7}$$

Here $\boldsymbol{v} = \frac{1}{2\pi} \boldsymbol{\nabla} \times \boldsymbol{\nabla}\varphi$ is the density of vortex field that accounts for the phase singularities, and $\Phi_0 = \frac{2\pi}{e}$ is the superconducting flux quantum. In the dimensionless units used here $\tilde{\boldsymbol{x}} = \boldsymbol{x}/\lambda_L$ and $\tilde{\boldsymbol{\nabla}} = \lambda_L \boldsymbol{\nabla}$, the Ampère-Maxwell equation (3.4) reads as:

$$\tilde{\boldsymbol{\nabla}} \times \boldsymbol{H} = \tilde{\boldsymbol{\nabla}} \times (\boldsymbol{B} - 4\pi \boldsymbol{M}) = \hat{\boldsymbol{J}}, \tag{3.8}$$

where $\boldsymbol{H} = \boldsymbol{B} + \Gamma \hat{\boldsymbol{j}}$, $\hat{\boldsymbol{J}} = \hat{\boldsymbol{j}} + \Gamma \boldsymbol{B}$, and $\boldsymbol{M} = -\dfrac{\Gamma \hat{\boldsymbol{j}}}{4\pi}$, are, respectively, the (dimensionless) magnetic field, the total current and the magnetization. Introducing the complex quantity $\eta = \Gamma + i\sqrt{1 - \Gamma^2}$, the free energy density (3.6) in the London limit can further be rewritten as

$$\tilde{\mathcal{F}}_L \equiv \frac{\mathcal{F}_L}{k\lambda_L^2 e^2 \psi_0^2} = \left(\boldsymbol{B} + \eta \hat{\boldsymbol{j}} \right) \cdot \left(\boldsymbol{B} + \eta^* \hat{\boldsymbol{j}} \right) , \tag{3.9}$$

The constant density approximation, together with the expression for the magnetic field (3.7), thus yields the dimensionless free energy:

$$\tilde{\mathcal{F}}_L = \left(\boldsymbol{\mathcal{L}}^* \hat{\boldsymbol{j}} - \Phi_0 \boldsymbol{v} \right) \cdot \left(\boldsymbol{\mathcal{L}} \hat{\boldsymbol{j}} - \Phi_0 \boldsymbol{v} \right) \tag{3.10}$$

Here, for a shorthand notation, we introduce the new operator:

$$\boldsymbol{\mathcal{L}} \hat{\boldsymbol{j}} \equiv \tilde{\boldsymbol{\nabla}} \times \hat{\boldsymbol{j}} - \eta \hat{\boldsymbol{j}}.$$

The London equation for the current $\hat{\boldsymbol{j}}$, obtained as the Euler - Lagrange equation by varying the free energy (3.10) with respect to $\hat{\boldsymbol{j}}$, reads as

$$\boldsymbol{\mathcal{L}} \boldsymbol{\mathcal{L}}^* \hat{\boldsymbol{j}} = \Phi_0 \mathrm{Re}[\boldsymbol{\mathcal{L}}^* \boldsymbol{v}] \tag{3.11}$$

Note that, the source field $\boldsymbol{v}$ is not a regular function but a distribution which is zero almost everywhere, except for a set of phase singularities identified with positions of

vortices. Since we are interested in vortex free configurations, the source term associated with the vortex fields is, from now on, set to zero $\boldsymbol{v} = 0$. As we demonstrate below, the London equation (3.11) can be seen as a complex, force-free equation whose solution corresponds to the eigenfunctions of the curl operator with complex eigenvalues. The general axisymmetric eigenfunctions of the curl operator can, for example, be found by using the Chandrasekhar-Kendall toroidal-poloidal decomposition [42, 95]. Below, we will express the solutions differently, using the basis of vector spherical harmonics.

3.1.2 Derivation of a general solution via vector spherical harmonics

We are interested in finding the spatially localized solutions of the London equation (3.11). This equation can be simplified by introducing a complex, force-free vector field $\boldsymbol{\mathcal{Q}}$ that satisfies the force-free equation:

$$\boldsymbol{\mathcal{L}}\boldsymbol{\mathcal{Q}} = 0\,. \tag{3.12}$$

Hence, in the absence of a source term, the London equation implies that

$$\boldsymbol{\mathcal{L}}^*\hat{\boldsymbol{j}} = i\mathrm{Im}(\eta)\boldsymbol{\mathcal{Q}}\,, \tag{3.13}$$

where $\boldsymbol{\mathcal{Q}}$ obeys the force-free equation (3.12). This definition relates the physical magnetic fields and the electric current to the force-free field $\boldsymbol{\mathcal{Q}}$ as

$$\hat{\boldsymbol{j}} = \mathrm{Re}(\boldsymbol{\mathcal{Q}}), \qquad \hat{\boldsymbol{J}} = \sqrt{1-\Gamma^2}\,\mathrm{Im}(\eta\boldsymbol{\mathcal{Q}})\,, \tag{3.14a}$$

$$\boldsymbol{B} = -\mathrm{Re}(\eta\boldsymbol{\mathcal{Q}}), \quad \boldsymbol{H} = \sqrt{1-\Gamma^2}\,\mathrm{Im}(\boldsymbol{\mathcal{Q}})\,. \tag{3.14b}$$

In exactly the same way as in the chapter 2, it is convinient to represent the solutions $\boldsymbol{\mathcal{Q}}$ of the force-free equation (3.12) in basis of the vector spherical harmonics[92], which provides a convenient separation of the radial and angular variables. The force-free $\boldsymbol{\mathcal{Q}}$, as well as the other fields, are thus decomposed as follows:

$$\boldsymbol{\mathcal{Q}}(\boldsymbol{r}) = \sum_{l=0}^{\infty}\sum_{m=-l}^{l}\left(\sum_{\boldsymbol{Z}=\boldsymbol{Y},\boldsymbol{\Psi},\boldsymbol{\Phi}} Q^{\boldsymbol{Z}}_{lm}(r)\,\boldsymbol{Z}_{lm}(\hat{\boldsymbol{r}})\right), \tag{3.15}$$

where $\boldsymbol{Z}_{lm} = (\boldsymbol{Y}_{lm}, \boldsymbol{\Psi}_{lm}, \boldsymbol{\Phi}_{lm})$ (the three orthogonal vector spherical harmonics) and the corresponding radial functions $Q^{\boldsymbol{Z}}_{lm}(r)$ are labeled by by the integer-valued quantum number of the angular momentum $l = 0, 1, 2, \ldots$ and its projection on the z axis, $m \equiv m_z \in \mathbb{Z}$ with $-l \leqslant m \leqslant l$. The angular coordinate are encoded in the unit vector $\hat{\boldsymbol{r}} \equiv \boldsymbol{r}/r$. The vector spherical harmonics $\boldsymbol{Z}_{lm}$ are defined, in the parametrization of

Ref. [92], via their scalar counterpart $Y_{lm}(\hat{\boldsymbol{r}})$ as:

$$\boldsymbol{Y}_{lm}(\hat{\boldsymbol{r}}) = Y_{lm}(\hat{\boldsymbol{r}})\hat{\boldsymbol{r}}\,, \tag{3.16a}$$

$$\boldsymbol{\Psi}_{lm}(\hat{\boldsymbol{r}}) = r\boldsymbol{\nabla}Y_{lm}(\hat{\boldsymbol{r}})\,, \tag{3.16b}$$

$$\boldsymbol{\Phi}_{lm}(\hat{\boldsymbol{r}}) = \boldsymbol{r}\times\boldsymbol{\nabla}Y_{lm}(\hat{\boldsymbol{r}})\,, \tag{3.16c}$$

See the A for the details on the definitions and properties of the vector spherical harmonics.

Given the decomposition (3.15), the force-free equation (3.12) determines a system of three differential equations:

$$-\frac{l(l+1)}{r}Q^{\boldsymbol{\Phi}}_{lm} - \eta Q^{\boldsymbol{Y}}_{lm} = 0\,, \tag{3.17a}$$

$$-\frac{1}{r}\frac{d}{dr}\big(rQ^{\boldsymbol{\Phi}}_{lm}\big) - \eta Q^{\boldsymbol{\Psi}}_{lm} = 0\,, \tag{3.17b}$$

$$\frac{1}{r}\frac{d}{dr}\big(rQ^{\boldsymbol{\Psi}}_{lm}\big) - \frac{1}{r}Q^{\boldsymbol{Y}}_{lm} - \eta Q^{\boldsymbol{\Phi}}_{lm} = 0\,, \tag{3.17c}$$

which, combined together, yields:

$$Q^{\boldsymbol{Y}}_{lm} = -\frac{l(l+1)}{\eta r}Q^{\boldsymbol{\Phi}}_{lm}\,, \tag{3.18a}$$

$$Q^{\boldsymbol{\Psi}}_{lm} = -\frac{1}{\eta r}\frac{d}{dr}\big(rQ^{\boldsymbol{\Phi}}_{lm}\big)\,, \tag{3.18b}$$

$$\left[\frac{1}{r^2}\frac{d}{dr}\left(r^2\frac{d}{dr}\right) - \frac{l(l+1)}{r^2} + \eta^2\right]Q^{\boldsymbol{\Phi}}_{lm} = 0\,. \tag{3.18c}$$

The equation (3.18c) on $Q^{\boldsymbol{\Phi}}_{lm}$ is the spherical Bessel equation whose general solution is the superposition of two spherical Hankel functions

$$Q^{\boldsymbol{\Phi}}_{lm} = c_{lm}h^{(1)}_l(\eta r) + d_{lm}h^{(2)}_l(\eta r). \tag{3.19}$$

Here, $h^{(1)}_l$ and $h^{(2)}_l$ are respectively the spherical Hankel functions of the first and second kind.

The second spherical functions diverges at large r in the next way (B.9):

$$h^{(1)}_l(z) \sim \frac{2\pi}{z}\exp\left[+i\left(z - \frac{(l+1)\pi}{2}\right)\right], \tag{3.20a}$$

$$h^{(2)}_l(z) \sim \frac{2\pi}{z}\exp\left[-i\left(z - \frac{(l+1)\pi}{2}\right)\right], \tag{3.20b}$$

By definition, $\eta = \Gamma + i\sqrt{1-\Gamma^2}$ with $\Gamma \in [0;1]$, so that $0 < \arg(\eta r) < \pi$ and thus

$$h^{(1)}_l(\eta r) \sim \frac{2\pi(-i)^{l+1}}{\eta r}e^{+i\Gamma r}e^{-\sqrt{1-\Gamma^2}r}\,, \tag{3.21a}$$

$$h^{(2)}_l(\eta r) \sim \frac{2\pi(+i)^{l+1}}{\eta r}e^{-i\Gamma r}e^{+\sqrt{1-\Gamma^2}r}\,. \tag{3.21b}$$

It follows that for the solutions (3.19) to be bounded at infinity, we must have $d_{lm} = 0$, and thus

$$Q^{\mathbf{\Phi}}_{lm} = c_{lm} h^{(1)}_l(\eta r)\,. \tag{3.22}$$

Finally, given the defining relations((3.18a), (3.18b)) the asymptotic finite components of the force-free field, associated with the different vector spherical harmonics are

$$\begin{aligned} Q^{\boldsymbol{Y}}_{lm} &= -c_{lm}\frac{l(l+1)}{\eta r} h^{(1)}_l(\eta r)\,, \quad Q^{\mathbf{\Phi}}_{lm} = c_{lm} h^{(1)}_l(\eta r), \\ Q^{\mathbf{\Psi}}_{lm} &= -c_{lm}\left(\frac{l+1}{\eta r} h^{(1)}_l(\eta r) - h^{(1)}_{l+1}(\eta r)\right)\,. \end{aligned} \tag{3.23}$$

Here c_{lm} is an arbitratry complex constant. Using the relations between the physical fields and the force-free field (3.14), the total London free energy (3.10) can be written in the basis of the vector spherical harmonics as:

$$\tilde{F} = (1-\Gamma^2)\sum_{l=0}^{\infty}\sum_{m=-l}^{l}\int_0^{\infty} r^2 dr \sum_{\boldsymbol{Z}=\boldsymbol{Y},\mathbf{\Psi},\mathbf{\Phi}} \omega^{\boldsymbol{Z}}_{lm} |Q^{\boldsymbol{Z}}_{lm}|^2\,, \tag{3.24}$$

where $\omega^{\boldsymbol{Y}}_{lm} = 1$ and $\omega^{\mathbf{\Psi}}_{lm} = \omega^{\mathbf{\Phi}}_{lm} = l(l+1)$. Here, the angular degrees of freedom have been integrated out using the orthogonality properties of the spherical harmonics (see Appendix A). Note that the dimensionless energy (3.24) is related to the total free-energy as $F = k\lambda_L^5 e^2 \psi_0^2 \tilde{F}$.

According to the definition of the free energy (3.6), in the absence of phase gradients, the gauge field $\boldsymbol{A}$ is related to the dimensionless current $\hat{\boldsymbol{j}}$ as $\boldsymbol{A} = -\lambda_L \hat{\boldsymbol{j}}$. Thus, the dimensionless helicity (2.74) reads as: $\tilde{\mathcal{H}} \equiv \mathcal{H}/\lambda_L = -\int \hat{\boldsymbol{j}} \cdot \boldsymbol{B}$. Here again, given the relations (3.14) between the physical fields and the force-free field $\boldsymbol{\mathcal{Q}}$, the dimensionless helicity takes the following form:

$$\mathcal{H} = \int \mathrm{Re}(\boldsymbol{\mathcal{Q}}) \cdot \mathrm{Re}(\eta \boldsymbol{\mathcal{Q}}) = \sum_{l,m} \int r^2 dr \mathcal{H}_{lm}, \tag{3.25}$$

where

$$\mathcal{H}_{lm} = \sum_{\boldsymbol{Z}=\boldsymbol{Y},\mathbf{\Psi},\mathbf{\Phi}} \omega^{\boldsymbol{Z}}_{lm} \begin{cases} \mathrm{Re}(\eta Q^{\boldsymbol{Z}}_{lm})\mathrm{Re}(Q^{\boldsymbol{Z}}_{lm}), & \text{if } m \text{ is even}\,, \\ \mathrm{Im}(\eta Q^{\boldsymbol{Z}}_{lm})\mathrm{Im}(Q^{\boldsymbol{Z}}_{lm}), & \text{if } m \text{ is odd}\,. \end{cases}$$

Knowing the behavior of the Hankel function with a small argument (B.10), we can obtain the leading contribution of the different components of the force-free field at small r:

$$Q^{\boldsymbol{Y}}_{lm} = c_{lm}\frac{i2^l l(l+1)\Gamma(l+1/2)}{\sqrt{\pi}(\eta r)^{l+2}}\,, \tag{3.26a}$$

$$Q^{\mathbf{\Psi}}_{lm} = -c_{lm}\frac{i2^l l\Gamma(l+1/2)}{\sqrt{\pi}(\eta r)^{l+2}}\,, \tag{3.26b}$$

$$Q^{\mathbf{\Phi}}_{lm} = -c_{lm}\frac{i2^l \Gamma(l+1/2)}{\sqrt{\pi}(\eta r)^{l+1}}\,, \tag{3.26c}$$

where $\Gamma(z)$ is the Gamma function (not to be confused with the dimensionless parameter Γ). Thus, at small radius r, all the components of the force - free field (3.23) diverges as:

$$Q^{\boldsymbol{Y}} \sim r^{-(l+2)}, \quad Q^{\boldsymbol{\Psi}} \sim r^{-(l+2)}, \quad Q^{\boldsymbol{\Phi}} \sim r^{-(l+1)}. \tag{3.27}$$

Therefore, all the toroflux modes, in the London limit, have an intrinsic divergence at the origin, and, then they require regularization, or a cut-off, at the core of the solutions. For example, the divergence of the $l = 1$ solution behaves as a point-like magnetic dipole which, in realistic circumstances, can be regularized by the size of a ferromagnetic (spherical) inclusion that represents a physical dipole. The same statement can also be applied to the other, quadrupole ($l = 2$) and higher modes.

The conventional vortices, in the London limit, are known to have a similar divergence, which is resolved by introducing a cut-off at a short distance from the vortex center. Introducing such a cut-off is relevant because vortices have a nonzero phase winding, and consequently, the complex field of the condensate must vanish somewhere. However, these arguments cannot be applied to the case of the toroflux for the simple reason that the source term associated with the vortex fields is set to zero, $\boldsymbol{v} = 0$ (see the discussion after Eq. (3.11)). Therefore, no topological arguments demand vanishing the superconducting density, leading to a breakdown of the London limit that further requires the introduction of an ultraviolet cutoff. Below we consider a general case of a magnetized inclusion which naturally regularizes the divergence of the toroflux modes (3.27).

3.2 Magnetized inclusion

In order to account for the divergences of the force-free field, it is instructive to consider the case of a magnetized inclusion in the bulk of the noncentrosymmetric material. For simplicity, we study a spherical inclusion of radius r_0, as it is schematically illustrated in Fig. 3.1. Inside a magnetized medium, the constituent magnetostatics equations are:

$$\tilde{\boldsymbol{\nabla}} \times \boldsymbol{H} = 0, \ \tilde{\boldsymbol{\nabla}} \cdot \boldsymbol{B} = 0, \tag{3.28}$$

where $\boldsymbol{B} = \boldsymbol{H} + 4\pi \boldsymbol{M}$.

The fields of the magnetized spherical inclusion are constructed following the standard textbook calculations, see e.g. [96]. To this end, we introduce the magnetic scalar potential ω_M which describe the magnetic field $\boldsymbol{H} = -\tilde{\boldsymbol{\nabla}}\omega_M$, and decompose the magnetic potential over the scalar spherical harmonics by using multipole expansion of ω_M:

$$\omega_M(\boldsymbol{r}) = \sum_{l=0}^{\infty} \sum_{m=-l}^{l} \omega_{lm}(r) Y_{lm}(\hat{\boldsymbol{r}}), \tag{3.29}$$

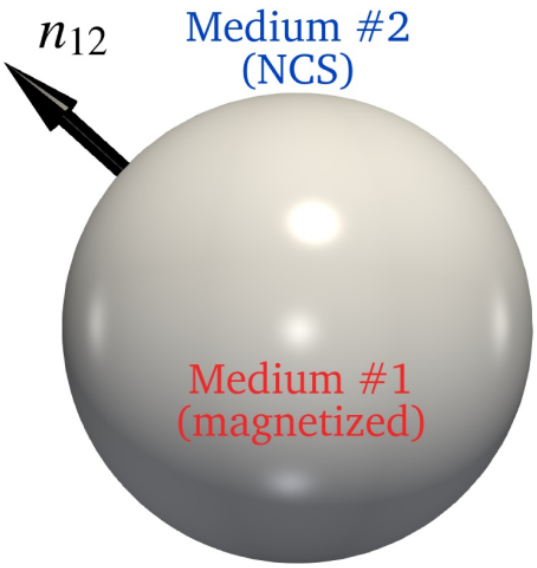

Figure 3.1: Schematic representation of a spherical magnetized medium (#1) of radius r0 and the noncentrosymmetric superconducting medium (#2). The unit vector $\boldsymbol{n}_{12}$ is the normal vector at the interface between these media.

in order to get the field $\boldsymbol{H}$ in terms of spherical harmonics (A.9):

$$\boldsymbol{H} = -\sum_{l=0}^{\infty}\sum_{m=-l}^{l}\left(\frac{d\omega_{lm}}{dr}\boldsymbol{Y}_{lm} + \frac{\omega_{lm}}{r}\boldsymbol{\Psi}_{lm}\right). \tag{3.30}$$

The relation $\tilde{\boldsymbol{\nabla}}\cdot\boldsymbol{H} = 0$, which reflects the closeness of the lines of the field $\boldsymbol{H}$, give us equation on $\omega_{lm}(r)$:

$$\left[\frac{d^2}{dr^2} + 2r\frac{d}{dr} - l(l+1)\right]\omega_{lm} = 0. \tag{3.31}$$

This determines the magnetic potential associated with the magnetized inclusion:

$$\omega_{lm} = \begin{cases} \check{c}_{lm}r^{l}\,, & \text{if } r < r_0\,, \\ \check{d}_{lm}r^{-(l+1)}\,, & \text{if } r > r_0\,. \end{cases} \tag{3.32}$$

Hereafter, the symbol $\check{}$ marks the quamtities inside the spherical inclusion.

The continuity of the magnetic potential at the boundary $r = r_0$ implies that $\check{d}_{lm} = \check{c}_{lm}r_0^{2l+1}$. The normal derivative of the magnetic potential is discontinuous across the interface. Therefore, the relation $\boldsymbol{\nabla}\cdot\big(\boldsymbol{H} + 4\pi\boldsymbol{M}\big) = 0$ implies that, at $r = r_0$,

$$\frac{d\omega_{lm}^{\text{in}}}{dr} - \frac{d\omega_{lm}^{\text{out}}}{dr} = 4\pi\check{\boldsymbol{M}}_{lm}^{\boldsymbol{Y}} \quad\Rightarrow\quad \check{c}_{lm} = \frac{4\pi\check{\boldsymbol{M}}_{lm}^{\boldsymbol{Y}}}{(2l+1)r_0^{l-1}}. \tag{3.33}$$

Here, $\check{\boldsymbol{M}}_{lm}^{\boldsymbol{Y}}$ is the $\boldsymbol{Y}$-component of the magnetization $\check{\boldsymbol{M}}$, decomposed (as well as the magnetic field $\boldsymbol{B}$) onto the vector spherical harmonics, similarly to the force-free field $\boldsymbol{\mathcal{Q}}$ (3.15). Hence, the general solutions are constrained by the requirement that the

magnetic field should be a real-valued quantity, while the magnetic fields $\check{\boldsymbol{B}}$ and $\check{\boldsymbol{H}}$ inside the magnetized spherical inclusion of radius r_0 satisfy the following relations:

$$\check{H}^{\boldsymbol{Y}}_{lm} = \check{H}^{\boldsymbol{\Psi}}_{lm} = -\frac{4\pi l \check{\boldsymbol{M}}^{\boldsymbol{Y}}_{lm}}{2l+1}\left(\frac{r}{r_0}\right)^{l-1}, \quad \check{H}^{\boldsymbol{\Phi}}_{lm} = 0\,, \tag{3.34a}$$

$$\check{\boldsymbol{B}}^{\boldsymbol{Z}}_{lm} = \check{H}^{\boldsymbol{Z}}_{lm} + 4\pi \check{\boldsymbol{M}}^{\boldsymbol{Z}}_{lm}, \tag{3.34b}$$

with $\boldsymbol{Z} = \boldsymbol{Y}, \boldsymbol{\Psi}, \boldsymbol{\Phi}$. As detailed below, the interface boundary conditions between the magnetized inclusion and the superconductor allow to relate the values of the parameters c_{lm} between both media.

Matching conditions at the interface

The continuity conditions for the current and the magnetic fields at the interface between a magnetized inclusion inside a superconducting medium read as:

$$0 = \boldsymbol{J}\cdot\boldsymbol{n}_{12}\big|_{r=r_0}\,, \tag{3.35a}$$

$$0 = \boldsymbol{n}_{12}\cdot\left(\boldsymbol{B}_2-\boldsymbol{B}_1\right)\big|_{r=r_0}\,, \tag{3.35b}$$

$$\boldsymbol{J}_S = \boldsymbol{n}_{12}\times\left(\boldsymbol{H}_2-\boldsymbol{H}_1\right)\big|_{r=r_0}\,. \tag{3.35c}$$

Here, $\boldsymbol{n}_{12}$ is the normal vector from medium 1 (the magnetized inclusion) to the medium 2 (the parity-odd superconductor) and $\boldsymbol{J}_S$ is the surface current density which is localized at the interface.

The first equation in (3.35) represents the requirement of the absence of a flow of superconducting current $\boldsymbol{J}$ through the interface between the superconductor and the magnetized inclusion [91]. Consequently, the normal component of $\boldsymbol{J}$ vanishes at the interface between these media. Given the decomposition (3.15) of the solution voer the vector spherical harmonics, and since $\boldsymbol{Y}_{lm}$ is the only vector harmonic that has a radial component, the first two relations in Eq. (3.35) reduce to:

$$\boldsymbol{J}\cdot\boldsymbol{n}_{12}\big|_{r=r_0} = \sqrt{1-\Gamma^2}\sum_{l,m}\mathrm{Im}(\eta Q^{\boldsymbol{Y}}_{lm}Y_{lm}) = 0\,, \tag{3.36a}$$

$$(\boldsymbol{B}-\check{\boldsymbol{B}})\big|_{r=r_0} = -\sum_{l,m}\mathrm{Re}\Big((\eta Q^{\boldsymbol{Y}}_{lm}+\check{\boldsymbol{B}}^{\boldsymbol{Y}}_{lm})Y_{lm}\Big) = 0\,. \tag{3.36b}$$

Note that the intrinsic degrees of freedom of the solutions of these equations always allows to reconstruct the real valued magnetic field (3.34) inside the inclusion. In other words, it is always possible to construct the field $\check{\boldsymbol{B}}$ such that $\mathrm{Im}\check{\boldsymbol{B}} = 0$. Hence, the interface conditions (3.35), for a given (l,m) mode, boil down to

$$(\eta Q^{\boldsymbol{Y}}_{lm}+\check{\boldsymbol{B}}^{\boldsymbol{Y}}_{lm}) = 0. \tag{3.37}$$

Now, we use of the explicit form of the radial modes (3.23) to fix all the coefficients c_{lm} of the solution:

$$c_{lm} = \frac{r_0 \check{\boldsymbol{B}}^{\boldsymbol{Y}}_{lm}(r_0)}{l(l+1)h_l^{(1)}(\eta r_0)}, \text{for } l > 0. \tag{3.38}$$

Finally, given the (l, m) magnetization modes for the fields inside the magnetized spherical inclusion (3.34), the arbitrary coefficients c_{lm} reads as:

$$c_{lm} = \frac{4\pi r_0 M^{\boldsymbol{Y}}_{lm}(r_0)}{l(2l+1)h_l^{(1)}(\eta r)}, \text{for } l > 0. \tag{3.39}$$

Thus, we obtain the most general solution for a spherical inclusion with arbitrary magnetization.

3.2.1 Explicit forms of the toroflux induced by a magnetic dipole

Consider now the particular case of a spherical impurity of the radius r_0, which possesses the magnetic dipole moment $\check{\boldsymbol{M}}$ directed along the axis $\hat{\boldsymbol{z}}$, and with all higher-order modes vanishing. In spherical coordinates, the magnetic moment reads as follows:

$$\check{\boldsymbol{M}} = M_0 \hat{\boldsymbol{z}} = M_0 \left(\hat{\boldsymbol{r}} \cos\theta - \hat{\boldsymbol{\theta}} \sin\theta \right) = \sqrt{\frac{4\pi}{3}} M_0 (\boldsymbol{Y}_{10} + \boldsymbol{\Psi}_{10}). \tag{3.40}$$

Thus, the magnetic fields (3.34) inside the inclusion are

$$\check{H}^{\boldsymbol{Y}}_{10} = \check{H}^{\boldsymbol{\Psi}}_{10} = -\left(\frac{4\pi}{3}\right)^{3/2} M_0\,, \quad \check{H}^{\boldsymbol{\Phi}}_{10} = 0\,, \tag{3.41a}$$

$$\check{B}^{\boldsymbol{Y}}_{10} = \check{B}^{\boldsymbol{\Psi}}_{10} = 2\left(\frac{4\pi}{3}\right)^{3/2} M_0\,, \quad \check{B}^{\boldsymbol{\Phi}}_{10} = 0, \tag{3.41b}$$

The continuity conditions (3.39) fix the only nonzero coefficient c_{10} of the force-free field $\boldsymbol{\mathcal{Q}}$ (3.23):

$$c_{10} = \frac{r_0 M_0}{h_1^{(1)}(\eta r_0)} \left(\frac{4\pi}{3}\right)^{3/2} \tag{3.42}$$

The behaviour of the Hankel functions for small arguments (B.10) implies that:

$$c_{10} = i\sqrt{\frac{4\pi}{3}} \left(\frac{4\pi r_0^3}{3}\right)^{3/2} M_0 \eta^2\,, \text{when } r_0 \to 0\,. \tag{3.43}$$

Thus, for a point-like dipole with the magnetic moment

$$M_0^d = \frac{4\pi}{3} r_0^3 M_0\,, \tag{3.44}$$

where the quantity M_0 is the density of the magnetic moment in the impurity calculated per unit volume, the coefficient c_{10} is uniquely determined as

$$c_{10} = i\sqrt{\frac{4\pi}{3}}\eta^2 M_0^d. \tag{3.45}$$

Now, given the coefficient (3.45), the magnetic field $\boldsymbol{H}$ and the current $\boldsymbol{J}$ induced by a magnetic pointlike dipole can be reconstructed from the force-free field $\boldsymbol{\mathcal{Q}}$ according to (3.14). The components of the force-free field $\boldsymbol{\mathcal{Q}}$ corresponding to a given sector of the vector spherical harmonics are defined in therms of the spherical Hankel functions of the first kind (3.23). These functions can further be expressed in a closed form using the relation (B.8a). Finally, the vector harmonics of a dipolar source possess the single mode $(l, m) = (1, 0)$ which have the simple form (A.16). Thus, in terms of elementary functions, the related force-free field $\boldsymbol{\mathcal{Q}}_{10}$ induced by a magnetic dipole reads as

$$\boldsymbol{\mathcal{Q}}_{10} = -M_0^d \frac{e^{i\eta r}}{\eta r^3}\Big[(1-i\eta r)\big(2\cos\theta\hat{\boldsymbol{r}} + \eta r\sin\theta\hat{\boldsymbol{\phi}}\big) + \big(1-i\eta r(1-i\eta r)\big)\sin\theta\hat{\boldsymbol{\theta}}\Big]. \tag{3.46}$$

The complex parameter η depends on the parity breaking parameter $0 < \Gamma < 1$ as $\eta = \Gamma + i\sqrt{1-\Gamma^2}$. Thus all the fields are exponentially localised as $e^{-r\sqrt{1-\Gamma^2}}$. Hence, the size of the torofluxes,

$$L_{\rm tor} = \frac{\lambda_L}{\sqrt{1-\Gamma^2}}, \tag{3.47}$$

is determined by the London penetration length λ_L and the dimensionless parity breaking coupling Γ defined in Eq.(3.6). In the limit of the maximal parity violation, $\Gamma \to 1$, the size of the toroflux diverges.

As a result, the physical fields $\boldsymbol{H}$ and $\boldsymbol{J}$ can be reconstructed from the force-free field $\boldsymbol{\mathcal{Q}}_{10}$ (3.46) by using the relations (3.14):

$$\begin{aligned}
\boldsymbol{H} &= M_0^d e^{-r\sqrt{1-\Gamma^2}}\left\{\frac{2\cos\theta}{r^3}\left[\left(\sqrt{1-\Gamma^2}+r\right)\cos\Gamma r - \Gamma\sin\Gamma r\right]\hat{\boldsymbol{r}}\right. \qquad (3.48a)\\
&+\frac{\sin\theta}{r^3}\left[\left((1+r^2)\sqrt{1-\Gamma^2}+r\right)\cos\Gamma r + \Gamma(r^2-1)\sin\Gamma r\right]\hat{\boldsymbol{\theta}}\\
&\left.+\frac{\sin\theta}{r^2}\left[\Gamma r\cos\Gamma r - \left(1+r\sqrt{1-\Gamma^2}\right)\sin\Gamma r\right]\hat{\boldsymbol{\phi}}\right\},\\
\boldsymbol{J} &= M_0^d e^{-r\sqrt{1-\Gamma^2}}\left\{\frac{2\cos\theta}{r^3}\left[\Gamma r\cos\Gamma r - \left(1+r\sqrt{1-\Gamma^2}\right)\sin\Gamma r\right]\hat{\boldsymbol{r}}\right. \qquad (3.48b)\\
&+\frac{\sin\theta}{r^3}\left[\Gamma r\left(1+2r\sqrt{1-\Gamma^2}\right)\cos\Gamma r - \left(1+r\sqrt{1-\Gamma^2}+r^2(1-2\Gamma^2)\right)\sin\Gamma r\right]\hat{\boldsymbol{\theta}}\\
&\left.-\frac{\sin\theta}{r^2}\left[\Gamma\left(1+2r\sqrt{1-\Gamma^2}\right)\sin\Gamma r + \left(r(1-2\Gamma^2)+\sqrt{1-\Gamma^2}\right)\cos\Gamma r\right]\hat{\boldsymbol{\phi}}\right\}.
\end{aligned}$$

An alternative derivation via the Chandrasekhar-Kendall method is briefly outlined in the next subsection 3.2.2.

It should be stressed that our derivation of the toroflux solutions is performed in the continuum Ginzburg-Landau model (3.1) which does not incorporate the shortdistance

cutoff played by the spacing a of the underlying crystal lattice. Therefore, the validity of our whole proposal assumes that the toroflux solutions should have length scale much larger than the lattice constant a, or $r_0 \gg a/\lambda_L$. It is not difficult to satisfy this requirement because $a \ll \lambda_L$, ξ generically [91].

Yet another restriction comes from the fact that the present construction of the toroflux solutions, induced by a magnetized source in a noncentrosymmetric superconductor, is done in the London limit approximation, where the amplitude of the superconducting condensate is fixed. This implies that only the magnetic energy and kinetic energy of supercurrents are taken into account and thus assumes that there is no suppression of the order parameter. However, in the case of conventional vortices, the London approximation breaks down near the vortex core, where the kinetic and magnetic energy densities are large enough to suppress the superconducting condensate. A similar situation is expected for toroflux, where the kinetic energy density of supercurrents cannot grow indefinitely. Instead, when the sum of the kinetic and magnetic energy densities becomes comparable to condensation energy density, the modulus of the order parameter should get suppressed $|\psi(\boldsymbol{r})| < \psi_0$. This results in the formation of a core like structure where the growth of kinetic energy is limited by the depletion of the density of the order parameter.

To estimate when the London approximation breaks down, we compare the energy densities $\mathcal{F}$, Eqs. (2.1), of two possible configurations. The first configuration is $\mathcal{F}_1$, the energy density of the toroflux in the London approximation where $\psi = \psi_0$. The second configuration is $\mathcal{F}_2$, the energy of a normal state ($\psi = 0$), with the same magnetic field configuration. Hence the London approximation can be expected to break where $\mathcal{F}_1 > \mathcal{F}_2$. The energy $\mathcal{F}_2$ is thus

$$\mathcal{F}_2 = \frac{\boldsymbol{B}^2}{8\pi} + \frac{\beta\psi_0^4}{2} = \frac{(M_0^d)^2[5+3\cos(2\theta)]}{16\pi r^6} + \frac{\beta\psi_0^4}{2}\,, \tag{3.49}$$

where the magnetic field $\boldsymbol{B}$ of the toroflux solution is given by (3.46) inserted into (3.14). The energy $\mathcal{F}_1$, in the London approximation, is obtained from (3.6) [again by inserting (3.46) into (3.14)]:

$$\mathcal{F}_1 = \frac{(M_0^d)^2[5+3\cos(2\theta)]}{16\pi r^6}\left(1+\frac{\nu^2}{\lambda_0^2}\right)\,. \tag{3.50}$$

The requirement that $\mathcal{F}_1 > \mathcal{F}_2$ can be expressed as the following inequality:

$$r^6 < \frac{(M_0^d)^2\nu^2[5+3\cos(2\theta)]}{8\pi\beta\psi_0^4\lambda_0^2}\,. \tag{3.51}$$

Now, we want to ensure that our London approximation works reasonably everywhere outside the magnetic inclusion. Hence the cutoff r_c, which corresponds to the maximal possible radius r of the impurity where the London theory breaks down, is obtained from Eq. (3.51) with $\theta = 0$:

$$r_c = \left(4eM_0^d\nu\xi\right)^{1/3}\,. \tag{3.52}$$

It is interesting to note that the cutoff scale in the case of a toroflux is not simply $\propto \xi$ as for usual vortices, but is $\propto \xi^3$ with a dependence on the size and magnetization of the impurity. Then our approximation will work everywhere if $r_c < r_0$, which results in the following condition, expressed via the parameters of the model (2.4):

$$\frac{16\pi}{3}\nu\xi e M_0 < 1\,, \tag{3.53}$$

or equivalently,

$$\frac{32\pi^2 M_0 \xi \sqrt{\lambda_L^2(1-\Gamma^2)-\lambda_0^2}}{3\Phi_0} < 1\,. \tag{3.54}$$

Note that this condition can always be satisfied for sufficiently small magnetic moment M_0.

3.2.2 Outline of the Chandraseckhar-Kendall approach for a dipole source

The above section provides the explicit forms of the toroflux solutions induced by a dipole. These can alternatively be derived via the Chandrasekhar-Kendall method [42]. Consider a case when we want to find the magnetic field $\boldsymbol{B}$ that satisfies the following equation:

$$\boldsymbol{\mathcal{L}}\boldsymbol{\mathcal{L}}^*\boldsymbol{B} = c\boldsymbol{\nabla}\times\Big(\boldsymbol{\nabla}\times\boldsymbol{M}^d\Big) + d\boldsymbol{\nabla}\times\boldsymbol{M}^d\,, \tag{3.55}$$

where c and d are some real parameters and $\boldsymbol{M}^d$ is a field that corresponds to an external field induced by a magnetic moment. Then, the magnetic field $\boldsymbol{B}$ can be solved in terms of the following functions:

$$\begin{aligned} \boldsymbol{B} &= -\mathrm{Re}(\eta\boldsymbol{\mathcal{Q}})\,, && \text{(3.56a)}\\ \boldsymbol{\mathcal{Q}} &= \boldsymbol{\nabla}\times\boldsymbol{u} + \boldsymbol{\nabla}\times(\boldsymbol{\nabla}\times\boldsymbol{u})/\eta\,, && \text{(3.56b)}\\ \Delta\boldsymbol{u} + \eta^2\boldsymbol{u} &= b\boldsymbol{M}^d\,, && \text{(3.56c)} \end{aligned}$$

where $b = -i(d+c\eta)/(\mathrm{Im}\eta)$ and $\boldsymbol{u}$ is found from solving inhomogeneous vector Helmholtz equation (3.56c). The set of equations (3.56) can be verified by showing that

$$\boldsymbol{\mathcal{L}}\boldsymbol{\mathcal{Q}} = -b\boldsymbol{\nabla}\times\boldsymbol{M}^d/\eta\,, \tag{3.57}$$

which subsequently implies Eq. (3.55).

In the simplest case of pointlike dipole source $\boldsymbol{M}^d = M_0^d\hat{\boldsymbol{z}}\delta(r)$, the explicit solution of the Helmholtz equation (3.56c) is:

$$\boldsymbol{u} = -M_0^d\hat{\boldsymbol{z}}b\frac{e^{i\eta r}}{4\pi r} \tag{3.58}$$

Note, that values of c and b depend on boundary conditions that are used between magnetised and superconducting medium. The boundary conditions (3.37) are given by:

$$\left(\eta\boldsymbol{\mathcal{Q}} + \check{\boldsymbol{B}}\right) \cdot \hat{\boldsymbol{r}}\Big|_{r=r_0} = 0. \tag{3.59}$$

For $\check{\boldsymbol{B}}(r_0) = 2M_0^d\hat{\boldsymbol{z}}/r_0^3$ this results in the constants being $c = 4\pi$ and $d = -4\pi\mathrm{Re}(\eta)$ (and thus $b = 4\pi$).

Now, given the values of c and d that satisfy the appropriate boundary condition, inserting the solution (3.58) of the Helmholtz equation into the constituting equation (3.56b) yields the very same expression for the force-free field $\boldsymbol{\mathcal{Q}}$ as the explicit form of equation (3.46).

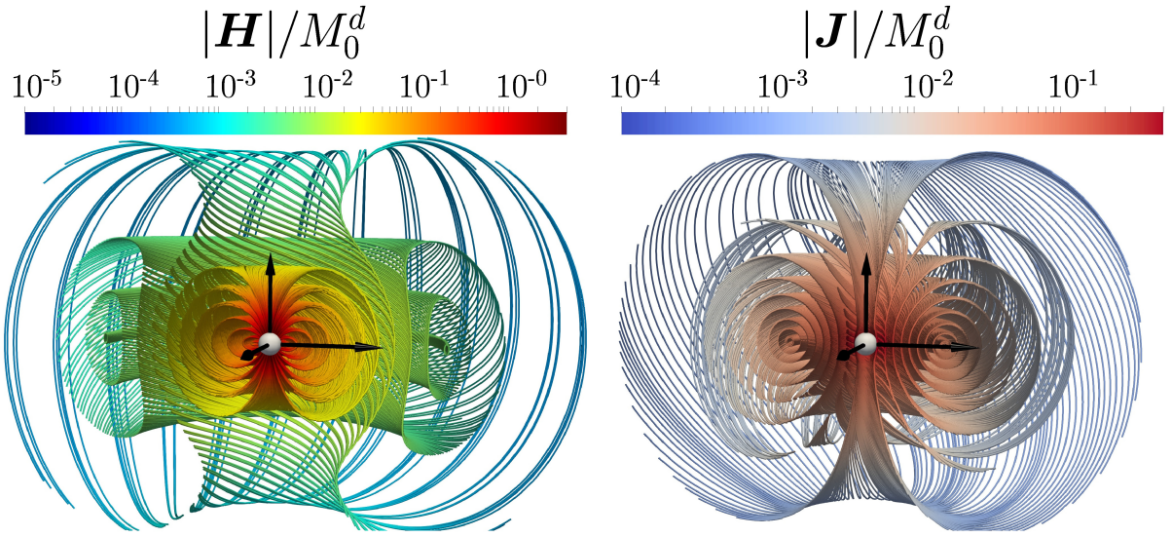

Figure 3.2: A toroflux solution induced by a magnetic dipole for the parity breaking parameter $\Gamma = 0.5$. The left panel displays the streamlines of the magnetic field $\boldsymbol{H}$, while the right panel shows the streamlines of the total electric current $\boldsymbol{J}$. These quantities are related to the other to the Ampère-Maxwell equation (3.8). The sphere in the center shows the position of the magnetized inclusion (the magnetic dipole).

3.2.3 Knotted nature of toroflux

The physical fields $\boldsymbol{H}$ and $\boldsymbol{J}$ associated with the force-free field $\boldsymbol{\mathcal{Q}}_{10}$ induced by a magnetic dipole (3.46) are displayed in the Fig. 3.2, for the value of the parity-breaking parameter $\Gamma = 0.5$. This figure illustrates that a magnetic dipole impurity induces, in a noncentrosymmetric superconductor, the knotted lines of both the magnetic field and the electric current. These toroidal, axially symmetric, nested structures, resemble in many aspects the standard Chandrasekhar-Kendall states [42]. The alternative derivation of our solutions, presented in the Section 3.2.2, highlights the proximity of the toroflux and the Chandrasekhar-Kendall states. The torofluxes are basically the

spatially localized analogues of the Chandrasekhar-Kendall states. Note that since the magnetic lines of the toroflux are closed, the total flux through any cross-section of the solution vanishes identically.

The London penetration depth determines the overall length scale the toroflux without affecting the geometry of its internal structure. On the contrary, the strength of the noncentrosymmetricity strongly affects the overall structure of the toroflux. The latter feature is illustrated in the Fig. 3.4 and 3.5, which show the streamlines of the magnetic field $\boldsymbol{H}$ and the electric current $\boldsymbol{J}$ as well as their Poincarè sections of the torofluxes for moderate ($\Gamma = 0.15$), intermediate ($\Gamma = 0.5$), and high ($\Gamma = 0.95$) values of the parity-breaking parameter Γ.

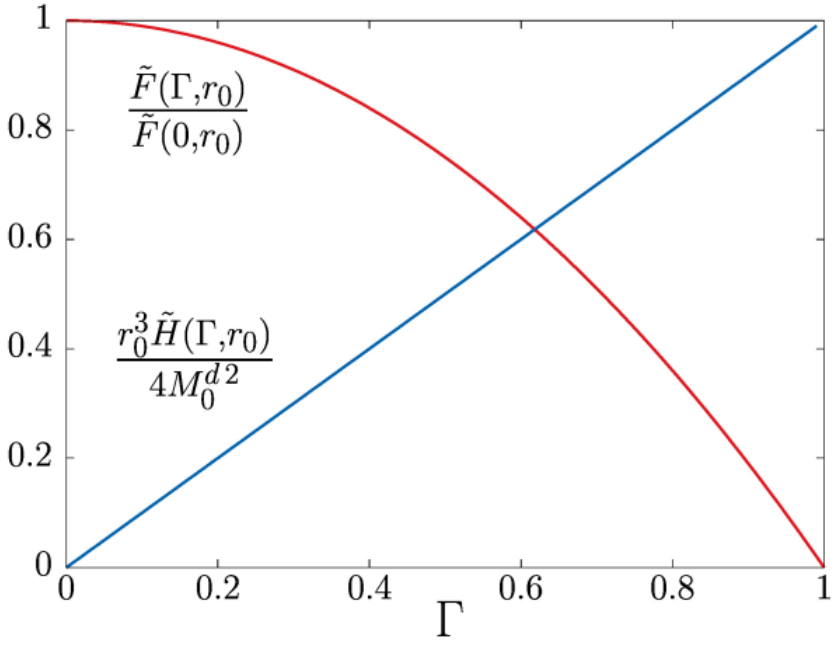

Figure 3.3: Normalized free energy $\tilde{F}$ and normalized helicity $\tilde{H}$ of the toroflux as functions of the parity breaking coupling Γ for the spherical magnetic-dipole impurity of the radius $r_0 = 10^{-2}$ (in units of λ_L).

At small parity breaking ($\Gamma = 0.15$), the magnetic field lines resembles that of a magnetic dipole. They are attached to the magnetized inclusion and slightly twisted around the axis of the dipole (and the chirality of twist depends on the sign of Γ). Accordingly, the current flows around the dipole and covers various tori. When the noncentrosymmetricity becomes more important ($\Gamma = 0.5$), the toroflux features nested tori of the magnetic lines, in addition to the twisted structure near the dipole. This property can be seen, in particular, in the $\boldsymbol{H}\big|_{x=0}$ Poincarè section in Fig. 3.4. Interestingly, the chirality of the extra nested tori is reversed compared to set of field lines that are attached to the dipole. Upon increase of the parity breaking, additional sets of nested tori appear, as can be seen field the $\boldsymbol{H}\big|_{x=0}$ Poincarè section in the Fig. 3.4 for $\Gamma = 0.95$. The fact that the number of tori with opposite chirality increases as the par-

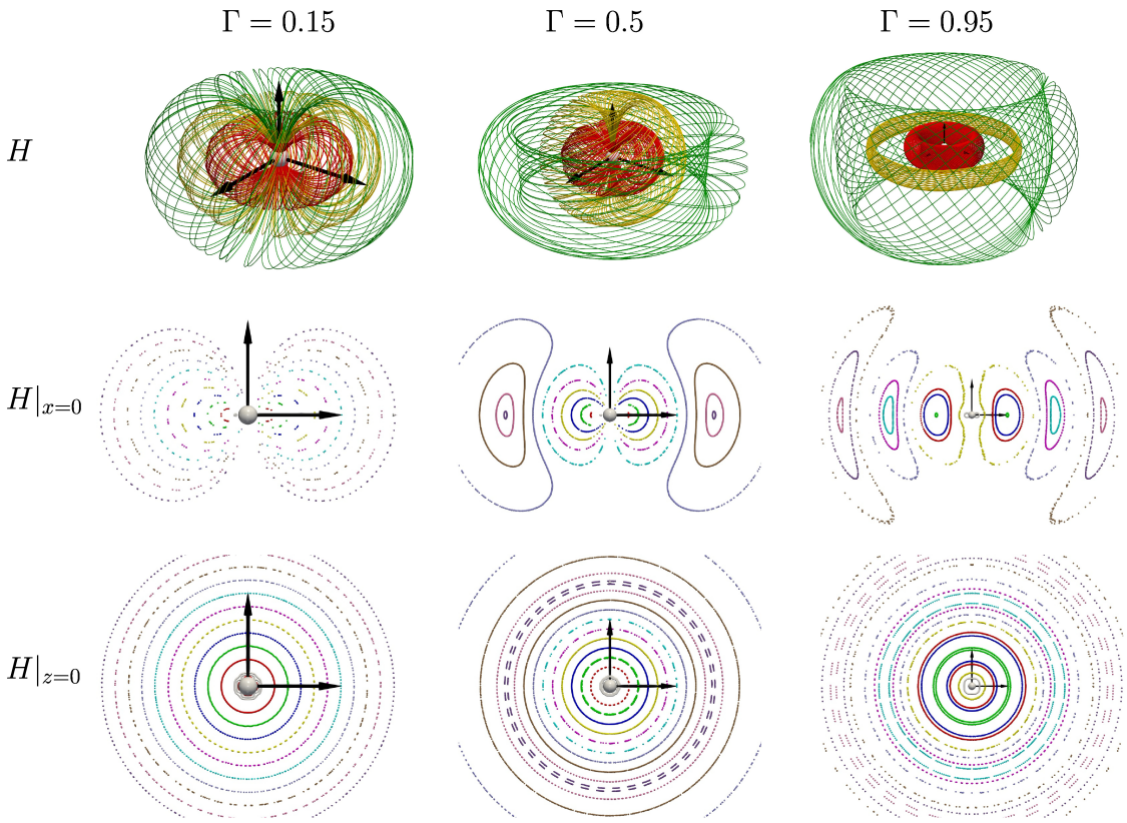

Figure 3.4: The structure of the streamlines of the magnetic field $\boldsymbol{H}$ of the toroflux solution induced by a magnetic dipole, for the values of the parity-breaking parameter $\Gamma = 0.15, 0.5,$ and 0.95. The line on the top row shows the streamlines of $\boldsymbol{H}$, and the two next rows are the Poincaré sections of the streamlines of $\boldsymbol{H}$ on the $x = 0$ and $z = 0$ planes, respectively. The central sphere depicts the spherical magnetic dipole inclusion. The relative sizes of the torofluxes can be seen from the vector basis.

ity breaking becomes stronger is qualitatively similar to the effect of the magnetic-field inversion observed near vortices at large Γ reported in Refs. [57, 58].

3.2.4 Energy and helicity of the toroflux

The dimensionless energy (3.24) of the toroflux solution (3.46) induced by a magnetic dipole depends on the parity breaking parameter Γ as:

$$\tilde{F}(\Gamma, r_0) = \frac{2(M_0^d)^2}{r_0^3} e^{-2r_0\sqrt{1-\Gamma^2}} \Big[(1+2r_0^2)(1-\Gamma^2) + \big(2(1-\Gamma^2)+r_0^2\big) r_0 \sqrt{1-\Gamma^2}\Big]. \quad (3.60)$$

The exponential prefactor contains the ratio of the inclusion radius r_0 with the size (3.47) of the toroflux, which is the consequence of the Meissner effect.

The Figure 3.3 shows the toroflux energy (3.60) as a function of the parity-breaking parameter Γ. The toroflux energy monotonically decreases as the parity breaking parameter Γ, and it is maximal in the centrosymmetric limit, $\Gamma \to 0$. This property is a consequence of the Lifshitz term $\boldsymbol{j} \cdot \boldsymbol{B}$, which provides a negative contribution when

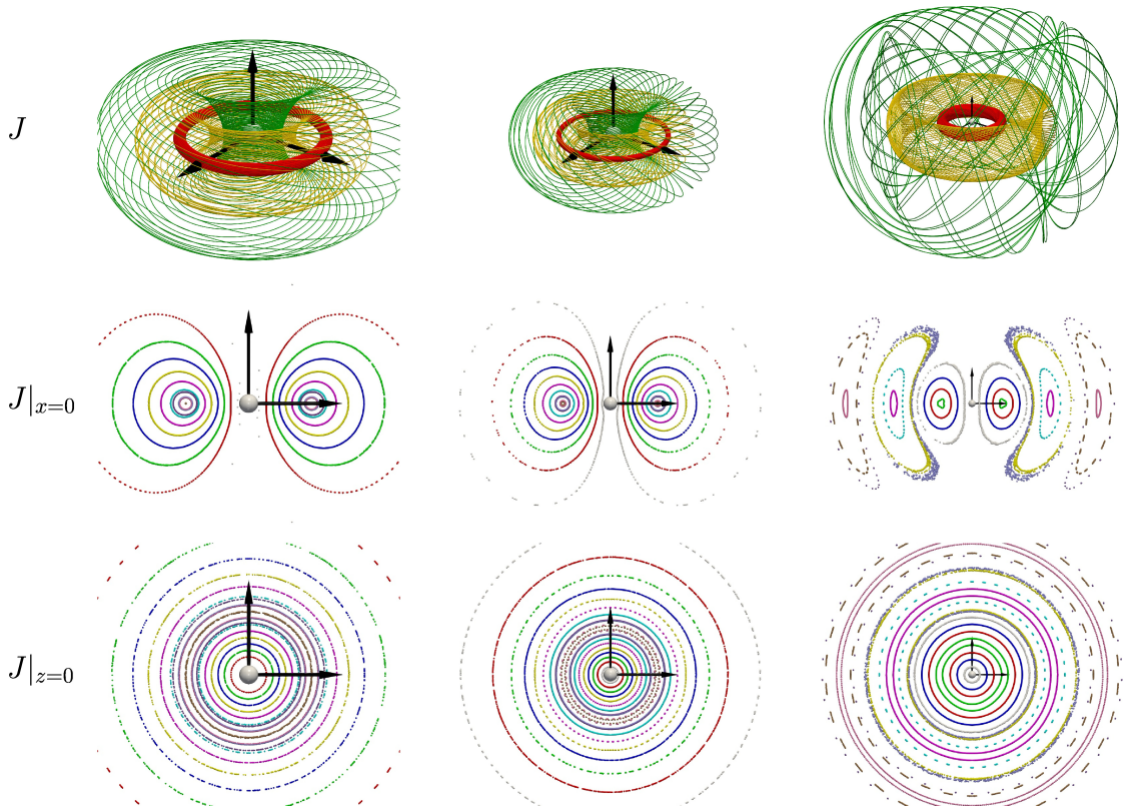

Figure 3.5: The structure of the streamlines of the electric current $\boldsymbol{J}$, of the toroflux solution induced by a magnetic dipole, for the values of the parity-breaking parameter $\Gamma = 0.15, 0.5,$ and 0.95. The line on the top row shows the streamlines of $\boldsymbol{J}$, and the two next rows are the Poincaré sections of the streamlines of $\boldsymbol{J}$ on the $x = 0$ and $z = 0$ planes, respectively. The central sphere depicts the spherical magnetic dipole inclusion. The relative sizes of the torofluxes can be seen from the vector basis.

the electric current and the magnetic field are (partially) aligned. When Γ reaches the upper bound, $\Gamma = 1$, the toroflux energy vanishes while its size (3.47) diverges. Note that unlike vortices, which carry a quantized magnetic flux, the toroflux has a zero net flux through any plane that intersects the magnetic dipole impurity. The amplitude of the magnetic field is determined only by the magnetization of the dipole, hence the energy of our toroflux solution is not quantized.

The Figure 3.3 also displays the helicity (3.25) of the toroflux (for a spherical inclusion with a small radius r_0) which, unlike the energy, monotonically grows with the increase of the parity breaking parameter Γ. As the nonlinear corrections are negligible for small inclusions, the helicity is almost a linear function of Γ. The leading contribution to the helicity at the small radius r_0 reads explicitly as follows:

$$\frac{H(\Gamma, r_0)}{2(M_0^d)^2} = \frac{2\Gamma\left(1 + r_0^2(1+\Gamma^2)\right)}{r_0^3} - 2(\Gamma^5 + 4\Gamma^3 - 3\Gamma) + \frac{8\Gamma^5 + 12\Gamma^3 - 17\Gamma}{3\sqrt{1-\Gamma^2}} + \mathcal{O}(r_0^2). \quad (3.61)$$

As previously stated, the magnetic helicity, which is associated with the topological

properties of the magnetic field lines, serves as the measure of the entanglement of knotted lines of the magnetic field $\boldsymbol{B}$.

For convenience, we finish this chapter with a short summary. We express the London equation in terms of a force-free field $\boldsymbol{\mathcal{Q}}$ (3.12), which allows us to obtain explicit solutions for all values of (l, m) (3.18). We demonstrate that a ferromagnetic inclusion regularizes the singular behavior of the solution, serving, at the same time, as a source for a finite-energy superconducting knotted solution. We further investigate the case where the inclusion is a ferromagnetic dipole (3.40). In this case the energy and the helicity are defined by expression (3.60) and (3.61). And explicit solution for current $\boldsymbol{J}$ and magnetic field $\boldsymbol{H}$ are presented in Eq. (3.48).

3.2.5 Toroidal dipole moments

Beyond the magnetic helicity, which was considered in section above, the toroflux solutions can be characterized by additional global quantities: the toroidal dipole moments. The multipole expansions are central to various areas of physics [97, 98]. A particularly insteresting kind of multipole moments are the toroidal moments, which play an important role in the electrodynamics of various condensed matter systems [97, 99, 100]. The toroidal dipole moments of the magnetic field $\boldsymbol{H}$ and the induction $\boldsymbol{B}$ are respectively defined as

$$\boldsymbol{T}^{\boldsymbol{H}} = \frac{1}{2}\int d^3\boldsymbol{r}\ \boldsymbol{r}\times\boldsymbol{H},\ \text{and}\ \boldsymbol{T}^{\boldsymbol{B}} = \frac{1}{2}\int d^3\boldsymbol{r}\ \boldsymbol{r}\times\boldsymbol{B}\,. \tag{3.62}$$

Given the relation (3.14) between the physical fields and the force-free field $\boldsymbol{\mathcal{Q}}_{10}$ (3.46) induced by a point-like dipole, the toroidal dipole moments (3.62) of the associated toroflux thus reads as

$$\boldsymbol{T}^{\boldsymbol{H}}_{10} = -\frac{1}{2}\mathrm{Re}\left[\eta\sum_{\boldsymbol{Z}=\boldsymbol{Y},\boldsymbol{\Psi},\boldsymbol{\Phi}}\int d^3\boldsymbol{r}\ Q^{\boldsymbol{Z}}_{10}(\boldsymbol{r}\times\boldsymbol{Z}_{10})\right], \tag{3.63a}$$

$$\boldsymbol{T}^{\boldsymbol{B}}_{10} = \frac{\sqrt{1-\Gamma^2}}{2}\mathrm{Im}\left[\sum_{\boldsymbol{Z}=\boldsymbol{Y},\boldsymbol{\Psi},\boldsymbol{\Phi}}\int d^3\boldsymbol{r}\ Q^{\boldsymbol{Z}}_{10}(\boldsymbol{r}\times\boldsymbol{Z}_{10})\right]. \tag{3.63b}$$

It is thus necessary to evaluate the volume integral

$$\int d^3\boldsymbol{r}\ Q^{\boldsymbol{Z}}_{10}(\boldsymbol{r}\times\boldsymbol{Z}_{10}) = \int dr\ r^3 Q^{\boldsymbol{Z}}_{10}\int d\Omega\ \hat{\boldsymbol{r}}\times\boldsymbol{Z}_{10}(\hat{\boldsymbol{r}}) \tag{3.64}$$

To this end, note the property of the vector spherical harmonics

$$\hat{\boldsymbol{r}}\times\boldsymbol{Y}_{lm}(\hat{\boldsymbol{r}}) = 0\,, \tag{3.65a}$$

$$\hat{\boldsymbol{r}}\times\boldsymbol{\Psi}_{lm}(\hat{\boldsymbol{r}}) = \boldsymbol{\Phi}_{lm}(\hat{\boldsymbol{r}})\,, \tag{3.65b}$$

$$\hat{\boldsymbol{r}}\times\boldsymbol{\Phi}_{lm}(\hat{\boldsymbol{r}}) = -\boldsymbol{\Psi}_{lm}(\hat{\boldsymbol{r}})\,, \tag{3.65c}$$

and that the only non-vanishing integral over the sphere here is $\int d\Omega \boldsymbol{\Psi}_{10} = 2\sqrt{\frac{4\pi}{3}}\hat{\boldsymbol{z}}$ (see detailes in Appendix A.3). Moreover the radial integral also gives a simple relation

$$\int dr\ r^3 h^{(1)}(\eta r) = \frac{3i}{\eta^4}\,. \tag{3.66}$$

Thus, given the coefficient c_{10} (3.45) associated with the pointlike magnetic dipole, the volume integral (3.64) becomes

$$\sum_{\boldsymbol{Z}=\boldsymbol{Y},\boldsymbol{\Psi},\boldsymbol{\Phi}} \int d^3\boldsymbol{r}\ Q_{10}^{\boldsymbol{Z}}(\boldsymbol{r}\times\boldsymbol{Z}_{10}) = \big(8\pi M_0^d(\eta^*)^2\big)\hat{\boldsymbol{z}}. \tag{3.67}$$

Finally, using this relation together with the definition of toroidal dipole moments (3.63) yields the relations

$$\boldsymbol{T}_{10}^{\boldsymbol{H}} = -8\pi M_0^d \Gamma\sqrt{1-\Gamma^2}\hat{\boldsymbol{z}}, \quad \text{and} \quad \boldsymbol{T}_{10}^{\boldsymbol{B}} = -4\pi M_0^d \Gamma\hat{\boldsymbol{z}}\,. \tag{3.68}$$

It follow, as illustrated in Fig. 3.6, that both toroidal dipole moments vanish in the centrosymmetric case. Interestingly, unlike $\boldsymbol{T}_{10}^{\boldsymbol{B}}$ which is a linear function of the parity breaking parameter Γ, the toroidal moment $\boldsymbol{T}_{10}^{\boldsymbol{H}}$ also vanishes at maximal parity breaking $\Gamma = 1$. The observation of a toroidal dipole moment of either $\boldsymbol{B}$ or $\boldsymbol{H}$ thus unambiguously signals the presence of a toroflux induced by a magnetic dipole.

3.3 Experimental detection of the toroflux state

The toroflux could be in principle be detected with the muon-spin spectroscopy [101]. This method is a powerful tool to probe magnetic fields inside superconductors, allowing to shed light on their superconducting properties [102, 103].

The muon-spin spectroscopy involves implanting spin-polarized positively charged muons (also called antimuons) in the bulk of the sample. After coming to rest inside the material, the spin of each muon starts to precess about the axis of the local magnetic field. The precession, however, does not last long, as the muon decays with a half-life of 2.2 μs. The crucial ingredient of the method is that the product of the decay, a positron, carries information about the direction of the muon spin at the time of the decay. Therefore, the measurement of the spatial distribution of the emitted positrons probes the local magnetic environment inside the materials. In addition, the method is susceptible to weak field variations, which makes it especially useful in probing the internal field structure.

The decomposition of the positron spectrum over the vector spherical harmonic modes yields direct information on the knottedness of the toroflux lines, which, in turn, can provide information about the parity-breaking parameter Γ. In our article, we do not discuss the details of the experimental techniques. Instead, we assume that

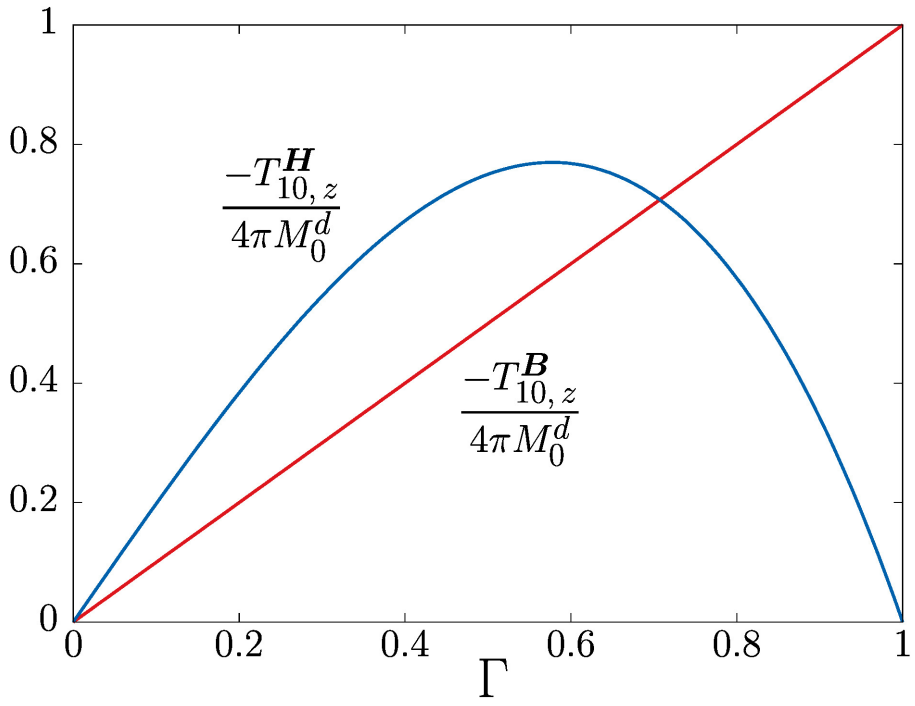

Figure 3.6: The amplitude of the toroidal dipole moments of the toroflux induced by a point-like magnetic dipole, as functions of the parity breaking coupling Γ. The toroidal dipole moment associated with the induction $\boldsymbol{T}^{\boldsymbol{B}}_{10}$ grows linearly with Γ, taking its maximum at the maximal value of the parity breaking parameter, $\Gamma = 1$. Quite surprisingly, $\boldsymbol{T}^{\boldsymbol{B}}_{10}$, the magnetic dipole moment $\boldsymbol{T}^{\boldsymbol{H}}_{10}$ is maximal at $\Gamma = 1/\sqrt{3}$, and vanishes at maximal parity breaking.

the spectrum gives information about the spherical modes of the magnetic field, in a natural extension of the earlier experiments [102, 103].

Since the experiment detects the volume-averaged flux of positrons, the positron spectrum is insensitive to the position of the toroflux inside the sample but is susceptible to the toroflux orientation. Setting the coordinate system along the axial symmetry vector of the toroflux, the magnetic moments of the magnetic field $\boldsymbol{H}$ of the toroflux solution are:

$$a^{\boldsymbol{Z}}_{lm,l'm'} = \int d^3\boldsymbol{r}\boldsymbol{H}_{lm}(\boldsymbol{r})\boldsymbol{Z}_{l'm'}(\boldsymbol{r})\,. \tag{3.69}$$

For the simplest $(l, m) = (1, 0)$ solution, given explicitly in Eq. (3.48), the monopole component is obviously zero, $a^{\boldsymbol{Z}}_{00}$ (where for short we note $a^{\boldsymbol{Z}}_{l'm'} \equiv a^{\boldsymbol{Z}}_{10,l'm'}$). For the experimentally relevant small values of the radius $r_0 \ll 1$, the $(l', m') = (1, 0)$ dipole-

moment components take the following form:

$$a_{10}^{\boldsymbol{Y}} = -4M_0^d\sqrt{\frac{\pi}{3}}\Big\{\Big(\ln r_0+\gamma_E-1\Big)\cos\Gamma+\Gamma\sin\Gamma\Big\}+\mathcal{O}(r_0^2)\,, \tag{3.70a}$$

$$a_{10}^{\boldsymbol{\Psi}} = 4M_0^d\sqrt{\frac{\pi}{3}}\Big\{\Big(\ln r_0+\gamma_E-2\Big)\cos\Gamma+\Gamma\sin\Gamma\Big\}+\mathcal{O}(r_0^2)\,, \tag{3.70b}$$

$$a_{10}^{\boldsymbol{\Phi}} = 8M_0^d\sqrt{\frac{\pi}{3}}\sin\Gamma+\mathcal{O}(r_0)\,, \tag{3.70c}$$

where γ_E is the Euler-Mascheroni constant. In the centrosymmetric limit $\Gamma\to 0$, the radial $a_{10}^{\boldsymbol{Y}}$, and polar, $a_{10}^{\boldsymbol{\Psi}}$, dipole components of the toroflux solution are nonvanishing. These components are characteristics of an ordinary magnetic dipole which possesses a trivial, unknotted magnetic field. Despite of the apparent logarithmic divergence in small impurity limit, $r_0\to 0$, the dipole moments $a_{10}^{\boldsymbol{Y}}$ and $a_{10}^{\boldsymbol{\Psi}}$ do not diverge since at a constant magnetic dipole density M_0, since the total dipole moment $M_0^d=M_0^d(r_0)$ diminishes with decreasing radius as r_0^3, as seen in Eq. (3.44). However, the presence of a nonvanishing azimuthal dipole component, $a_{10}^{\boldsymbol{\Phi}}\sim\Gamma$, which could potentially be detected in a muon-spin spectroscopy, can be considered as a clear sign of the presence of the knotted magnetic lines that are inherent to our toroflux solution.

The nonvanishing $a_{10}^{\boldsymbol{\Phi}}$ component (3.70) is calculated in the (laboratory) coordinate system in which the z axis is co-aligned with magnetic dipole moment of the impurity. If these axis are misaligned, then, in a general coordinate system, the toroflux-sensitive coefficient $a_{10}^{\boldsymbol{\Phi}}$ will be different from the result of Eq. (3.70). The difference between the system associated with the toroflux and the laboratory coordinate system are given by a spatial rotation with a matrix $\hat{R}$. Under rotation, the (l,m) vector spherical harmonics transformed linearly into each other with the proportionality coefficients given by the Wigner D-matrices [104]. In particular, $\hat{R}\boldsymbol{\Phi}_{lm}=\sum_{m'=-l}^{l}D^l_{mm'}\Phi_{lm'}$. Substituting this equation into the definition of the magnetic moments (3.69), we observe by an explicit calculation that for the $(l,m)=(1,0)$ toroflux solution (3.48), the component $a_{10}^{\boldsymbol{\Phi}}$ is nonzero (3.70), while other two components with $m=\pm1$ vanish, $a_{1,\pm1}^{\boldsymbol{\Phi}}\equiv 0$. Therefore, in the rotated coordinate system, the $\boldsymbol{\Phi}$ magnetic dipole moment is given by

$$a_{10}^{\boldsymbol{\Phi}}(\vartheta)=D^1_{00}(\vartheta)a_{10}^{\boldsymbol{\Phi}}\,, \tag{3.71}$$

where $a_{10}^{\boldsymbol{\Phi}}$ is the magnetic moment in the local system associated with the toroflux solution and ϑ is the angle between the symmetry axis of the toroflux and the z axis of the laboratory system.

Taking into account the value of the corresponding Wigner matrix, $D^1_{00}(\vartheta)=\cos\vartheta$, one gets:

$$a_{10}^{\boldsymbol{\Phi}}(\vartheta)=4M_0^d\sqrt{\frac{\pi}{3}}\Gamma\cos\vartheta\,. \tag{3.72}$$

The $\mathbf{\Phi}$ component of the magnetic moment (3.72) has the same properties as the usual magnetic moment because it measures the projection of the dipole moment onto the z axis. Its value is maximal when the z axis is co-aligned with the axis of the toroflux ($\vartheta = 0$) and it vanishes when the axis are perpendicular to each other ($\vartheta = \pi/2$). Detecting a nonvanishing coefficient $a_{10}^{\mathbf{\Phi}}$, for example in a muon-spin experiment, should signal the presence of the toroflux induced by a magnetic dipole. Since the importance of the $\kappa_{\pm}$ term in the Ginzburg-Landau functional strongly depends on the temperature, that will also help differentiating the effects of noncentrosymmetricity from the effects caused by a random polarisation of magnetic inclusions.

Conclusion

We demonstrated that noncentrosymmetric superconductors with broken inversion symmetry host a new family of stable configurations with self-knotted magnetic field lines. Existence of these solutions was presented in the London limit of the Ginzburg-Landau formalism in the presence of the parity-breaking Lifshitz term allowed by the O point group symmetry. These states, which we call "toroflux" or "spheromak", are superconducting counterparts of the Chandrasekhar-Kendall states that play an important role in highly conducting, force-free plasmas relevant to astrophysical research and applications in nuclear fusion [42, 43].

The knotted nature of the toroflux states is rooted in the parity breaking magnetoelectric effect that generates the supercurrent along the magnetic field lines. The supercurrent also produces the magnetic field, thus linking the magnetic field lines of the toroflux. The toroflux is characterized by a non-vanishing toroidal dipole moment of the magnetic field that linearly depends on the parity breaking parameter Γ. They are characterized as well by the helicity of the magnetic field, which vanishes in the absence of the parity breaking ($\Gamma = 0$), indicating that the knottedness disappears. The broken parity in a noncentrosymmetric superconductor plays a crucial role in the existence of the toroflux since no such configurations are possible in an ordinary superconductors with unbroken parity.

The Meissner effect forces the spatial localization of the toroflux solutions, thus making them different from the conventional Chandrasekhar-Kendall states. The size of the solution is determined by the London penetration length λ_L and the dimensionless parity breaking parameter $0 < \Gamma < 1$, as $L_{\rm tor} = \lambda_L/\sqrt{1-\Gamma^2}$. In the limit of the maximal parity violation, $\Gamma \to 1$, the size diverges.

Torofluxes constitute an infinitely high tower of solutions labeled by orbital $0 < l < \infty$ and magnetic $-l \leqslant m \leqslant l$ quantum numbers. Although the energy of any (l,m)-toroflux diverges at its core in the London limit, one could argue that the toroflux energy should be finite beyond this limit (similarly to the energy density of the Abrikosov vortices, which is divergent in the London limit if a core cutoff is neglected and finite otherwise).

Contrary to the Abrikosov vortices, the spheromak configurations carry a non-quantized magnetic field. Consequently, the energy of our spheromak solution is not

quantized, and therefore, it can be made arbitrarily small. The absence of the energy gap should facilitate the creation of the spheromak-field configuration at the isolated spherical pinning centers in noncentrosymmetric superconductors. Moreover, we show that a finite-sized ferromagnetic inclusion with an (l, m)-multipole moment regularize the divergences and thus induces an (l, m)-toroflux with finite energy. The most physically relevant case we discuss here in detail is the case of magnetic dipole inclusion $(l, m) = (1, 0)$. Note that, in general, our solutions are regularized by any finite-size magnetized inclusion with a nonvanishing (l, m)-multipole moment.

These findings open up the possibility of extracting new information about noncentrosymmetric superconductors from muon spin rotation probes. A muon spin rotation probe allows to obtain the statistics of the magnetic field distribution in a superconductor. Our study suggests that doping a noncentrosymmetric superconductor with magnetic impurities will result into toroflux: helical localized configurations of the magnetic field. We have shown that the distribution of magnetic field polarizations that we obtain for toroflux solutions is principally different from a dipole field configuration of a magnetic impurity in a conventional superconductor. It could potentially allow us to extract the parameters $\varkappa_{\pm}$ from the statistics of the polarization of the magnetic field sensed by muons.

As a further study of this subject, numerical studies by Monte Carlo methods are planned, which will allow considering the complete theory with dynamic interactions of scalar order ψ and vector electromagnetic field $\boldsymbol{A}$.

On the basis of the results of this study, the properties of noncentrosymmetric superconductors with other crystal point symmetry groups can be studied in the London limit.

The developed methods can also be applied to search for similar compact nodal configurations in non-Abelian gauge field theories like the Yang–Mills theory.

Appendices

Appendices

A Vector spherical harmonics

The scalar spherical harmonics [105] are defined as

$$Y_{lm}(\hat{\boldsymbol{r}}) = (-1)^m \sqrt{\frac{2l+1}{4\pi}\frac{(l-m)!}{(l+m)!}} P_l^m(\cos\theta) e^{im\phi}, \tag{A.1}$$

where P_l^m are the associated Legendre polynomials [105], which are defined by the Rodrigues' formula:

$$P_l^m(x) \;=\; \frac{(-1)^m}{2^l l!}(1-x^2)^{m/2}\frac{d^{l+m}}{dx^{l+m}}[(x^2-1)^l]\,. \tag{A.2}$$

The spherical harmonics depend on the polar and azimuthal ϕ angles expressed collectively via the unit vector $\hat{\boldsymbol{r}} = \boldsymbol{r}/r$. The spherical harmonics satisfy the orthonormality condition:

$$\int d\Omega\, Y_{lm}(\hat{\boldsymbol{r}}) Y^*_{l'm'}(\hat{\boldsymbol{r}}) = \delta_{ll'}\delta_{mm'}, \tag{A.3}$$

where $Y^*_{lm} \equiv (-1)^m Y_{l,-m}$ and $d\Omega = \sin\theta d\theta d\phi$ - is the solid-angle element.

Adopting the parametrization of [92], the vector spherical harmonics are defined via their scalar counterpart (A.1):

$$\boldsymbol{Y}_{lm}(\hat{\boldsymbol{r}}) \;=\; Y_{lm}(\hat{\boldsymbol{r}})\hat{\boldsymbol{r}}\,, \tag{A.4a}$$

$$\boldsymbol{\Psi}_{lm}(\hat{\boldsymbol{r}}) \;=\; r\boldsymbol{\nabla} Y_{lm}(\hat{\boldsymbol{r}})\,, \tag{A.4b}$$

$$\boldsymbol{\Phi}_{lm}(\hat{\boldsymbol{r}}) \;=\; \boldsymbol{r}\times\boldsymbol{\nabla} Y_{lm}(\hat{\boldsymbol{r}})\,. \tag{A.4c}$$

In a given (l, m) sector, the vector spherical harmonics are locally orthogonal to each other at every point of the unit sphere:

$$\boldsymbol{Y}_{lm}(\hat{\boldsymbol{r}})\cdot\boldsymbol{\Psi}_{lm}(\hat{\boldsymbol{r}}) \;=\; 0, \tag{A.5a}$$

$$\boldsymbol{Y}_{lm}(\hat{\boldsymbol{r}})\cdot\boldsymbol{\Phi}_{lm}(\hat{\boldsymbol{r}}) \;=\; 0, \tag{A.5b}$$

$$\boldsymbol{\Psi}_{lm}(\hat{\boldsymbol{r}})\cdot\boldsymbol{\Phi}_{lm}(\hat{\boldsymbol{r}}) \;=\; 0. \tag{A.5c}$$

They also satisfy the following normalization:

$$\int d\Omega\, \boldsymbol{Y}_{lm}(\hat{\boldsymbol{r}}) \cdot \boldsymbol{Y}^*_{l'm'}(\hat{\boldsymbol{r}}) = \delta_{ll'}\delta_{mm'}\,, \tag{A.6a}$$

$$\int d\Omega\, \boldsymbol{\Phi}_{lm}(\hat{\boldsymbol{r}}) \cdot \boldsymbol{\Phi}^*_{l'm'}(\hat{\boldsymbol{r}}) = l(l+1)\delta_{ll'}\delta_{mm'}\,, \tag{A.6b}$$

$$\int d\Omega\, \boldsymbol{\Psi}_{lm}(\hat{\boldsymbol{r}}) \cdot \boldsymbol{\Psi}^*_{l'm'}(\hat{\boldsymbol{r}}) = l(l+1)\delta_{ll'}\delta_{mm'}\,, \tag{A.6c}$$

and orthogonality relations:

$$\int d\Omega\, \boldsymbol{Y}_{lm}(\hat{\boldsymbol{r}}) \cdot \boldsymbol{\Psi}^*_{l'm'}(\hat{\boldsymbol{r}}) = 0, \tag{A.7a}$$

$$\int d\Omega\, \boldsymbol{Y}_{lm}(\hat{\boldsymbol{r}}) \cdot \boldsymbol{\Phi}^*_{l'm'}(\hat{\boldsymbol{r}}) = 0, \tag{A.7b}$$

$$\int d\Omega\, \boldsymbol{\Phi}_{lm}(\hat{\boldsymbol{r}}) \cdot \boldsymbol{\Psi}^*_{l'm'}(\hat{\boldsymbol{r}}) = 0, \tag{A.7c}$$

where

$$\boldsymbol{Z}^*_{lm} \equiv (-1)^m \boldsymbol{Z}_{l,-m}\,, \tag{A.8}$$

for $\boldsymbol{Z}_{lm} = (\boldsymbol{Y}_{lm}, \boldsymbol{\Psi}_{lm}, \boldsymbol{\Phi}_{lm})$.

A.1 Differential operators on vector spherical harmonics

The gradient of a scalar field $\omega(\boldsymbol{r})$ in terms of vector spherical harmonics:

$$\boldsymbol{\nabla}\omega(\boldsymbol{r}) = \sum_{l=0}^{\infty}\sum_{m=-l}^{l}\left(\frac{d\omega_{lm}}{dr}\boldsymbol{Y}_{lm} + \frac{\omega_{lm}}{r}\boldsymbol{\Psi}_{lm}\right). \tag{A.9}$$

The divergence of the vector spherical harmonics is:

$$\boldsymbol{\nabla}\cdot\Big(f(r)\boldsymbol{Y}_{lm}\Big) = \left(\frac{df}{dr} + \frac{2}{r}f\right)Y_{lm}, \tag{A.10a}$$

$$\boldsymbol{\nabla}\cdot\Big(f(r)\boldsymbol{\Psi}_{lm}\Big) = -\frac{l(l+1)}{r}fY_{lm}, \tag{A.10b}$$

$$\boldsymbol{\nabla}\cdot\Big(f(r)\boldsymbol{\Phi}_{lm}\Big) = 0. \tag{A.10c}$$

Similarly, the curl of the vector spherical harmonics gives:

$$\boldsymbol{\nabla}\times\Big(f(r)\boldsymbol{Y}_{lm}\Big) = -\frac{1}{r}f\boldsymbol{\Phi}_{lm}, \tag{A.11a}$$

$$\boldsymbol{\nabla}\times\Big(f(r)\boldsymbol{\Psi}_{lm}\Big) = \left(\frac{df}{dr} + \frac{1}{r}f\right)\boldsymbol{\Phi}_{lm}\,, \tag{A.11b}$$

$$\boldsymbol{\nabla}\times\Big(f(r)\boldsymbol{\Phi}_{lm}\Big) = -\frac{l(l+1)}{r}f\boldsymbol{Y}_{lm} - \left(\frac{df}{dr} + \frac{1}{r}f\right)\boldsymbol{\Psi}_{lm}\,. \tag{A.11c}$$

These relations allow to express the divergence,

$$\boldsymbol{\nabla}\cdot\boldsymbol{G} \;=\; \sum_{l=0}^{\infty}\sum_{m=-l}^{l}\left(\frac{1}{r^2}\frac{d}{dr}(r^2 G^{\boldsymbol{Y}}_{lm}) - \frac{l(l+1)}{r}G^{\boldsymbol{\Psi}}_{lm}\right)Y_{lm}, \tag{A.12}$$

and the curl,

$$\begin{aligned}\boldsymbol{\nabla}\times\boldsymbol{G} \;=\; \sum_{l=0}^{\infty}\sum_{m=-l}^{l}\Bigg[&-\frac{l(l+1)}{r}G^{\boldsymbol{\Phi}}_{lm}\boldsymbol{Y}_{lm} - \left(\frac{dG^{\boldsymbol{\Phi}}_{lm}}{dr}+\frac{1}{r}G^{\boldsymbol{\Phi}}_{lm}\right)\boldsymbol{\Psi}_{lm} \\ &+\left(-\frac{1}{r}G^{\boldsymbol{Y}}_{lm}+\frac{dG^{\boldsymbol{\Psi}}_{lm}}{dr}+\frac{1}{r}G^{\boldsymbol{\Psi}}_{lm}\right)\boldsymbol{\Phi}_{lm}\Bigg],\end{aligned} \tag{A.13}$$

of a generic vector:

$$\begin{aligned}\boldsymbol{G}(\boldsymbol{r}) \;&=\; \sum_{l=0}^{\infty}\sum_{m=-l}^{l}\left(\sum_{\boldsymbol{Z}=\boldsymbol{Y},\boldsymbol{\Psi},\boldsymbol{\Phi}} G^{\boldsymbol{Z}}_{lm}(r)\,\boldsymbol{Z}_{lm}(\hat{\boldsymbol{r}})\right) \\ &=\; \sum_{l=0}^{\infty}\sum_{m=-l}^{l}\left(G^{\boldsymbol{Y}}_{lm}(r)\boldsymbol{Y}_{lm}+G^{\boldsymbol{\Psi}}_{lm}(r)\boldsymbol{\Psi}_{lm}+G^{\boldsymbol{\Phi}}_{lm}(r)\boldsymbol{\Phi}_{lm}\right).\end{aligned} \tag{A.14}$$

A.2 First vector spherical harmonics

It is usefull to condiser a first few spherical harmonics explicitly. Note that the harmonics with negative indices m can be obtained from the equations below, using the conjugacy relation (A.8).

The lowest $l=0$ spherical harmonics is a trivial hedgehog as it possesses a radial component only:

$$\boldsymbol{Y}_{00}=\frac{1}{\sqrt{4\pi}}\hat{\boldsymbol{r}}, \qquad \boldsymbol{\Psi}_{00}=0, \qquad \boldsymbol{\Phi}_{00}=0. \tag{A.15}$$

The first nontrivial vector spherical harmonics starts from the orbital momentum $l=1$:

$$\begin{aligned}\boldsymbol{Y}_{10} &= \sqrt{\tfrac{3}{4\pi}}\cos\theta\,\hat{\boldsymbol{r}}, & \boldsymbol{Y}_{11} &= -\sqrt{\tfrac{3}{8\pi}}e^{i\phi}\sin\theta\,\hat{\boldsymbol{r}}, \\ \boldsymbol{\Psi}_{10} &= -\sqrt{\tfrac{3}{4\pi}}\sin\theta\,\hat{\boldsymbol{\theta}}, & \boldsymbol{\Psi}_{11} &= -\sqrt{\tfrac{3}{8\pi}}e^{i\phi}\left(\cos\theta\,\hat{\boldsymbol{\theta}}+i\hat{\boldsymbol{\phi}}\right), \\ \boldsymbol{\Phi}_{10} &= -\sqrt{\tfrac{3}{4\pi}}\sin\theta\,\hat{\boldsymbol{\phi}}, & \boldsymbol{\Phi}_{11} &= \sqrt{\tfrac{3}{8\pi}}e^{i\phi}\left(i\hat{\boldsymbol{\theta}}-\cos\theta\,\hat{\boldsymbol{\phi}}\right).\end{aligned} \tag{A.16}$$

The basis for $l=2$ vector spherical functions is as follows:

$$\begin{aligned}\boldsymbol{Y}_{20} &= \tfrac{1}{4}\sqrt{\tfrac{5}{\pi}}(3\cos^2\theta-1)\hat{\boldsymbol{r}}, & \boldsymbol{Y}_{21} &= -\sqrt{\tfrac{15}{8\pi}}e^{i\phi}\sin\theta\cos\theta\,\hat{\boldsymbol{r}}, \\ \boldsymbol{\Psi}_{20} &= -\tfrac{3}{2}\sqrt{\tfrac{5}{\pi}}\sin\theta\cos\theta\,\hat{\boldsymbol{\theta}}, & \boldsymbol{\Psi}_{21} &= -\sqrt{\tfrac{15}{8\pi}}e^{i\phi}\left(\cos 2\theta\,\hat{\boldsymbol{\theta}}+i\cos\theta\hat{\boldsymbol{\phi}}\right), \\ \boldsymbol{\Phi}_{20} &= -\tfrac{3}{2}\sqrt{\tfrac{5}{\pi}}\sin\theta\cos\theta\,\hat{\boldsymbol{\phi}}, & \boldsymbol{\Phi}_{21} &= \sqrt{\tfrac{15}{8\pi}}e^{i\phi}\left(i\cos\theta\hat{\boldsymbol{\theta}}-\cos 2\theta\,\hat{\boldsymbol{\phi}}\right),\end{aligned} \tag{A.17a}$$

$$\begin{aligned}\boldsymbol{Y}_{22} &= \tfrac{1}{4}\sqrt{\tfrac{15}{2\pi}}e^{2i\phi}\sin^2\theta\,\hat{\boldsymbol{r}}, \\ \boldsymbol{\Psi}_{22} &= \sqrt{\tfrac{15}{8\pi}}e^{2i\phi}\sin\theta\left(\cos\theta\,\hat{\boldsymbol{\theta}}+i\hat{\boldsymbol{\phi}}\right), \\ \boldsymbol{\Phi}_{22} &= \sqrt{\tfrac{15}{8\pi}}e^{2i\phi}\sin\theta\left(-i\hat{\boldsymbol{\theta}}+\cos\theta\,\hat{\boldsymbol{\phi}}\right).\end{aligned} \tag{A.17b}$$

A.3 Integrals of vector spherical functions

The integrals of vector spherical harmonics over $d\Omega = \sin\theta d\theta d\phi$ for $l = 0$ are vanished:

$$\int d\Omega\, \boldsymbol{Y}_{00} \;\; = 0\,. \tag{A.18}$$

In the case of $l = 1$ we have some nontrivial result:

$$\begin{aligned}
\int d\Omega\, \boldsymbol{Y}_{10} &= \sqrt{\tfrac{4\pi}{3}}\,\hat{\boldsymbol{z}}, & \int d\Omega\, \boldsymbol{Y}_{11} &= -\sqrt{\frac{2\pi}{3}}\,(\hat{\boldsymbol{x}} + i\hat{\boldsymbol{z}}), \\
\int d\Omega\, \boldsymbol{\Psi}_{10} &= 2\sqrt{\tfrac{4\pi}{3}}\,\hat{\boldsymbol{z}}, & \int d\Omega\, \boldsymbol{\Psi}_{11} &= -\sqrt{\frac{8\pi}{3}}\,(\hat{\boldsymbol{x}} + i\hat{\boldsymbol{z}}), \\
\int d\Omega\, \boldsymbol{\Phi}_{10} &= 0, & \int d\Omega\, \boldsymbol{\Phi}_{11} &= 0,
\end{aligned} \tag{A.19}$$

where the unit vectors of the spherical coordinate system $(\hat{\boldsymbol{r}}, \hat{\boldsymbol{\theta}}, \hat{\boldsymbol{\phi}})$ are expressed in terms of the unit vectors of the Cartesian coordinate system $(\hat{\boldsymbol{x}}, \hat{\boldsymbol{y}}, \hat{\boldsymbol{z}})$:

$$\hat{\boldsymbol{r}} = \sin\theta(\cos\phi\,\hat{\boldsymbol{x}} + \sin\phi\,\hat{\boldsymbol{y}}) + \cos\theta\,\hat{\boldsymbol{z}}\,, \tag{A.20a}$$

$$\hat{\boldsymbol{\theta}} = \cos\theta(\cos\phi\,\hat{\boldsymbol{x}} + \sin\phi\,\hat{\boldsymbol{y}}) - \sin\theta\,\hat{\boldsymbol{z}}\,, \tag{A.20b}$$

$$\hat{\boldsymbol{\phi}} = -\sin\phi\,\hat{\boldsymbol{x}} + \cos\phi\,\hat{\boldsymbol{y}}\,. \tag{A.20c}$$

B Special functions

B.1 Kelvin functions

Definition of the Kelvin function: [106, 107]

$$\begin{aligned}
\mathrm{ker}_\nu(r) + i\mathrm{kei}_\nu(r) &= \frac{1}{2}\pi i H_\nu^{(1)}(r\mathrm{e}^{3\pi i/4}) = -\frac{1}{2}\pi i \mathrm{e}^{-\nu\pi i} H_\nu^{(2)}(r\mathrm{e}^{-\pi i/4}) \\
&= \mathrm{e}^{-\frac{1}{2}\nu\pi i} K_\nu(r\mathrm{e}^{\pi i/4})\,, \qquad \text{(B.1a)} \\
\mathrm{ber}_\nu(r) + i\mathrm{bei}_\nu(r) &= \mathrm{e}^{\nu\pi i/2} I_\nu(r\mathrm{e}^{\pi i/4}) = \mathrm{e}^{3\nu\pi i/2} I_\nu(r\mathrm{e}^{-3\pi i/4}) \\
&= J_\nu(r\mathrm{e}^{3\pi i/4})\,, \qquad \text{(B.1b)}
\end{aligned}$$

where $K_\nu(x)$ is the modified Bessel function of the second kind and $H_\nu^{(i)}$ is the Hankel function (the Bessel function of the third kind).

The series for Kelvin functions:

$$\begin{Bmatrix} \ker_{l+1/2}(x) \\ \mathrm{kei}_{l+1/2}(x) \end{Bmatrix} \approx \pm 2^{l-1/2} x^{-l-1/2} \Gamma(l+1/2) \tag{B.2a}$$
$$\times \sum_{k=0}^{k<l+1/2} \begin{Bmatrix} \cos[(3(l+1/2)-2k)\pi/4] \\ \sin[(3(l+1/2)-2k)\pi/4] \end{Bmatrix} \frac{(x/2)^{2k}}{(1/2-l)^k k!},$$
$$\begin{Bmatrix} \mathrm{ber}_{l+1/2}(x) \\ \mathrm{bei}_{l+1/2}(x) \end{Bmatrix} \approx \left(\frac{x}{2}\right)^{l+1/2} \tag{B.2b}$$
$$\times \sum_{k=0}^{\infty} \begin{Bmatrix} \cos[(3(l+1/2)+2k)\pi/4] \\ \sin[(3(l+1/2)+2k)\pi/4] \end{Bmatrix} \frac{(x/2)^{2k}}{k!\Gamma(l+k+3/2)}.$$

The asymptotic expansion for large arguments:

$$\ker_\nu(x) = \sqrt{\frac{\pi}{2x}} e^{-\frac{x}{\sqrt{2}}} \Big[\; a_\nu(-x)\cos\beta - b_\nu(-x)\sin\beta \Big], \tag{B.3a}$$
$$\mathrm{kei}_\nu(x) = \sqrt{\frac{\pi}{2x}} e^{-\frac{x}{\sqrt{2}}} \Big[-a_\nu(-x)\sin\beta - b_\nu(-x)\cos\beta \Big], \tag{B.3b}$$
$$\mathrm{ber}_\nu(x) = \frac{1}{\sqrt{2\pi x}} e^{\frac{x}{\sqrt{2}}} \Big[\; a_\nu(x)\cos\left(\beta - \frac{\pi}{4}\right) + b_\nu(x)\sin\left(\beta - \frac{\pi}{4}\right) \Big], \tag{B.3c}$$
$$\mathrm{bei}_\nu(x) = \frac{1}{\sqrt{2\pi x}} e^{\frac{x}{\sqrt{2}}} \Big[\; a_\nu(x)\sin\left(\beta - \frac{\pi}{4}\right) - b_\nu(x)\cos\left(\beta - \frac{\pi}{4}\right) \Big], \tag{B.3d}$$

where

$$\beta \equiv \beta_\nu(x) = \frac{x}{\sqrt{2}} + \left(\frac{1}{2}\nu + \frac{1}{8}\right)\pi,$$
$$a_\nu(\pm x) \sim 1 + \sum_{k=1}^{\infty} h_{k,\nu}^{(\pm)}(x) \cos\left(\frac{k\pi}{4}\right),$$
$$b_\nu(\pm x) \sim \sum_{k=1}^{\infty} h_{k,\nu}^{(\pm)}(x) \sin\left(\frac{k\pi}{4}\right),$$

and

$$h_{k,\nu}^{(\pm)}(x) = \frac{(4\nu^2-1)(4\nu^2-9)...(4\nu^2-(2k-1)^2)}{(\mp 8x)^k k!}.$$

In this study, we also use the following recurrence relations

$$f_{\nu+1} + f_{\nu-1} = -\frac{\nu\sqrt{2}}{x}(f_\nu - g_\nu), \tag{B.4a}$$
$$f'_\nu = \pm\left(\frac{\nu}{x} f_\nu + \frac{1}{\sqrt{2}}\left(f_{\nu\pm1} + g_{\nu\pm1}\right)\right), \tag{B.4b}$$

and useful integral including the Kelvin functions:

$$\int dx\; x\Big(f_\nu^2 + g_\nu^2\Big) = x\Big(f_\nu g'_\nu - f'_\nu g_\nu\Big) \tag{B.5}$$
$$= -\frac{x}{\sqrt{2}}\Big(f_\nu f_{\nu+1} + g_\nu g_{\nu+1} - f_\nu g_{\nu+1} + f_{\nu+1} g_\nu\Big),$$

where f_ν and g_ν are any one of two pairs:

$$\left\{\begin{matrix} f_\nu = \ker_\nu(x) \\ g_\nu = \mathrm{kei}_\nu(x) \end{matrix}\right\} \quad \text{or} \quad \left\{\begin{matrix} f_\nu = \ \ \mathrm{kei}_\nu(x) \\ g_\nu = -\ker_\nu(x) \end{matrix}\right\}.$$

B.2 The spherical Hankel functions

The spherical Hankel functions [105] are expressed via the spherical Bessel functions as:

$$h_l^{(1)}(z) = j_l(z) + iy_l(z)\,, \quad h_l^{(2)}(z) = j_l(z) - iy_l(z)\,, \tag{B.6}$$

where, in turn, the spherical Bessel functions are related to the Bessel functions of half-integer order:

$$j_l(z) = \sqrt{\frac{2\pi}{z}} J_{l+1/2}(z)\,, \quad y_l(z) = \sqrt{\frac{2\pi}{z}} Y_{l+1/2}(z)\,, \tag{B.7}$$

with J_l and Y_l being resperctively the Bessel functions of the first and second kind. Note that for a non-negative rank l, the spherical Hankel functions can be expressed in a closed form:

$$h_l^{(1)}(z) = \frac{e^{+iz}}{z} \sum_{p=0}^{l} (+i)^{p-l-1} (2z)^{-p} \frac{(l+p)!}{p!(l-p)!}\,, \tag{B.8a}$$

$$h_l^{(2)}(z) = \frac{e^{-iz}}{z} \sum_{p=0}^{l} (-i)^{p-l-1} (2z)^{-p} \frac{(l+p)!}{p!(l-p)!}\,. \tag{B.8b}$$

For a large $|z|$, when $-\pi < \arg z < \pi$, the spherical Hankel functions have the following asymptotic behaviour at the large argument:

$$h_l^{(1)}(z) \sim \frac{2\pi}{z} \exp\left[+i\left(z - \frac{(l+1)\pi}{2}\right)\right], \tag{B.9a}$$

$$h_l^{(2)}(z) \sim \frac{2\pi}{z} \exp\left[-i\left(z - \frac{(l+1)\pi}{2}\right)\right]. \tag{B.9b}$$

At small z, the spherical Hankel function behave as:

$$h_l^{(1)}(z) \approx -\frac{i2^l \Gamma(l+1/2)}{\sqrt{\pi} z^{l+1}}\,, \tag{B.10a}$$

$$h_l^{(2)}(z) \approx \frac{i2^l \Gamma(l+1/2)}{\sqrt{\pi} z^{l+1}}\,, \tag{B.10b}$$

where $\Gamma(z)$ is the Gamma function.

C Investigaton of structure and dynamics of proteins by the Landau – Ginzburg – Wilson approach

During the research period for this thesis, we were simultaneously involved in two more projects that were not included in this text. The first project was devoted to the analytical and numerical study of the behavior of the baryon density near the Roberge-Weiss transition [108–110]. The second project is related to the study of the structure and dynamic properties of protein molecules using field theory methods [111–113]. This section presents the fundamental ideas and results of the second protein project, which the author began working on while studying at the Bachelor's degree.

Protein folding and unfolding are examples of very complex physical processes, of which an effective theoretical description should matter: the underlying mechanism is always controlled by the same universal biophysical and biochemical principles [114].

Landau-Ginzburg-Wilson (LGW) approach is a systematic methodology for developing an effective theory. This approach is useful for modeling phase properties in systems that have a universal character.

We found that the LGW approach can also describe universal aspects of the tertiary structure of the protein and the effect of temperature on protein dynamics [70, 115–122].

Kink and Protein Backbone Geometry

In this approach, the geometry of the protein is described in terms of the C_α backbone. The positions of the C_α atoms are described by the position vectors $\mathbf{r}_i$, where $i = 1, \cdots, N$ labels the residues. At each position of C_α, there is an orthonormal triplet $(\mathbf{n}_i, \mathbf{t}_i, \mathbf{b}_i)$ with the unit tangent vector

$$\mathbf{t}_i = \frac{\mathbf{r}_{i+1} - \mathbf{r}_i}{|\mathbf{r}_{i+1} - \mathbf{r}_i|}\,, \tag{C.11}$$

the unit binomial vector

$$\mathbf{b}_i = \frac{\mathbf{t}_{i-1} \times \mathbf{t}_i}{|\mathbf{t}_{i-1} \times \mathbf{t}_i|}\,, \tag{C.12}$$

and the unit normal vector

$$\mathbf{n}_i = \mathbf{b}_i \times \mathbf{t}_i\,. \tag{C.13}$$

This defines the discrete Frenet frame [117, 121]. The C_α backbone bond angles κ_i and torsion angles τ_i can be defined in terms of the frame vectors

$$\kappa_i = \arccos\left(\mathbf{t}_{i+1} \cdot \mathbf{t}_i\right)\,, \tag{C.14}$$

$$\gamma_i = \mathrm{sgn}\left[(\mathbf{b}_{i-1} \times \mathbf{b}_i) \cdot \mathbf{t}_i\right] \arccos\left(\mathbf{b}_{i+1} \cdot \mathbf{b}_i\right)\,. \tag{C.15}$$

Conversely, when the values of the bond and torsion angles are all known, the discrete Frenet equation

$$\begin{pmatrix} \mathbf{n}_{i+1} \\ \mathbf{b}_{i+1} \\ \mathbf{t}_{i+1} \end{pmatrix} = \begin{pmatrix} \cos\kappa_i \cos\tau_i & \cos\kappa_i \sin\tau_i & -\sin\kappa_i \\ \sin\tau_i & \cos\tau_i & 0 \\ \sin\kappa_i \cos\tau_i & \sin\kappa_i \sin\tau_i & \cos\kappa_i \end{pmatrix} \begin{pmatrix} \mathbf{n}_i \\ \mathbf{b}_i \\ \mathbf{t}_i \end{pmatrix} , \tag{C.16}$$

computes the frame vectors at every vortex of backbone. Once all the frames are known, the entire chain is obtained by

$$\mathbf{r}_k = \sum_{i=0}^{k-1} |\mathbf{r}_{i+1} - \mathbf{r}_i| \mathbf{t}_i \, . \tag{C.17}$$

Unlike the tangent vector $\mathbf{t}_i$, the normal and binormal vectors $(\mathbf{n}_i, \mathbf{b}_i)$ do not appear in equation above (C.17). Therefore, if these vectors are simultaneously rotated around the vector $\mathbf{t}$, the C_α geometry remains intact, and only the way how it is framed changes. In particular, rotation by π constitutes the discrete Z_2 gauge transformation

$$\tau_i \;\; \rightarrow \;\; \begin{cases} \gamma_i - \pi, \text{ if } \gamma_i > 0, \\ \gamma_i + \pi, \text{ if } \gamma_i < 0, \end{cases} \tag{C.18}$$

$$\kappa_k \;\; \rightarrow \;\; -\kappa_k, \text{ for all } k \geq i, \tag{C.19}$$

which was proved to be very convenient in analyzing the protein loop structure [70, 115–122]. Note that regular protein secondary structures correspond to definite values of (κ_i, τ_i). For example, for the standard right-handed α-helix

$$\begin{cases} \kappa \sim \frac{\pi}{2}, \\ \tau \sim 1, \end{cases} \tag{C.20}$$

and for the standard β-strand

$$\begin{cases} \kappa \sim 1, \\ \tau \sim \pm\pi, \end{cases} \tag{C.21}$$

with the angles in radians.

The variables κ_i and γ_i are mutually connected by the equations of motion, determined by the atomic-level interactions along the protein chain. The free-energy of the polymer can be written in terms of (κ, γ) internal coordinates using a Landau–Ginzburg–Wilson free-energy:

$$F = -\sum_{i=1}^{N-1} 2\kappa_{i+1}\kappa_i + \sum_{i=1}^{N} \left(2\kappa_i^2 + \lambda \left(\kappa_i^2 - m^2 \right)^2 + \frac{q}{2}\kappa_i^2\gamma_i^2 - p\tau_i + \frac{r}{2}\gamma_i^2 \right) , \tag{C.22}$$

where α, m, q, p and r are parameters of the energy. The detailed derivation of this form of free energy can be found in [70, 115, 120, 121].

Minimizing this free-energy (C.22) relative to κ and γ leads to a nonlinear equation of motion for the curvature similar to a generalized DNLS (The Discrete Nonlinear Schrödinger Equation) which admits kinks as particular solutions. Thus, the modular building blocks of folded proteins, i.e., a supersecondary structure such as a helix-loop-helix or strand-loop-strand motif, are described in terms of the kink of a generalized version of the DNLS equation [70, 115–122].

Glauber Algorithm for Protein Dynamics

We examine the dynamics of protein by simulating heating and cooling trajectories using the Glauber algorithm [123]. In other words, we combine the Landau–Ginzburg–Wilson approach with Glauber dynamics to study in detail how these systems unfold and fold. Glauber dynamics is a Markov chain Monte Carlo method that is widely used to describe near-equilibrium relaxation dynamics of a statistical system toward equilibrium Gibbs state. It should be noted that the Glauber algorithm manages the dynamics of simple spin chain systems coming close to the thermal equilibrium, which also obeys the Arrhenius law [124]. Since proteins can be regarded as spin chains, it is natural to simulate protein folding in terms of the Glauber algorithm.

The main results obtained

It is described how myoglobin unfolds from the native folded state to a random coil when temperature and acidity increase. The presence of two molten globule folding intermediates is confirmed and an abrupt transition between the two is predicted when acidity changes. The results obtained also suggest that the ligand entry and exit of the ligand are driven by large-scale collective motions that destabilize the myoglobin F-helix [123].

Some aspects of topology in protein folding was investigated. The temperature-driven folding and unfolding of the slipknotted archaeal virus protein AFV3-109 was simulated. These simulations also reveal that with a change in temperature, this protein proceeds through a folding intermediate step – a trefoil knot. [85].

We show that without molecular dynamics simulations, the kinks are able to identify not only the phosphorylated sites of protein, the key players in folding, but also the reasons for the weak stability of the eIF4E-binding protein 2 (4E-BP2) [109].

We demonstrate that the kinks are capable of identifying the key residues causing structural flexibility of αS. In addition, the stability of the experimental structures of αS is investigated by simulating heating/cooling trajectories using the Glauber algorithm. The findings are consistent with experiments [110].

Bibliography

[1] William Thomson. "On Vortex Atoms". In: *Proceedings of the Royal Society of Edinburgh* 6 (1869), pp. 94–105. DOI: 10.1017/S0370164600045430.

[2] Louis H Kauffman. *Knots and Physics*. 3rd. WORLD SCIENTIFIC, July 2001. DOI: 10.1142/8338. eprint: https://www.worldscientific.com/doi/pdf/10.1142/4256.

[3] Y. M. Cho, Seung Hun Oh, and Pengming Zhang. "Knots in physics". In: *International Journal of Modern Physics A* 33.07 (2018), p. 1830006. DOI: 10.1142/S0217751X18300065.

[4] Heike Kamerlingh Onnes. In: *Leiden Comm.* 124c (1911).

[5] W. Meissner and R. Ochsenfeld. "Ein neuer Effekt bei Eintritt der Supraleitfähigkeit". In: *Naturwissenschaften* 21.44 (Nov. 1933), pp. 787–788. DOI: 10.1007/bf01504252.

[6] Michael Tinkham. *Introduction to Superconductivity*. 2nd ed. Dover Publications, June 2004. ISBN: 0486435032.

[7] V. V. Schmidt. *The Physics of Superconductors*. Ed. by Paul Müller and Alexey V. Ustinov. Springer Berlin Heidelberg, 1997. DOI: 10.1007/978-3-662-03501-6.

[8] Filipp N. Rybakov, Julien Garaud, and Egor Babaev. "Stable Hopf-Skyrme topological excitations in the superconducting state". In: *Physical Review B* 100.9 (Sept. 2019). ISSN: 2469-9969. DOI: 10.1103/physrevb.100.094515.

[9] L.N. Bulaevskii, A.A. Guseinov, and A.I. Rusinov. "Superconductivity in crystals without symmetry centers". In: *Soviet Journal of Experimental and Theoretical Physics* 44 (6 Dec. 1976). (Russian original - ZhETF, Vol. 71, No. 6, p. 2356, December 1976), p. 1243.

[10] L.S. Levitov, Yu. V. Nazarov, and G.M. Eliashberg. "Magnetoelectric effects in conductors with mirror isomer symmetry". In: *Soviet Journal of Experimental and Theoretical Physics* 61 (1 Jan. 1985). (Russian original - ZhETF, Vol. 88, No. 1, p. 229, January 1985), p. 133.

[11] L.S. Levitov, Yu. V. Nazarov, and G.M. Eliashberg. "Magnetostatics of superconductors without an inversion center". In: *Soviet Journal of Experimental and Theoretical Physics Letters* 41 (1985). (Russian original - Pis'ma Zh. Eksp. Teor. Fiz., Vol. 41, No. 9, p. 365, 1985), p. 445.

[12] V. P. Mineev and K. V. Samokhin. "Helical phases in superconductors". In: *Soviet Journal of Experimental and Theoretical Physics* 78 (Mar. 1994). (Russian original - Zh. Eksp. Teor. Fiz., Vol.105, No. 3, pp. 747-763, 1994), pp. 401–409.

[13] Victor M Edelstein. "The Ginzburg - Landau equation for superconductors of polar symmetry". In: *Journal of Physics: Condensed Matter* 8.3 (Jan. 1996), pp. 339–349. DOI: 10.1088/0953-8984/8/3/012.

[14] D.F. Agterberg. "Novel magnetic field effects in unconventional superconductors". In: *Physica C: Superconductivity* 387.1-2 (May 2003), pp. 13–16. DOI: http://dx.doi.org/10.1016/S0921-4534(03)00634-8.

[15] K. V. Samokhin. "Magnetic properties of superconductors with strong spin-orbit coupling". In: *Physical Review B* 70.10 (Sept. 2004). DOI: 10.1103/PhysRevB.70.104521.

[16] E. Bauer et al. "Heavy Fermion Superconductivity and Magnetic Order in Noncentrosymmetric $CePt_3Si$". In: *Phys. Rev. Lett.* 92 (2 Jan. 2004), p. 027003. DOI: 10.1103/PhysRevLett.92.027003.

[17] K. V. Samokhin, E. S. Zijlstra, and S. K. Bose. "$CePt_3Si$: An unconventional superconductor without inversion center". In: *Phys. Rev. B* 69 (9 Mar. 2004), p. 094514. DOI: 10.1103/PhysRevB.69.094514.

[18] H. Q. Yuan et al. "*S*-Wave Spin-Triplet Order in Superconductors without Inversion Symmetry: Li_2Pd_3B and Li_2Pt_3B". In: *Phys. Rev. Lett.* 97 (1 July 2006), p. 017006. DOI: 10.1103/PhysRevLett.97.017006.

[19] A. S. Cameron et al. "Rotation of the magnetic vortex lattice in Ru_7B_3 driven by the effects of broken time-reversal and inversion symmetry". In: *Physical Review B* 100.2 (July 2019). DOI: 10.1103/PhysRevB.100.024518.

[20] Rustem Khasanov et al. "Multiple-gap response of type-I noncentrosymmetric BeAu superconductor". In: *Physical Review Research* 2.2 (May 2020). DOI: 10.1103/PhysRevResearch.2.023142.

[21] E. Bauer and M. Sigrist. *Non-Centrosymmetric Superconductors: Introduction and Overview*. Ed. by E. Bauer and M. Sigrist. Lecture notes in physics. Springer, 2012. ISBN: 978-3-642-24624-1. DOI: 10.1007/978-3-642-24624-1.

[22] Sungkit Yip. "Noncentrosymmetric Superconductors". In: *Annual Review of Condensed Matter Physics* 5.1 (2014), pp. 15–33. DOI: 10.1146/annurev-conmatphys-031113-133912. eprint: https://doi.org/10.1146/annurev-conmatphys-031113-133912.

[23] M. Smidman et al. "Superconductivity and spin–orbit coupling in non-centrosymmetric materials: a review". In: *Reports on Progress in Physics* 80.3 (Jan. 2017), p. 036501. DOI: 10.1088/1361-6633/80/3/036501.

[24] M. K. Kashyap and D. F. Agterberg. "Vortices in cubic noncentrosymmetric superconductors". In: *Physical Review B* 88.10 (Sept. 2013). DOI: 10.1103/PhysRevB.88.104515.

[25] Petre Badica, Takaaki Kondo, and Kazumasa Togano. "Superconductivity in a New Pseudo-Binary $Li_2B(Pd_{1-x}Pt_x)_3$ (x=0–1) Boride System". In: *Journal of the Physical Society of Japan* 74.3 (2005), pp. 1014–1019. DOI: 10.1143/JPSJ.74.1014.

[26] A. B. Karki et al. "Structure and physical properties of the noncentrosymmetric superconductor Mo_3Al_2C". In: *Phys. Rev. B* 82 (6 Aug. 2010), p. 064512. DOI: 10.1103/PhysRevB.82.064512.

[27] E. Bauer et al. "Unconventional superconducting phase in the weakly correlated noncentrosymmetric Mo_3Al_2C compound". In: *Phys. Rev. B* 82 (6 Aug. 2010), p. 064511. DOI: 10.1103/PhysRevB.82.064511.

[28] Ryosuke Mizutani et al. "Superconductivity in PtSbS with a Noncentrosymmetric Cubic Crystal Structure". In: *Journal of the Physical Society of Japan* 88.9 (2019), p. 093709. DOI: 10.7566/JPSJ.88.093709.

[29] L. Faddeev and Antti J. Niemi. "Stable knot-like structures in classical field theory". In: *Nature* 387.6628 (May 1997), pp. 58–61. DOI: 10.1038/387058a0.

[30] H. K. Moffatt. "The degree of knottedness of tangled vortex lines". In: *Journal of Fluid Mechanics* 35.1 (1969), pp. 117–129. DOI: 10.1017/S0022112069000991.

[31] Mitchell A Berger. "Introduction to magnetic helicity". In: *Plasma Physics and Controlled Fusion* 41.12B (Dec. 1999), B167–B175. DOI: https://doi.org/10.1088/0741-3335/41/12B/312.

[32] Egor Babaev. "Dual Neutral Variables and Knot Solitons in Triplet Superconductors". In: *Physical Review Letters* 88.17 (Apr. 2002). DOI: 10.1103/PhysRevLett.88.177002.

[33] Paul Sutcliffe. "Skyrmion Knots in Frustrated Magnets". In: *Physical Review Letters* 118.24 (June 2017). DOI: 10.1103/PhysRevLett.118.247203.

[34] F. N. Rybakov et al. *Magnetic hopfions in solids*. 2019. DOI: 10.48550/ARXIV.1904.00250.

[35] Eugen Radu and Mikhail S. Volkovra. "Stationary ring solitons in field theory — Knots and vortons". In: *Physics Reports* 468.4 (Nov. 2008), pp. 101–151. DOI: 10.1016/j.physrep.2008.07.002.

[36] Richard A. Battye and P. M. Sutcliffe. "Knots as Stable Soliton Solutions in a Three-Dimensional Classical Field Theory". In: *Physical Review Letters* 81.22 (Nov. 1998), pp. 4798–4801. DOI: 10.1103/PhysRevLett.81.4798.

[37] M. N. Chernodub. *Free magnetized knots of parity-violating deconfined matter in heavy-ion collisions*. 2010. DOI: 10.48550/ARXIV.1002.1473.

[38] Kirill Tuchin. "Electromagnetic field and the chiral magnetic effect in the quark-gluon plasma". In: *Physical Review C* 91.6 (June 2015). DOI: 10.1103/PhysRevC.91.064902.

[39] Yuji Hirono, Dmitri E. Kharzeev, and Yi Yin. "Self-similar inverse cascade of magnetic helicity driven by the chiral anomaly". In: *Physical Review D* 92.12 (Dec. 2015). DOI: 10.1103/PhysRevD.92.125031.

[40] Kirill Tuchin. "Excitation of Chandrasekhar-Kendall photons in quark gluon plasma by propagating ultrarelativistic quarks". In: *Physical Review C* 93.5 (May 2016). DOI: 10.1103/PhysRevC.93.054903.

[41] Xiao-liang Xia, Hong Qin, and Qun Wang. "Approach to Chandrasekhar-Kendall-Woltjer state in a chiral plasma". In: *Physical Review D* 94.5 (Sept. 2016). DOI: 10.1103/PhysRevD.94.054042.

[42] S. Chandrasekhar and P. C. Kendall. "On Force-Free Magnetic Fields." In: *The Astrophysical Journal* 126 (Sept. 1957), p. 457. DOI: 10.1086/146413.

[43] J. B. Taylor. "Relaxation of Toroidal Plasma and Generation of Reverse Magnetic Fields". In: *Phys. Rev. Lett.* 33 (19 Nov. 1974), pp. 1139–1141. DOI: 10.1103/PhysRevLett.33.1139.

[44] M.N. Rosenbluth and M.N. Bussac. "MHD stability of Spheromak". In: *Nuclear Fusion* 19.4 (Apr. 1979), pp. 489–498. DOI: 10.1088/0029-5515/19/4/007.

[45] J. B. Taylor. "Relaxation and magnetic reconnection in plasmas". In: *Reviews of Modern Physics* 58.3 (July 1986), pp. 741–763. DOI: https://doi.org/10.1103/RevModPhys.58.741.

[46] Bascom S. Deaver and William M. Fairbank. "Experimental Evidence for Quantized Flux in Superconducting Cylinders". In: *Phys. Rev. Lett.* 7 (2 July 1961), pp. 43–46. DOI: 10.1103/PhysRevLett.7.43.

[47] R. Doll and M. Näbauer. "Experimental Proof of Magnetic Flux Quantization in a Superconducting Ring". In: *Phys. Rev. Lett.* 7 (2 July 1961), pp. 51–52. DOI: 10.1103/PhysRevLett.7.51.

[48] B.D. Josephson. "Possible new effects in superconductive tunnelling". In: *Physics Letters* 1.7 (1962), pp. 251–253. ISSN: 0031-9163. DOI: https://doi.org/10.1016/0031-9163(62)91369-0.

[49] P. W. Anderson and J. M. Rowell. "Probable Observation of the Josephson Superconducting Tunneling Effect". In: *Physical Review Letters* 10.6 (Mar. 1963), pp. 230–232. DOI: https://doi.org/10.1103/PhysRevLett.10.230.

[50] I.K. Yanson, V.M. Svistunov, and I.M. Dmitrenko. "Experimental Observation of the Tunnel Effect for Cooper Pairs with the Emission of Photons". In: *JETP* 21.3 (1965), p. 650.

[51] J. G. Bednorz and K. A. Müller. "Possible high T_c superconductivity in the $Ba - La - Cu - O$ system". In: *Zeitschrift für Physik B Condensed Matter* 64 (2 1986), pp. 189–193. ISSN: 1431-584X. DOI: 10.1007/BF01303701.

[52] G. Ziegler. "Superconducting Properties of Nb_3Sn with High Carbon Doping". In: *Zeitschrift für Naturforschung A* 28.2 (Feb. 1973), pp. 318–319. DOI: 10.1515/zna-1973-0231.

[53] Y.V. Kopaev. "High-temperature superconductivity models". In: *Physics-Uspekhi* 45.6 (June 2002), pp. 655–659. DOI: 10.1070/pu2002v045n06abeh001196.

[54] J. Bardeen, L. N. Cooper, and J. R. Schrieffer. "Theory of Superconductivity". In: *Phys. Rev.* 108 (5 Dec. 1957), pp. 1175–1204. DOI: 10.1103/PhysRev.108.1175.

[55] L. D. Landau and E. M. Lifshitz. *Statistical Physics Part I*. 3rd. bibtex: landa;b;sp80. Amsterdam: Elsevier, 1980.

[56] A.A. Abrikosov. "On the Magnetic Properties of Superconductors of the Second Group". In: *JETP* 5 (6 Dec. 1957). (Russian original - ZhETF, Vol. 32, No. 6, p. 1442, December 1957), p. 1174.

[57] J. Garaud, M. N. Chernodub, and D. E. Kharzeev. "Vortices with magnetic field inversion in noncentrosymmetric superconductors". In: *Phys. Rev. B* 102 (18 Nov. 2020), p. 184516. DOI: 10.1103/PhysRevB.102.184516.

[58] Albert Samoilenka and Egor Babaev. "Spiral magnetic field and bound states of vortices in noncentrosymmetric superconductors". In: *Phys. Rev. B* 102 (18 Nov. 2020), p. 184517. DOI: 10.1103/PhysRevB.102.184517.

[59] A. Buzdin. "Direct Coupling Between Magnetism and Superconducting Current in the Josephson φ_0 Junction". In: *Phys. Rev. Lett.* 101 (10 Sept. 2008), p. 107005. DOI: 10.1103/PhysRevLett.101.107005.

[60] F. Konschelle and A. Buzdin. "Magnetic Moment Manipulation by a Josephson Current". In: *Phys. Rev. Lett.* 102 (1 Jan. 2009), p. 017001. DOI: 10.1103/PhysRevLett.102.017001.

[61] M. N. Chernodub, J. Garaud, and D. E. Kharzeev. *Chiral Magnetic Josephson junction: a base for low-noise superconducting qubits?* 2019. DOI: 10.48550/ARXIV.1908.00392.

[62] V. P. Mineev and K. V. Samokhin. "Nonuniform states in noncentrosymmetric superconductors: Derivation of Lifshitz invariants from microscopic theory". In: *Phys. Rev. B* 78 (14 Oct. 2008), p. 144503. DOI: 10.1103/PhysRevB.78.144503.

[63] Fuyuki Ando et al. "Observation of superconducting diode effect". In: *Nature* 584 (2020), pp. 373–376. DOI: 10.1038/s41586-020-2590-4.

[64] C. A. Reynolds, B. Serin, and L. B. Nesbitt. "The Isotope Effect in Superconductivity. I. Mercury". In: *Phys. Rev.* 84 (4 Nov. 1951), pp. 691–694. DOI: 10.1103/PhysRev.84.691.

[65] L.P. Gor'kov. "Microscopic derivation of the Ginzburg-Landau equations in the theory of superconductivity". In: *Sov. Phys. JETP* 9(6) (1959), pp. 1364–1367.

[66] R.L. Stratonovich. "A method for the computation of quantum distribution functions". In: *Dokl. Akad. Nauk SSSR* 115.6 (1957), pp. 1097–1100.

[67] J. Hubbard. "Calculation of Partition Functions". In: *Phys. Rev. Lett.* 3 (2 July 1959), pp. 77–78. DOI: 10.1103/PhysRevLett.3.77.

[68] Nicholas Manton and Paul Sutcliffe. *Topological Solitons*. Cambridge Monographs on Mathematical Physics. Cambridge University Press, 2004. DOI: 10.1017/CBO9780511617034.

[69] G. H. Derrick. "Comments on nonlinear wave equations as models for elementary particles". In: *J. Math. Phys.* 5 (1964), pp. 1252–1254. DOI: 10.1063/1.1704233.

[70] Maxim Chernodub, Shuangwei Hu, and Antti J. Niemi. "Topological solitons and folded proteins". In: *Physical Review E* 82.1 (July 2010). DOI: 10.1103/PhysRevE.82.011916.

[71] H.B. Nielsen and P. Olesen. "Vortex-line models for dual strings". In: *Nuclear Physics B* 61 (1973), pp. 45–61. ISSN: 0550-3213. DOI: https://doi.org/10.1016/0550-3213(73)90350-7.

[72] Ana Achúcarro and Tanmay Vachaspati. “Semilocal and electroweak strings”. In: *Physics Reports* 327.6 (2000), pp. 347–426. ISSN: 0370-1573. DOI: https://doi.org/10.1016/S0370-1573(99)00103-9.

[73] V. L. Berezinskii. “Destruction of Long-range Order in One-dimensional and Two-dimensional Systems Possessing a Continuous Symmetry Group. II. Quantum Systems”. In: *Soviet Journal of Experimental and Theoretical Physics* 34 (Jan. 1972), p. 610.

[74] J M Kosterlitz and D J Thouless. “Ordering, metastability and phase transitions in two-dimensional systems”. In: *Journal of Physics C: Solid State Physics* 6.7 (Apr. 1973), p. 1181. DOI: 10.1088/0022-3719/6/7/010.

[75] Vladimir I. Arnold. “The asymptotic Hopf invariant and its applications”. In: *Vladimir I. Arnold - Collected Works: Hydrodynamics, Bifurcation Theory, and Algebraic Geometry 1965-1972*. Ed. by Alexander B. Givental et al. Berlin, Heidelberg: Springer Berlin Heidelberg, 2014, pp. 357–375. ISBN: 978-3-642-31031-7. DOI: 10.1007/978-3-642-31031-7_32.

[76] J. H. C. Whitehead. “An Expression of Hopf’s Invariant as an Integral”. In: *Proceedings of the National Academy of Sciences* 33.5 (May 1947), pp. 117–123. DOI: https://doi.org/10.1073/pnas.33.5.117.

[77] Antonio F. Ranada. “A topological theory of the electromagnetic field”. In: *Letters in Mathematical Physics* 18.2 (Aug. 1989), pp. 97–106. DOI: https://doi.org/10.1007/BF00401864.

[78] William T. M. Irvine and Dirk Bouwmeester. “Linked and knotted beams of light”. In: *Nature Physics* 4.9 (Aug. 2008), pp. 716–720. DOI: https://doi.org/10.1038/nphys1056.

[79] Jarmo Hietarinta and Petri Salo. “Faddeev-Hopf knots: dynamics of linked unknots”. In: *Physics Letters B* 451.1-2 (Apr. 1999), pp. 60–67. DOI: https://doi.org/10.1016/S0370-2693(99)00054-4.

[80] E. A. Kuznetsov and V. P. Ruban. “Collapse of vortex lines in hydrodynamics”. In: *Journal of Experimental and Theoretical Physics* 91.4 (Oct. 2000), pp. 775–785. DOI: https://doi.org/10.1134/1.1326970.

[81] Anatoly Kamchatnov. “Topological solitons in magnetohydrodynamics”. In: *Sov. Phys.* 55 (Jan. 1982), pp. 69–73.

[82] C. B. Smiet et al. “Self-Organizing Knotted Magnetic Structures in Plasma”. In: *Physical Review Letters* 115.9 (Aug. 2015). DOI: 10.1103/PhysRevLett.115.095001.

[83] Iwo Bialynicki-Birula and Zofia Bialynicka-Birula. "Vortex lines of the electromagnetic field". In: *Phys. Rev. A* 67 (6 June 2003), p. 062114. DOI: 10.1103/PhysRevA.67.062114.

[84] Y.M. Cho, F. H. Cho, and J. H. Yoon. "Vacuum decomposition of Einstein's theory and knot topology of vacuum space-time". In: *Classical and Quantum Gravity* 30.5 (Feb. 2013), p. 055003. DOI: 10.1088/0264-9381/30/5/055003.

[85] Alexander Begun et al. "On topology and knotty entanglement in protein folding". In: *PLOS ONE* 16.1 (Jan. 2021), pp. 1–17. DOI: 10.1371/journal.pone.0244547.

[86] M. Yamada et al. "Quasistatic Formation of the Spheromak Plasma Configuration". In: *Phys. Rev. Lett.* 46 (3 Jan. 1981), pp. 188–191. DOI: 10.1103/PhysRevLett.46.188.

[87] M. Yamada et al. "Magnetic reconnection of plasma toroids with cohelicity and counterhelicity". In: *Phys. Rev. Lett.* 65 (6 Aug. 1990), pp. 721–724. DOI: 10.1103/PhysRevLett.65.721.

[88] Y. Ono et al. "Experimental investigation of three-dimensional magnetic reconnection by use of two colliding spheromaks". In: *Physics of Fluids B: Plasma Physics* 5.10 (1993), pp. 3691–3701. DOI: 10.1063/1.860840.

[89] C. G. R. Geddes, T. W. Kornack, and M. R. Brown. "Scaling studies of spheromak formation and equilibrium". In: *Physics of Plasmas* 5.4 (1998), pp. 1027–1034. DOI: 10.1063/1.872632.

[90] L.D. Landau, E.M. Lifshitz, and L.P. Pitaevskii. *Course of Theoretical Physics: Statistical Physics, Part 2 : by E.M. Lifshitz and L.P. Pitaevskii*. 1980.

[91] D. F. Agterberg. "Non-Centrosymmetric Superconductors: Introduction and Overview". In: *Non-Centrosymmetric Superconductors: Introduction and Overview*. Ed. by Ernst Bauer and Manfred Sigrist. Berlin, Heidelberg: Springer Berlin Heidelberg, 2012. Chap. Magnetoelectric Effects, Helical Phases, and FFLO Phases, pp. 155–170. ISBN: 978-3-642-24624-1. DOI: 10.1007/978-3-642-24624-1_5.

[92] R. G. Barrera, G. A. Estevez, and J. Giraldo. "Vector spherical harmonics and their application to magnetostatics". In: *European Journal of Physics* 6.4 (Oct. 1985), pp. 287–294. DOI: 10.1088/0143-0807/6/4/014.

[93] Jason Cantarella et al. "Influence of Geometry and Topology on Helicity". In: *Magnetic Helicity in Space and Laboratory Plasmas*. American Geophysical Union (AGU), 1999, pp. 17–24. ISBN: 9781118664476. DOI: https://doi.org/10.1029/GM111p0017. eprint: https://agupubs.onlinelibrary.wiley.com/doi/pdf/10.1029/GM111p0017.

[94] R. P. Kaur, D. F. Agterberg, and M. Sigrist. "Helical Vortex Phase in the Noncentrosymmetric $CePt_3Si$". In: *Phys. Rev. Lett.* 94 (13 Apr. 2005), p. 137002. DOI: 10.1103/PhysRevLett.94.137002.

[95] S. Chandrasekhar. "ON FORCE-FREE MAGNETIC FIELDS". In: *Proceedings of the National Academy of Sciences* 42.1 (Jan. 1956), pp. 1–5. DOI: 10.1073/pnas.42.1.1.

[96] John David Jackson. *Classical electrodynamics*. 3rd ed. New York, NY: Wiley, 1999. ISBN: 9780471309321.

[97] Kip S. Thorne. "Multipole expansions of gravitational radiation". In: *Rev. Mod. Phys.* 52 (2 Apr. 1980), pp. 299–339. DOI: 10.1103/RevModPhys.52.299.

[98] V.M. Dubovik and V.V. Tugushev. "Toroid moments in electrodynamics and solid-state physics". In: *Physics Reports* 187.4 (1990), pp. 145–202. ISSN: 0370-1573. DOI: https://doi.org/10.1016/0370-1573(90)90042-Z.

[99] Nicola A Spaldin, Manfred Fiebig, and Maxim Mostovoy. "The toroidal moment in condensed-matter physics and its relation to the magnetoelectric effect". In: *Journal of Physics: Condensed Matter* 20.43 (Oct. 2008), p. 434203. DOI: 10.1088/0953-8984/20/43/434203.

[100] Nahid Talebi, Surong Guo, and Peter A. van Aken. "Theory and applications of toroidal moments in electrodynamics: their emergence, characteristics, and technological relevance". In: *Nanophotonics* 7.1 (2018), pp. 93–110. DOI: doi:10.1515/nanoph-2017-0017. URL: https://doi.org/10.1515/nanoph-2017-0017.

[101] S. J. Blundell. "Spin-polarized muons in condensed matter physics". In: *Contemporary Physics* 40.3 (1999), pp. 175–192. DOI: 10.1080/001075199181521.

[102] Ikuto Kawasaki et al. "Superconducting Properties of Noncentrosymmetric Superconductor LaPt3Si Studied by Muon Spin Spectroscopy". In: *Journal of the Physical Society of Japan* 82.8 (2013), p. 084713. DOI: 10.7566/JPSJ.82.084713.

[103] R. P. Singh et al. "Detection of Time-Reversal Symmetry Breaking in the Noncentrosymmetric Superconductor Re_6Zr Using Muon-Spin Spectroscopy". In: *Phys. Rev. Lett.* 112 (10 Mar. 2014), p. 107002. DOI: 10.1103/PhysRevLett.112.107002.

[104] Seymour Stein. "Addition theorems for spherical wave functions". In: *Quarterly of Applied Mathematics* 19 (1961), pp. 15–24.

[105] Frank W. Olver et al. *NIST Handbook of Mathematical Functions*. 1st. USA: Cambridge University Press, 2010. ISBN: 0521140633.

[106] AP Prudnikov, Yu A Brychkov, and OI Marichev. *Integrals and series Volume 3: More special functions*. Taylor and Francis, Oxford, UK, 2003.

[107] M. Abramowitz and I. A. Stegun, eds. *Handbook of Mathematical Functions with Formulas, Graphs, and Mathematical Tables*. 10th printing, with correction. National Bureau of Standards, 1972.

[108] Khatuna Kachlishvili et al. "New Insights into Folding, Misfolding, and Non-folding Dynamics of a WW Domain". In: *The Journal of Physical Chemistry B* 124.19 (2020). PMID: 32271570, pp. 3855–3872. DOI: 10.1021/acs.jpcb.0c00628.

[109] Adam K. Sieradzan et al. "Investigation of Phosphorylation-Induced Folding of an Intrinsically Disordered Protein by Coarse-Grained Molecular Dynamics". In: *Journal of Chemical Theory and Computation* 17.5 (2021). PMID: 33909430, pp. 3203–3220. DOI: 10.1021/acs.jctc.1c00155.

[110] Anatolii Korneev et al. "Exploring Structural Flexibility and Stability of α-Synuclein by the Landau-Ginzburg-Wilson Approach". In: *The Journal of Physical Chemistry B* 126.36 (Sept. 2022), pp. 6878–6890. DOI: https://doi.org/10.1021/acs.jpcb.2c04651.

[111] V. G. Bornyakov et al. "Numerical study of the Roberge-Weiss transition". In: *Phys. Rev. D* 107 (1 Jan. 2023), p. 014508. DOI: 10.1103/PhysRevD.107.014508.

[112] R. N. Rogalyov et al. "Roberge–Weiss Transition in the Lee–Yang Approach". In: *Physics of Particles and Nuclei Letters* 20 (3 June 2023), pp. 438–442. DOI: 10.1103/PhysRevD.107.014508.

[113] Nikolai Gerasimeniuk et al. "Lee-Yang Zeroes in the Baryon Fugacity Plane: The Role of High Densities". In: *Particles* 6.3 (2023), pp. 834–846. ISSN: 2571-712X. DOI: 10.3390/particles6030053.

[114] Alexei Finkelstein and O.B. Ptitsyn. *Protein Physics: A Course of Lectures: Second, Updated and Extended Edition*. June 2016, pp. 1–508.

[115] Nora Molkenthin, Shuangwei Hu, and Antti J. Niemi. "Discrete Nonlinear Schrodinger Equation and Polygonal Solitons with Applications to Collapsed Proteins". In: *Physical Review Letters* 106.7 (Feb. 2011). DOI: 10.1103/PhysRevLett.106.078102.

[116] Shuangwei Hu, Martin Lundgren, and Antti J. Niemi. "Discrete Frenet frame, inflection point solitons, and curve visualization with applications to folded proteins". In: *Physical Review E* 83.6 (June 2011). DOI: 10.1103/PhysRevE.83.061908.

[117] Shuangwei Hu et al. “Towards quantitative classification of folded proteins in terms of elementary functions”. In: *Physical Review E* 83.4 (Apr. 2011). DOI: 10.1103/PhysRevE.83.041907.

[118] Andrei Krokhotin, Antti J. Niemi, and Xubiao Peng. “Soliton concepts and protein structure”. In: *Physical Review E* 85.3 (Mar. 2012). DOI: 10.1103/PhysRevE.85.031906.

[119] Andrey Krokhotin et al. “Coexistence of Phases in a Protein Heterodimer”. In: *The Journal of Chemical Physics* 137.3 (July 2012), p. 035101. DOI: 10.1063/1.4734019.

[120] Andrey Krokhotin, Martin Lundgren, and Antti J. Niemi. “Solitons and collapse in the λ-repressor protein”. In: *Physical Review E* 86.2 (Aug. 2012). DOI: 10.1103/PhysRevE.86.021923.

[121] Andrey Krokhotin et al. “Kinks, loops, and protein folding, with protein A as an example”. In: *The Journal of Chemical Physics* 140.2 (Jan. 2014), p. 025101. DOI: 10.1063/1.4855735.

[122] Alexander Molochkov, Alexander Begun, and Antti Niemi. “Gauge symmetries and structure of proteins”. In: *EPJ Web of Conferences* 137 (2017). Ed. by Y. Foka, N. Brambilla, and V. Kovalenko, p. 04004. DOI: 10.1051/epjconf/201713704004.

[123] Alexander Begun, Alexander Molochkov, and Antti J. Niemi. “Protein tertiary structure and the myoglobin phase diagram”. In: *Scientific Reports* 9.1 (July 2019). DOI: https://doi.org/10.1038/s41598-019-47317-y.

[124] Michelle L. Scalley and David Baker. “Protein folding kinetics exhibit an Arrhenius temperature dependence when corrected for the temperature dependence of protein stability”. In: *Proceedings of the National Academy of Sciences* 94.20 (Sept. 1997), pp. 10636–10640. DOI: https://doi.org/10.1073/pnas.94.20.10636.

Anatolii KORNEEV

Compact Chandrasekhar-Kendall states in noncentrosymmetric superconductors

Résumé en français :

Dans cette thèse, nous démontrons que les supraconducteurs à symétrie d'inversion brisée supportent une famille de configurations stables et spatialement localisées du champ magnétique auto-noué. Ces solutions sont les homologues supraconducteurs des états de Chandrasekhar-Kendall (les sphéromaks ou les toroflux) qui apparaissent dans les plasmas astrophysiques et de fusion nucléaire hautement conducteurs et sans force.

Nous étudions les sphéromaks supraconducteurs dans le formalisme de Ginzburg-Landau, en présence d'un invariant de Lifshitz brisant la parité associé à la symétrie cristallographique du premier groupe ponctuel. Nous démontrons que dans la limite de Londres, l'énergie totale de la solution diverge dans la région ultraviolette et, par conséquent, doit être régularisée dans la région du noyau singulier.

Nous montrons qu'une impureté sphérique isolée peut servir de centre de fixation pour un état supraconducteur de Chandrasekhar-Kendall à énergie finie et résoudre explicitement les équations du mouvement en présence d'une impureté. Nous soutenons également qu'un dipôle magnétique ou une inclusion ferromagnétique dans la masse d'un supraconducteur noncentrosymétrique fournit des solutions de sphéromak à énergie finie. Nous construisons explicitement des solutions induites par un dipôle ferromagnétique et discutons de l'influence du paramètre de rupture de parité sur la structure, l'énergie et l'hélicité de ces configurations.

Mots clés : symétrie d'inversion spatiale brisée, condensats non centrosymétriques, États de Chandrasekhar-Kendall, hélicité magnétique, supraconducteurs

Summary :

In this thesis, we demonstrate that superconductors with broken inversion symmetry support a family of stable, spatially localized configurations of the self-knotted magnetic field. These solutions are the superconducting counterparts of the Chandrasekhar-Kendall states (spheromaks or toroflux) that appear in highly conducting, force-free astrophysical and nuclear-fusion plasmas.

We study the superconducting spheromaks in the Ginzburg-Landau formalism in the presence of a parity-breaking Lifshitz invariant associated with the O crystallographic point group symmetry. We demonstrate that in the London limit, the total energy of the solution diverges in the ultraviolet region and, therefore, needs to be regularized at the singular core region.

We show that an isolated spherical impurity may serve as a pinning center for a finite-energy superconducting Chandrasekhar-Kendall state and explicitly solve the equations of motion in the presence of an impurity. Also, we argue that a magnetic dipole or a ferromagnetic inclusion in the bulk of noncentrosymmetric superconductor sources finite-energy spheromak solutions. We explicitly construct solutions induced by a ferromagnetic dipole and discuss the influence of the parity-breaking parameter on the structure, energy, and helicity of these configurations.

Keywords : broken spatial inversion symmetry, non-centrosymmetric condensates, Chandrasekhar-Kendall states, magnetic helicity, superconductors